Spectroscopy of Semiconductor Nanostructures for Mid-IR Photonics

by

Michael K. Lewis

A Thesis submitted to the University of Surrey for the degree of Doctor of Philosophy

Physics Department, Faculty of Engineering and Physical Sciences, University of Surrey, Guildford, Surrey, GU2 7HX

August 2013

Abstract

Quantum dot structures of InAs(Sb)/InGaAs/InP designed as easy to fabricate, low cost mid-IR emitting lasers, have been spectroscopically characterised using temperature and power dependent photoluminescence. These structures have been simulated using a truncated pyramid structure in the Nextnano software package. The results show that the observed experimental data is the result of a bimodal dot distribution in both samples. In the InAs case, the bimodal behaviour is the result of varying width dots (35nm and 38.5nm). In the InAsSb case the dot groups were calculated to contain ~10% and zero antimony, indicating difficulties during the growth process. Additionally the InAs dots were found to have a dominant radiative recombination process, while the InAsSb dots were found to be affected by a defect related recombination process. It is suggested this is a result of increased defects formed by the larger lattice mismatch.

InAs/InAsSb superlattice structures have potential as mercury cadmium telluride (MCT) alternative mid-IR photo-detectors, and are predicted to not suffer from Ga-related defect recombination as other superlattice structures. High pressure techniques and modelling were used to probe the defect level in these structures. High pressure, low temperature photoluminescence experiments were performed using the sapphire ball cell to move the conduction band minima up in energy until overlap with the predicted defect level state was achieved. This resulted in a decrease in the measured integrated intensity of the sample due to carriers recombining via the defect states. Additionally power dependent measurements at high and low pressure were performed and an observed shift from radiative to defect dominated recombination was observed. This provides the first experimental evidence of a defect level positioned above the conduction band edge. This means that SRH recombination in the forbidden band gap will not be a contributing factor to the dark currents in InAs/InAsSb superlattice photo-detectors showing their promise for low dark current mid-IR detectors.

Acknowledgements

I began this PhD after quitting a lucrative job much to my wife's dismay, because I did not feel mentally challenged. During this PhD I no longer have that problem, every day has been a challenge that has culminated in this document. While ultimately it has been my responsibility to finish this work there are many people who have helped along the way, and I shall take a moment to thank them.

Firstly, there is my long-suffering wife. She has provided the family financial aid, and listened to me ranting about physics even though I know she does not understand a word of it. Prof. Stephen J. Sweeney is also high on my list of thanks. As a supervisor he is often busy on different projects, however he always provided insight into the data and without his pushing I would not have finished this work. Thanks also to Dr. Jeff Hosea for accepting me to begin a PhD at Surrey and providing me with the laboratory and tools to actually conduct experiments (even if they were in DOS). Thanks also to Dr Benjamin Crutchley, Dr Barnabus Ikyo, and Graham Read for the group meetings without which I may know no theory at all. Finally thanks to all my friends and family who have provided support throughout this portion of my life.

I would also like to express my gratitude to SEPnet and Qinetiq for funding my research and also NTU and ASU for providing the samples that were studied.

Publications

M. K. Lewis, A. Prins, Z. Bushell, Y-H. Zhang, S. J. Sweeney, "*Evidence for a defect level above the conduction band edge of InAs/InAs1-xSbx type-II super-lattices*", In preparation for the Journal of Applied Physics

M. K. Lewis, T. J. C. Hosea, X. Tang, S. J. Sweeney, *"Characterising the Temperature Dependent Blue-shift of InAsSb Quantum Dots"*, In preparation for the Journal of Applied Physics

Conferences

M. K. Lewis, A. Prins, Z. Bushell, Y-H. Zhang, S. J. Sweeney, "*Evidence for a defect level above the conduction band edge of InAs/InAs1-xSbx type-II super-lattices*", UK Semiconductors, Sheffield, 2013.

M. K. Lewis, A. Prins, Z. Bushell, Y-H. Zhang, S. J. Sweeney, *"Performance Improvements in Antimony Based Photo-detectors"*, ATI Open Day, Guildford 2012.

M. K. Lewis, T. J. C. Hosea, X. Tang, S. J. Sweeney, *"Temperature and power dependent blue shifts in mid-IR quantum dots"*, UK Semiconductors, Sheffield, 2012.

M. K. Lewis, T. J. C. Hosea, X. Tang, S. J. Sweeney, *"Temperature Dependent Blue Shift in Mid-IR Quantum Dots"*, SIOE, Cardiff, 2012.

M. K. Lewis, T. J. C. Hosea, X. Tang, S. J. Sweeney, *"InP based quantum dots for mid-IR applications"*, ATI Open Day, Guildford, 2011.

Chapter 1 - Introduction

1.1 The Mid-IR

The mid-IR region is loosely defined to be the wavelength region between 2μm and 8μm. This broad wavelength region has many important applications to fields such as medicine, the military, communications and gas sensing [1]. In the future through semiconductor development, these fields could have easy to use wavelength tailored devices, rather than using the closest matching device that currently exists.

In the medical industry lasers have many uses ranging from the treatment of skin cancer using photodynamic therapy [2] (note this treatment is usually not performed with a mid-IR laser), to the correction of vision using laser eye surgery. Using a laser to replace a traditional scalpel produces finer cuts; this results in less scarring and faster recovery times [3].

Uses in the military are varied and include; range finding, decoys for confusing a heat-seeking missile, using mid-IR laser chaff of greater intensity than the engines heat output. Another example is making thermal images useless with an intense mid-IR source.

Mid-IR devices are ideally suited to free space communications as there is an atmospheric window in this wavelength range as shown in figure 1. Free space communications using mid-IR laser require only a transmitter and detector, this allows cost saving to made in infrastructure such as not having to purchase, lay, and maintain optical cabling (at the time of this thesis priced at £3.96 per metre [5]). Power transfer from space to earth is also in development [6] currently at wavelengths of 1.55μm. This would allow targeted power transfer to earth at skin and eye safe wavelengths using IR lasers.

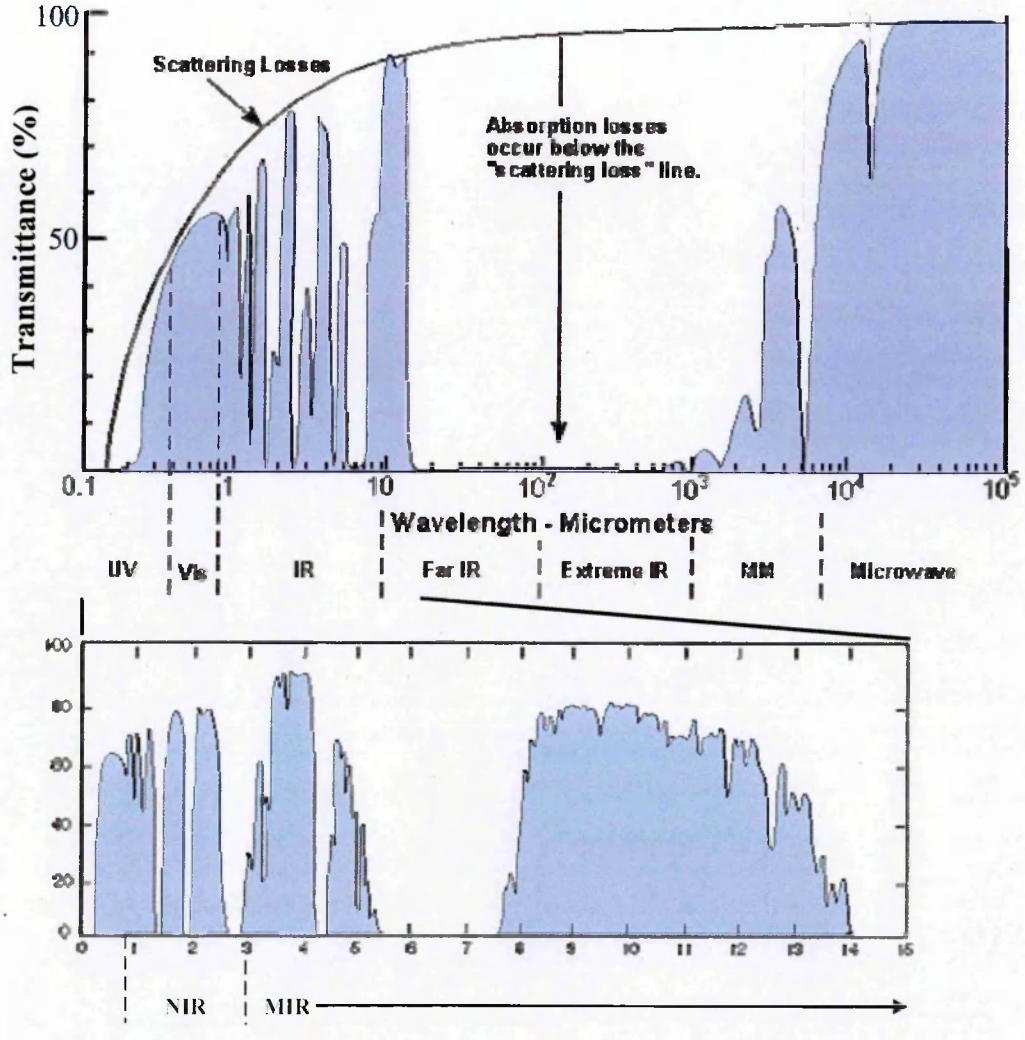

Figure 1: the percentage of light transmitted through the atmosphere at various wavelengths. The bottom plot expands the mid-IR region of interest t this work. Adapted from 4.

High sensitivity gas sensing is also a large application for mid-IR lasers. Many pollutant gases have strong absorption features in the mid-IR, such as: NH3 (2.1 μm), HF (2.5 μm), CH_4 (2.35 μm and 3.3 μm), HCHO (3.5 μm), HCl (3.5 μm), N_2O (3.9 μm and 4.5 μm), SO_2 (4 μm), CO_2 (4.25 μm) and CO (2.3 μm and 4.6 μm) [7]. The ability to accurately track the quantity of these gases in the atmosphere has direct applications to monitoring the progress of global warming.

Though these are just a few examples of the potential uses, it can clearly be seen that mid-IR devices are an important part of modern society. This means that developing mid-IR devices that operate at a variety of wavelengths and room temperature is increasingly important. Creating these long wavelength room temperature devices is scientifically challenging, and this work will use

spectroscopic techniques and simulations to investigate the underlying physics behind the studied devices for future development.

1.2 Quantum Dots

Quantum dot devices gained much interest after they were predicted to be temperature independent [8]. This was later found to *be* more complicated due to the dominance of Auger recombination at higher temperatures [9]. Quantum dots are still of great interest however. They typically have a lower threshold current density and reduced temperature sensitivity than the equivalent quantum well laser. This is because their small volume can therefore be used to create dense arrays of low power devices.

While quantum dot devices in the visible region are readily available most IR research has been to create quantum dot devices that emit at 1.3μm and 1.55μm. These wavelengths are of interest to the telecoms industry as there are loss minima for silica based optical fibres at these wavelengths [10]. Quantum dot devices emitting at 1.3μm manufactured from InGaAs/GaAs and InAs/InGaAs have been demonstrated, showing improved characteristics compared to QWs developed [11, 12, 13] 1.55μm devices manufactured from InAs/InP [9] are also the subject of investigation.

To extend the wavelength of quantum dot systems into the desired mid-IR wavelength range narrow bandgap materials such as In(As)Sb on GaSb substrates have been extensively investigated [14]. Fundamentally the bandgap range of a quantum dot material lies between the bulk bandgap of the barrier material used, and the bulk bandgap of the dot material. This makes the longest possible wavelength of InAs 2.97μm (0.417eV) [15] and InAsSb less than 5.27μm (0.235eV)[15] due to its large bowing parameter. These values are unattainable in practice due to the large wavefuntion confinement in quantum dots. There has been some success in growing self assembled SK mid-IR dot materials using "standard" MOVPE techniques, a 2μm room temperature laser has been developed from InAsSb/InP [16]. Wavelengths of 2.46μm at 6K have been reached using InAs/InGaAsP/InP [17] quantum dots. To extend the wavelength

limit even further, non-standard growth techniques are being investigated and are reviewed in a later chapter.

1.3 Photo-detectors

While there are many detectors available for purchase that cover the infrared region with varying sensitivities, Mercury Cadmium Telluride ($Hg_{1-x}Cd_xTe$) (also known as MCT) detectors are currently the commercially available standard for mid-IR photo-detectors. They were first engineered as a direct band gap material for the long wavelength infrared region in 1957 [18], and have been under development since then.

Despite the dominance of $Hg_{1-x}Cd_xTe$ photo-detectors in the mid-IR detection market, there are alternatives in the form of antimonide based type-II superlattices. These superlattice structures are predicted to have similar optical properties as the $Hg_{1-x}Cd_xTe$ mid-IR detectors, while having much improved electrical properties. The fist superlattice structures able to directly compete with $Hg_{1-x}Cd_xTe$ detectors were InAs/InGaAs type-II superlattices. Not only did these structures have the predicted electrical improvements, these superlattice structures are also less toxic to the environment than mercury and cadmium containing structures.

Though a viable alternative, InAs/InGaAs superlattice structures were found to have very large dark currents caused by SRH recombination in the forbidden bandgap therefore limiting their suitability as photo-detectors. The current generation of type II superlattice studied in this work is a InAs/InAsSb superlattice. This type of superlattice is predicted to have the defect state positioned above the conduction band edge, thus having no significant dark current contribution from Shockley-Read-Hall (SRH) in the forbidden band gap under ambient conditions.

1.4 Thesis Summary

Chapter 2 focuses on the fundamental physics built upon later in this work. These fundamentals include some of the analysis techniques used in later sections, and the theory behind the main spectroscopic techniques used.

Chapter 3 outlines the considerations that must be made when working in the mid-IR regime in terms of optical apparatus. The operation of the sapphire ball cell is also described with attention given to operating this piece of apparatus in the mid-IR. Finally, the experimental apparatus is presented on which the data was gathered.

Chapter 4 outlines the dependence of dot morphology on strain, and shows how the morphology is directly related to the dot emission wavelength. Simulated and experimental results are used to characterise InAs and InAsSb quantum dot structures emitting at ~2μm, and a theory for the underlying physics behind the observed measurements is presented and justified.

Chapter 5 describes why the new generation of superlattice structures could prove superior to $Hg_{1-x}Cd_xTe$ photo-detectors. Using high pressure and low temperature measurements the first experimental evidence of a defect state above the conduction band edge in InAs/InAsSb superlattice structures is discovered.

Chapter 6 summarizes the main findings of this work and suggests possible future research in the field.

1.5 References

[1] Z. Yin et al., *"A review of energy bandgap engineering in III–V semiconductor alloys for mid-infrared laser applications"*, Solid-State Electron. 51, 1, 6-15 (2007)

[2] Moan, J. and Q. Peng, "*Photodynamic therapy*", The Royal Society of Chemistry, (2003)

[3] .H. Sliney, et al., "*Medical lasers and their safe use*", (1992)

[4] M. Merrick PhD thesis *"Optical studies of Band Structure and Spin- dependent Processes in mid-infrared semiconductor devices and materials"*, Department of Physics, University of Surrey (2006)

[5] Thorlabs single Mode Fibre Costs, Accessed July 2013, <http://www.thorlabs.de/NewGroupPage9.cfm?ObjectGroup_ID=949&pn=SM980-5.8-125>

[6] J Mukherjee et al., *"Efficiency limits of laser power converters for optical power transfer applications"*, Journal of Physics D: Applied Physics 46, 26, (2013)

[7] André Joullié and Philippe Christol, "*GaSb-based mid-infrared 2–5 μm laser diodes*" Comptes Rendus Physique, 4, 621 (2003).

[8] Y. Arakawa et al., "*Multidimensional Quantum Well Laser and Temperature Dependence of its Threshold Current*", Applied Physics Letters 40, 939, (1982)

[9] S. A. Sayid et al., *"Efficiency limiting processes in 1.55μm InAs/InP-based quantum dots lasers"*, Applied Physics Letters 97, 161104 (2010)

[10] S. J. Sweeney et al., *"The Effect of Temperature Dependent Processes on the Performance of 1.5μm Compressively Strained InGaAs(P) MQW Semiconductor Diode Lasers"*, IEEE Photonics Technology Letters 10, 8, 1076 (1998)

[11] D. L. Huffaker et al., *"1.3μm room-temperature GaAs-based quantum-dot laser"*, Applied Physics Letters 73, 2654 (1998)

[12] Y. Qui et al., *"High-performance InAs quantum-dot lasers near 1.3μm"*, Applied Physics Letters 79, 3570 (2001)

[13] K. Mukai et al., *"1.3μm CW Lasing of InGaAs–GaAs Quantum Dots at Room Temperature with a Threshold Current of 8 mA"*, IEEE Photonics Technology Letters 11, 10, 1205 (1999)

[14] R. M. Biefeld, *"The metal-organic chemical vapor deposition and properties of III-V antimony-based semiconductor materials"*, Materials Science Enginering R 36, 105 (2002)

[15] I. Vurgaftman et al., *"Band parameters for III–V compound semiconductors and their alloys"*, Journal of Applied Physics 89, 11, (2001)

[16] Yueming Qiu et al., *"Room-temperature continuous-wave operation of InAsSb quantum-dot lasers near 2 μm based on (001) InP substrate"*, Applied Physics Letters 84, 263 (2004)

[17] J. Kotani et al., *"Mid-infrared emission from InAs quantum dots, wells and dot on well nanostructures grown on InP (100) by MOVPE"*, Journal of Applied Physics 106, 093112 (2009)

[18] P. Norton, *"HgCdTe Infrared Detectors"*, OPTO-ELECTRONICS REVIEW 10(3), 159–174 (2002)

Chapter 2 - Theory

2.1 Introduction

This chapter outlines some elements of key semiconductor theory that is the foundation for work done in later chapters. This begins with the density of states for bulk materials, and is limited in dimensionality until the density of states for a 0D structure such as the ideal quantum dot is shown. The occupation of these available states is then discussed using the Fermi-Dirac distribution.

Other important topics which are used throughout this work such as the different type of band alignments formed by a simple hetero-junction are shown, along with the principle behind the alloying of semiconductor materials to engineer desired optical properties.

The physics behind the principal spectroscopy types of PL and absorption is also covered in detail, and how they are physically fitted to experimental data. Finally, physics of photo-detector operation, focusing specifically on the sources of dark current are discussed. This becomes of relevance when the benefits of antimony vs. gallium type II superlattice photo-detectors are discussed in chapter 5.

2.2 Semiconductor Theory

2.2.1 The Density of states

The density of states (DOS) of a material describes the number of states available to be occupied by electrons per unit energy per unit volume. Classically, all values of energy are allowed resulting in any number of states to be occupied. However, when dealing with quantum mechanical particles such as fermions the Heisenberg uncertainty principle and the Pauli exclusion principle must be obeyed restricting the available energy levels. Furthermore, the Schrödinger equation must be satisfied subject to the boundary conditions imposed on the system, such as limits on the dimensionality. Degeneracy of the solutions must also be accounted for, i.e. for one energy level, more than one set of k-space values may give the same energy.

Each of these restrictions on the dimensions result in the density of states being proportional to the number of degrees of freedom in the system as can be seen in figure 1. The resulting density of states from limiting these degrees of freedom caused by restricting the dimensionality are shown in figure 1 along with their energy dependence. At this point is should be noted that real quantum dot systems have a finite size, this means that DOS for a real dot system is not a perfect delta function. Instead the DOS for a real dot has a broadening of the delta function dependent on its volume. Further to this there are usually many dots in a system with a distribution of sizes, further broadening the density of states.

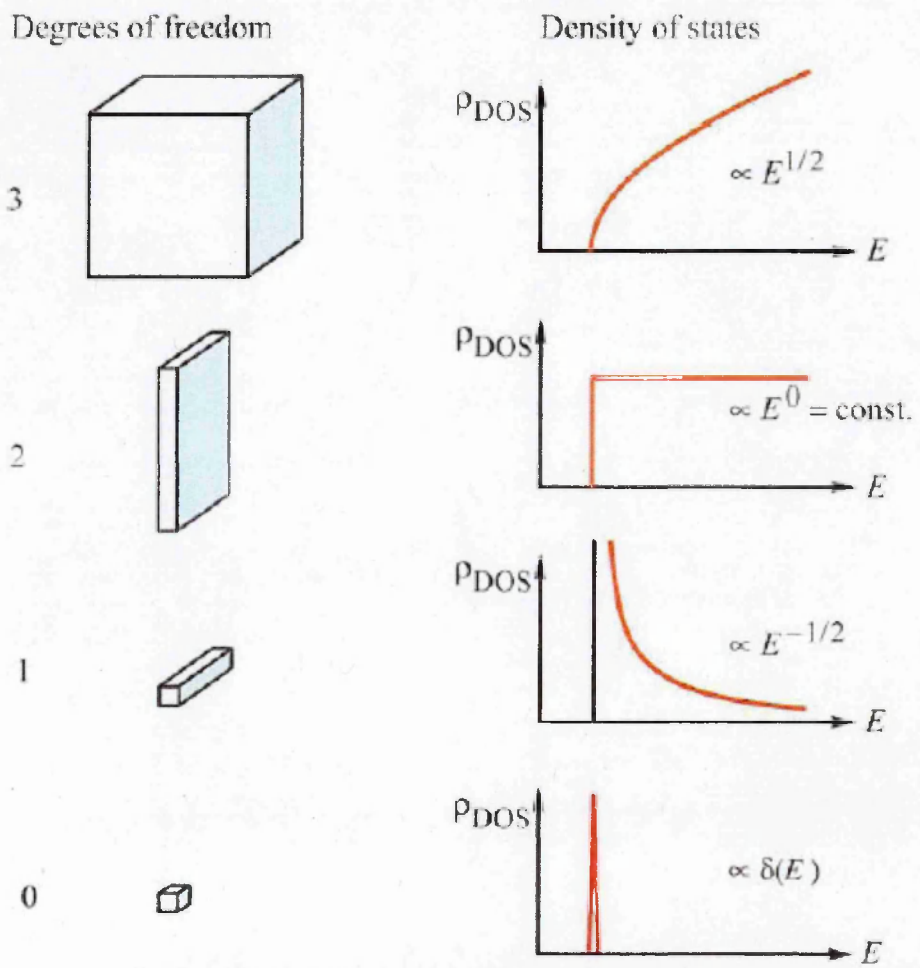

Figure 1: The density of states for 3D, 2D, 1D and 0D. Also shown in the proportionality of the energy dependence in each case. Adapted from [1].

2.2.2 Occupation of energy levels

While the density of states describes the states available for occupation, the probability of occupying these states is described by the Fermi-Dirac distribution. The Fermi-Dirac distribution is used as electrons and holes are fermions and therefore obey Fermi-Dirac statistics rather than the Bose-Einstein statistics. The Fermi-Dirac distribution gives the probability that a state energy E will be occupied in an ideal electron gas at thermal equilibrium and is given by the function:

$$f(E) = \frac{1}{exp[(E - E_F/k_B T] + 1} \qquad (1)$$

Where E is the state energy, E_F is the Fermi energy, k_B is the Boltzman constant and T is the temperature. At 0K this function produces a sharp step, and as the temperature is increased this step begins to broaden as shown in figure 2.

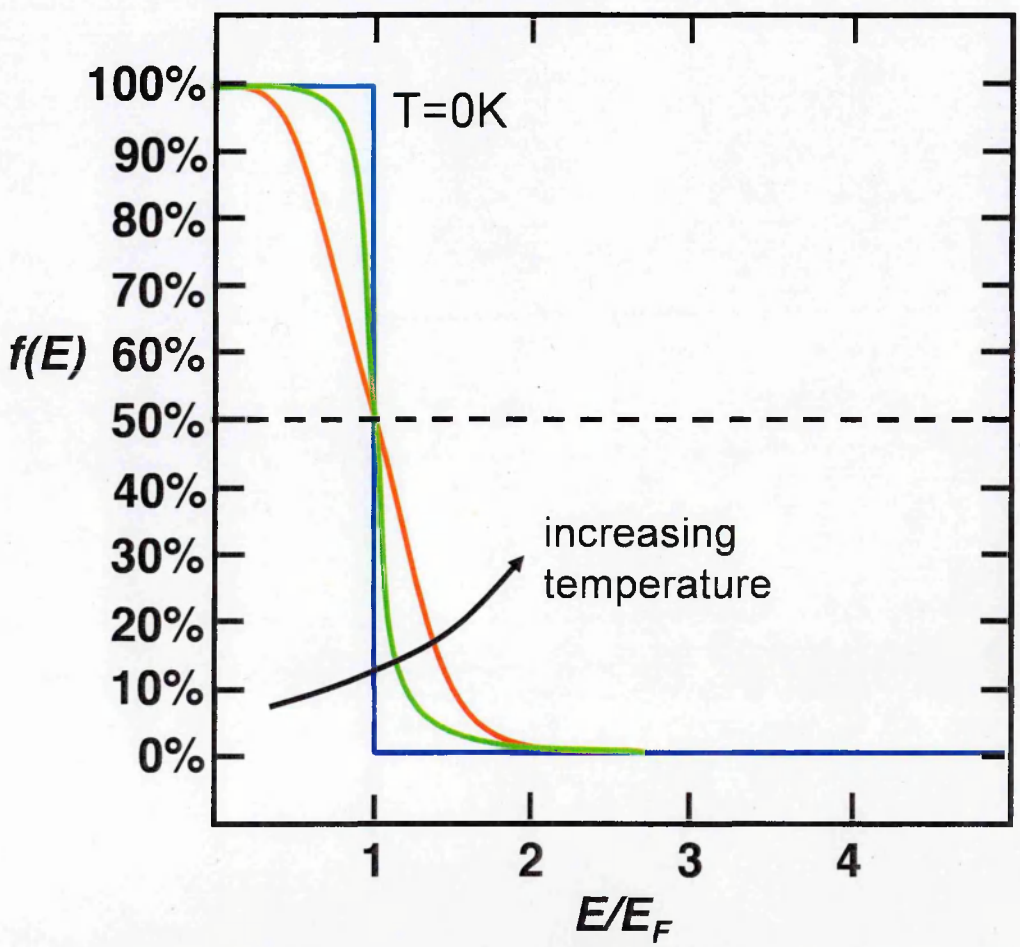

Figure 2: The Fermi-Dirac distribution. As temperature is increased the electrons are found in higher energy levels. Adapted from [2].

As the number of available states has been defined by the density of states, and the occupation of states has been described by the Fermi-Dirac function. These two functions can be combined to determine the occupation of a system as a function of temperature. The occupancy of the three dimensional density of states by a free electron gas obeying the Fermi-Dirac distribution is shown in figure 3. The shaded region shows the electron occupancy at 0K, as the temperature is increased there is a temperature related broadening of magnitude k_BT, resulting in electrons being thermally excited from region 1 to region 2. While bulk materials are not studied in this work, the figure illustrates that there is a thermal contribution to the band occupation present for all practical dimensionally restricted systems.

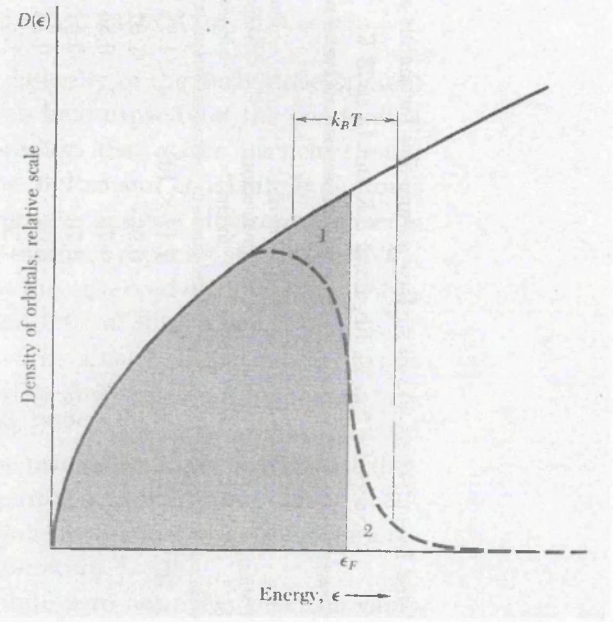

Figure 3: The3D density of states occupation of a Fermi-Dirac electron gas. The shaded region represents the occupation at 0K. Adapted from [3].

2.2.3 Band alignment types

As this work considers quantum dots as well as superlattice structures consisting of many quantum wells, it is prudent to briefly classify the type of band alignments that can be achieved when creating a hetero-junction and the parameters used to describe them. Figure 4 shows the three types of hetero-junction formed by combining two different bandgap materials A and B. The

Energy gap of material A or B is labelled E_{gA} or E_{gB} respectively. The terms ΔE_c and ΔE_v represent the conduction and valence band offsets respectively.

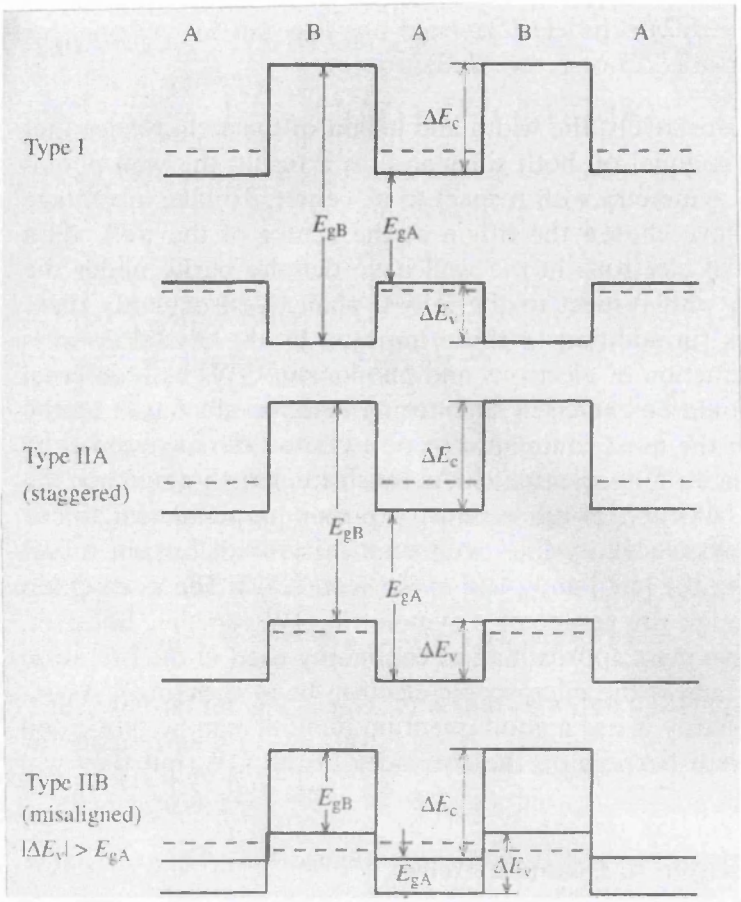

Figure 4: The different type of heterojunction band alignments. Adapted from [4].

Type I alignment creates the situation where the lowest energy transition is spatially direct between the valence and conduction band of one material (A). The second material (b) then creates a potential barrier to confine the carriers. This is the case of a classic type I quantum well.

Type II staggered alignment creates the situation where the lowest energy transition is spatially indirect and requires some spatial overlap of the wave function to allow excitation and relaxation of electrons to occur. The lowest energy transition becomes from the valence band of material B to the conduction band of material A. In this case the potential barrier to confine the carriers is supplied by the opposite material i.e. confinement in the valence band I supplied by material A and conduction band confinement by material B.

Type II misaligned (also known as type III) occurs when the valence band of material B is higher in energy then the bottom of the conduction band in material A. This hetero-juction behaves like a negative or zero-gap semiconductor or semimetal.

2.2.4 Semiconductor Alloys

Semiconductor alloying is the process of taking two (or more) semiconductors and combining them to create an alloy with properties such as the bandgap, that has values between both. An example of this used in this work is the ternary alloy $InAs_{1-x}Sb_x$. This is an alloy of the binary materials InAs and InSb, when the ternary alloy is formed arsenic atoms are replaced with antimony atoms resulting in a change in the electronic and optical properties of the material. In the case of bandgap, increasing the antimony content of the ternary alloy decreases the bandgap, this change between the two materials is not linear however and can be described a bowing parameter. The common ternary III-V are shown in figure 5 and are joined by curves descriving their bowing parameters.

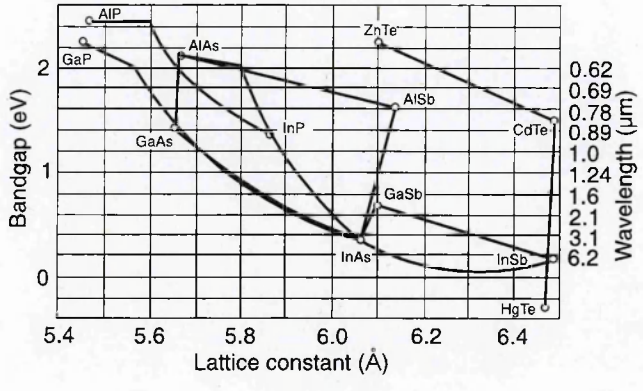

Figure 5: The bandgap and bowing parameter formed for many of the tertiary alloys. Adpated from [5]

During this work the main semiconductor parameters used are effective masses m_c^*, m_{hh}^*, m_{lh}^*, bandgap E_g and lattice constant. The ternary material $InAs_{1-x}Sb_x$ studied in this work has been well documented by I. Vurgaftman et al. [6]. The bandgap is determined by the bowing parameter as shown in figure 5. The

effective mass (m_c^*, m_{hh}^*) is approximately proportional to the bandgap and is therefore determined by the same parameter, while the lattice constant is a linear extrapolation between the two binaries.

2.2.5 Bandgap Temperature Dependence

As a III-V semiconductor is heated, the bandgap is reduced. This is due to thermal dilation of the lattice with temperature, and has been empirically expressed in the following equation, known as the Varshni Equation [7]:

$$E_g(T) = E_g(0) - \frac{\alpha T^2}{T + \beta} \qquad (2)$$

Where $E_g(0)$ is the bandgap of the material at 0K, and α and β are constants of the material. While the Varshni equation is normally found to be a good fit for bulk materials and hetero-structures, later on in this work it will be shown that it is not always suitable for more complex structure such as superlattices.

2.3 Recombination Processes

Once a semiconductor has absorbed a photon, then there are three major recombination processes available for excited carriers. The proportion of the total photo-generated carriers which recombine via each mechanism is different for each semiconductor and can depend on parameters like temperature and pressure. Each of the major recombination methods will be outlined in this section and also how one experimentally identifies which process is dominant in the material being measured.

2.3.1 Radiative Recombination

An electron in the conduction band recombines with the hole, returning the semiconductor to its ground state by emitting a photon, as shown in figure 6. When performing PL experiments on a semiconductor, this is the measured output.

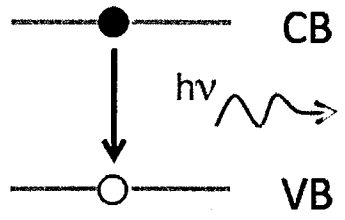

Figure 6: An electron recombines with a hole to emit a photon with energy proportional to the bandgap.

2.2.2 Defect related Recombination

Defect related recombination now differs from radiative recombination, as there is a defect related state located in the forbidden band gap by which the electon hole pair recombine. In a two stage recombination process the electron now recombines firstly from the conduction band to the defect state. Then secondly from the defect state to the valence band, returning the system to its ground state as shown in figure 7. While this recombination process may emit a photon when performing these transitions, this photon will have energy proportional to the energy gap between the conduction band and defect state or the defect state and valence band. However, the majority of these transitions are non-radiative releasing the energy via phonons therefore heating the lattice.

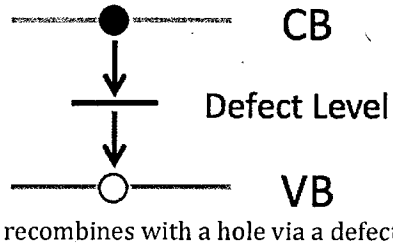

Figure 7: An electron recombines with a hole via a defect state within the bandgap.

2.3.3 Auger Recombination

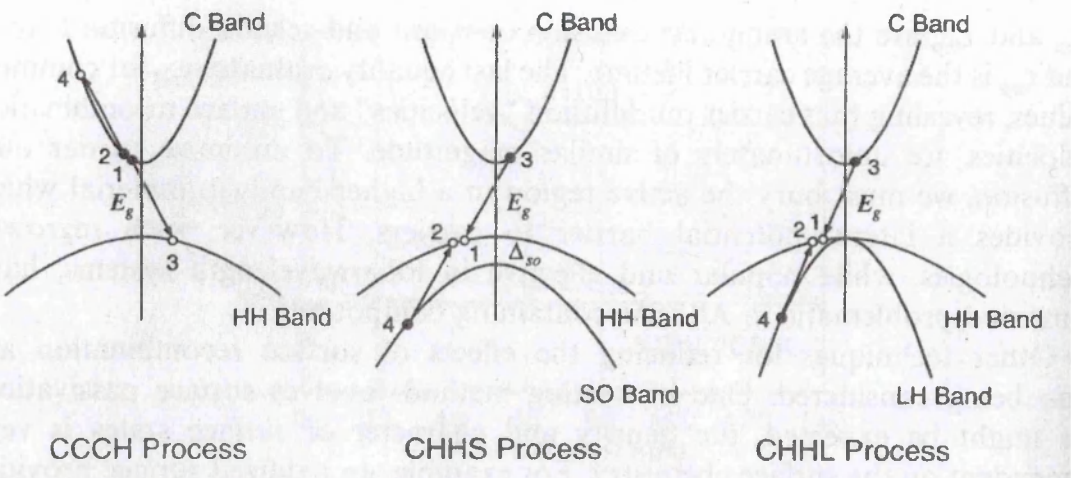

Figure 8: Three Auger recombination processes. Adapted from [8].

Some examples of Auger recombination processes are shown in figure 8.The CCCH (two conduction band electrons "CC" interacting to move to the conduction band and HH band "CH") process involves two electrons "colliding" via coulombic interaction of one of the electrons moves to the valence band and the other higher into the conduction band. This electron then thermalizes back down to the bottom of the conduction band releasing the excess energy to the lattice as heat. A similar process can occur in the heavy hole band where one hole is promoted to the conduction band and the other is promoted to spin off band (CHHS) or the light hole band (CHHL).

As Auger relies on the collision of carriers it can be seen that the CCCH process will occur when there is a high electron density, and the CHHS and CHHL process will occur when there is a high hole density.

2.3.4 Identifying Recombination Processes

The total input pump power into a sample is the sum of all the carrier related processes. The defect related recombination, the radiative recombination and Auger recombination. An expression for the total pump power is given by [9]:

$$P \propto An + Bn^2 + Cn^3 \qquad (3)$$

Where A, B, and C are recombination coefficients of the defect, radiative and Auger processes respectively. P is the total pump power, and n is the density of carriers, assuming that the electron and hole densities are equal. When performing a measurement only the radiative recombination component is measured. Therefore the measured light output is given by:

$$L \propto Bn^2 \tag{4}$$

Assuming that the coefficient has no dependence on carrier density i.e. B≠B(n) it follows that:

$$n \propto L^{1/2} \tag{5}$$

If one recombination process dominates over all others in the sample, (3) may be written as:

$$P \propto n^z \tag{6}$$

Where z = 1, 2, 3 depending on the number of carriers involved in the recombination process. Substituting in equation 5 to equation 6:

$$P \propto L^{z/2} \tag{7}$$

Taking the log of both sides gives:

$$\log P \propto \frac{z}{2} logL \tag{8}$$

Rearranging:

$$LogL \propto \frac{2}{z} logP \tag{9}$$

Equation 9 now gives an expression combining the measureable variables of pump power and light intensity. Plotting logL vs LogP and taking the gradient

gives a method of identifying the dominant recombination process in the sample. As discussed above, radiative recombination has two particles involved (z = 2) therefore the identifying gradient would be 1. Defect related recombination is a single particle process (z = 1) therefore the identifying gradient is 2. Auger related recombination is a three-particle process (z = 3) and therefore the identifying gradient would be 2/3. A combination of these processes can give a non-integer value of z.

2.4 Photoluminescence

Photoluminescence (PL) is the absorption of an incident photon of energy greater then the material bandgap to create an electron-hole pair, and subsequent radiative recombination of this pair to emit a photon of energy proportional to the energy of the bandgap. This basic principle will now be expanded upon to build a more complete picture of the process.

Einstein was the first to document the relationship between absorption and spontaneous emission, and as such the coefficients for the rates are named after him, the Einstein coefficients. A_{nm} the rate of spontaneous emission of radiation due to transition from level n to m, and B_{nm} the rate of absorption due to transition from a non degenerate level n to m. When $B_{nm} = B_{mn}$ie the absorption from non degenerate level n to m, is the the same as the absorption from m to n, these coefficients are related by equation 10 [4]:

$$A_{nm} = \frac{8\pi h v^3 n_r^3}{c^3} B_{nm} \tag{10}$$

Where h is Plancks constant, v is the photon frequency, c is the velocity of light in a vacuum, and n_r is the refractive index of the semiconductor material which is assumed to be non-dispersive. When in thermal equilibrium the rate of

absorption and emission between the conduction and valence bands must be equal. This relation between absorption and emission is known as the Roosbroek-Shockley relation [4]:

$$P_{vc}(v)\rho(v) = R_{vc}(v) \tag{11}$$

Where P_{vc}, is the absorption rate between the valence and conduction band, R_{vc} is the emission rate between the valence and conduction band, and ρ is the photon energy density. The absorption rate P_{vc} is related to absorption coefficient by $P_{vc} = \alpha c/n_r$ where α is the absorption coefficient of the semiconductor. Combining these equations and using the Planck distribution at a temperature T to represent ρ, the photon energy density, a relationship between emission probability and the absorption coefficient can be obtained [4]:

$$R_{vc} = \frac{\alpha(v)8\pi v^2 n_r^2}{c^2[\exp(E/k_bT) - 1]} \tag{12}$$

When the sample is optically excited using a laser, the system is driven away from this thermal equilibrium state unbalancing the emission and absorption rates. During a PL experiment the emission of excess photons while the sample returns to thermal equilibrium is what one generally detects. The non equilibrium states are described using quasi-Fermi levels. The stronger the excitation on the sample, the further the quasi-Fermi level is shifted from the actual Fermi level.

Under CW excitation a quasi-thermal equilibrium state is quickly reached in the sample, fixing the quasi-Fermi levels. To calculate the emission from a semiconductor in this quasi-thermal-equilibrium situation one can start from the emission rate in thermal equilibrium, defined as [4]:

$$R_{cv} = A_{cv} f_c (1 - f_v) \tag{13}$$

Where A_{cv} is the Einstein emission coefficient, and f_c and f_v are the electronic occupancies in the conduction and valence bands respectively i.e. the quasi-Fermi levels. When under low excitation this function can be approximated to a Boltzman distribution [4]:

$$f_c or\ f_v \propto exp\left[{}^{-E}/_{k_B T}\right] \tag{14}$$

The joint density of states for the conduction band and valence band in a type I three dimensional bandgap semiconductor is given by [3]:

$$D_j \propto (E - E_g)^{1}/_{2} \tag{15}$$

Substituting these values into the emission rate (equation 13), then the following equation for PL line shape is obtained [4]:

$$I_{PL}(E) \propto (E - E_g)^{1}/_{2} \exp\left[-{}^{E}/_{(k_B T)}\right] \tag{16}$$

This is the case when $E > E_g$, and zero otherwise when the incident photons have inadequate energy promote an electron across the forbidden bandgap. Differentiating this with respect to energy, the position at which the at which the lineshape is peaked E_{max} can be found [10]:

$$E_{max} = E_g + \frac{k_B T}{2} \tag{17}$$

This means that the measured peak energy extrapolated from any PL spectra is offset by $k_B T/2$ from the true peak energy.

This line shape expression is incomplete when looking at practical PL work as it does not allow for any energy values below the band gap. This is not the case in practical PL experiments. These transitions at energies less than E_g are called the

Urbach tail. This tail is created by imperfections in the semiconductor forming localised states within the bandgap from which carriers may recombine. The Urbach tail is given the form [11]:

$$\alpha(E) = A\, exp\left[\frac{\sigma}{k_B T}(E - E_g)\right] \tag{18}$$

Where A is a fitting parameter, and σ describes the slope of the tail. We now have two expressions for a practical PL line shape. There is a point at which they cross over, which can be shown to be $E_{co} = k_B T/2\sigma$. Thus the final PL line shape is given by:

$$\text{If } E \leq E_{co} \qquad I_{PL}(E) = A\sqrt{\frac{k_B T}{2\sigma}}\, exp\left[\frac{\sigma}{k_B T}(E - E_{co})\right] f_c f_v \tag{19}$$

$$\text{If } E \geq E_{co} \qquad I_{PL}(E) = A(E - E_g)^{1/2} f_c f_v \tag{20}$$

2.5 Absorption

Absorption spectroscopy is intrinsically related to the PL theory described above. While in the case of PL we are interested in the re-emitted photons generated from e-h recombination, for absorption we are interested in the amount of transmitted light which is dependent on the light being absorbed by the semiconductor to generate e-h pairs. The transmission is defined by the Beer-Lambert law [12]:

$$T(\hbar\omega) = \frac{I(\hbar\omega)}{I_0} = exp^{-\alpha(\hbar\omega)d} \tag{21}$$

Where I is the measured light intensity, I_0 is the initial light intensity, α is the absorption coefficient, and d is the depth of the semiconductor that the light is

penetrating. The absorption coefficient is then related to the bandgap in a direct bandgap semiconductor by [13]:

$$\alpha(\hbar\omega) \propto \frac{\sqrt{(E - E_g)}}{E} \tag{22}$$

This means by plotting α^2 *vs* E the points of changing gradient are features of the sample such as energy levels. Though absorption spectroscopy shows the same information as PL spectroscopy it has one large advantage; after the incident photons are absorbed there is no further dependence on carriers, meaning that the band edge is probed rather than the occupied energy levels. Absorption spectroscopy is a technique that can be used to probe band structure relatively free of carrier related features.

2.6 Photo-detector Operation

The basic principle of a semiconductor photo-detector is that an incident photon of energy greater than the bandgap of the material is absorbed, exciting and electron from the valence band of the material to the conduction band. Under even a small electric field this excited electron will drift creating a current. This basic principle of operation then leads to four key parameters of a photo-detector [14]: (1) the quantum efficiency, this determined how efficiently incident photons are converted to electron-hole pairs. (2) the responsivity, this determines the size of the generated current created by the optical power incident on the detector. (3) the detectivity, this determined how sensitive a detector is to a given wavelength. (4) the response time, this determines how quickly a detector can react to changes in the incident photons intensity.

2.6.1 Photodiodes

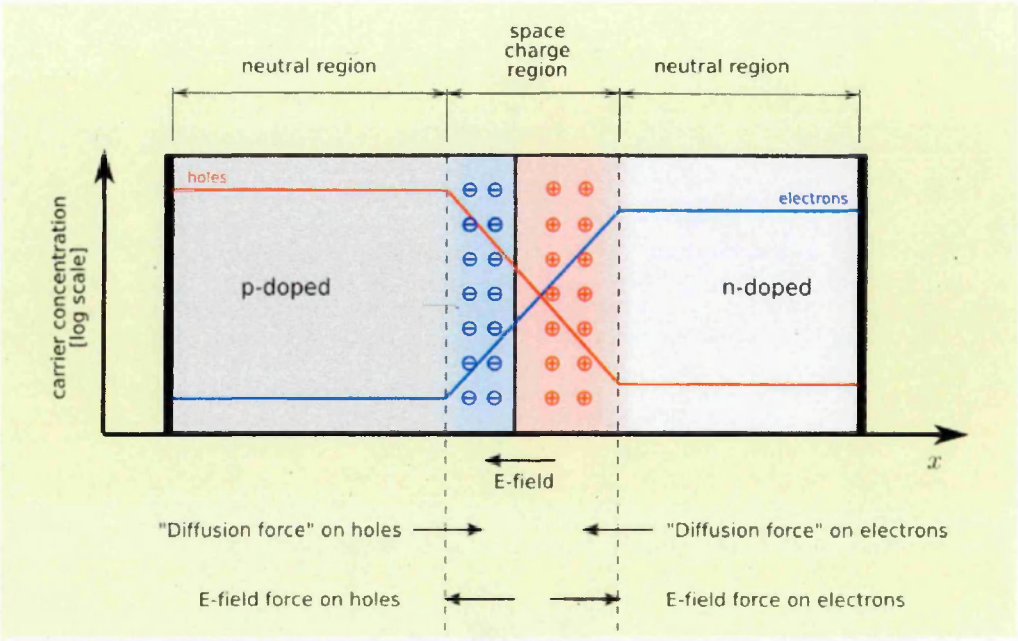

Figure 6: A diagram of a p-n junction showing the formation of a depletion region. Adapted from [15].

While there are other methods of photo-detection, the PIN photodiode is the method of interest for this work. When a p type semiconductor and an n type semiconductor are brought together, the excess electrons and holes would like to diffuse and fill the crystal uniformly, this would however disrupt the electrical neutrality of the crystal. Instead an electric field is formed creating a space charge free region called the depletion region, this is shown in figure 6. This depletion region creates the electric field required for free electrons to drift and create a current in the photodetector.

A p-n junction is often used with a reverse bias voltage, this reverse bias creates a strong electric field across the depletion region which increases the drift velocity of the carriers, it also increases the width of the depletion region making a larger area in which carriers can be generated for detection. A PIN diode has an intrinsic region between the p and n doped regions. Under reverse bias the electric field spans the intrinsic layer, increasing the volume in which the photon absorption can occur.

2.7 Photo-detector Dark Current Contributions

All good photo-detectors regardless of operational range or designed purpose must have a high sensitivity and low noise i.e. the SNR is large. The noise value of a photo-detector can be attributed to three main processes; diffusion current, generation-recombination current, and tunnelling current. This section will outline these methods of recombination.

2.7.1 Diffusion Current

In the non-depleted region of the semiconductor thermal carriers are generated. These carriers then diffuse towards the depleted region. The current caused by this diffusion is given by [14]:

$$I_{diff} \propto e^{-E_g/k_B T} \tag{23}$$

Where E_g is the bandgap of the semiconductor, k_B is the Boltzman constant and T is the temperature. This equation shows that the diffusion current is high for low bandgap materials such as InSb. To minimize the diffusion current most photo-detectors with a narrow bandgap are liquid nitrogen cooled (~77K) for operation.

2.7.2 Generation-Recombination Current

The generation-recombination current is caused by defect level states found within the bandgap of the material. Carriers "trapped" within these defect states can be promoted to the conduction band via optical or thermal excitation with energies less than E_g. The generation-recombination current is given by [14]:

$$I_{g-r} \propto We^{-E_g/2k_B T} \tag{24}$$

Where W is the volume of the depletion width of the semiconductor, E_g is the semiconductor bandgap, k_B is the Boltzman constant and T is the temperature. While similar to the diffusion current equation above, the generation recombination current depends on the volume of the depletion region unlike the diffusion current.

2.7.3 Tunnelling Current

When working with a high electric field for example a photo-detector under reverse bias, and geometrically narrow barriers, electrons can quantum mechanically tunnel from the valence band to the conduction band. The tunnelling current is given by [14]:

$$I_{tun} \propto EVexp\left(\frac{-\theta\sqrt{m}}{E}E_g^{3/2}\right) \tag{25}$$

Where E is the electric field, V is the applied reverse bias voltage, m is the effective mass of the electron, E_g is the semiconductor bandgap and θ represents the work function and is a material constant dependent on the barrier height.

2.8 Summary

In this chapter the relevant physics which is built upon is subsequent chapters is outlined. The density of states for different dimensionalities of material is covered along with the occupation of these states using the Fermi-Dirac function.

The different types of hetero-structures that can be formed by a binary material are briefly covered, followed by a discussion on how the material parameters are changed by forming a tertiary alloy e.g. the bowing parameter of the bandgap.

The theory behind the main spectroscopic techniques used in this work (PL and absorption) are covered, which follows onto the important parameters in designing a photo-detector, the basic principles of photo-detection operation and the sources of dark current.

2.9 References

[1] Neudeck and Pierret, *"Advanced Semiconductor Fundamentals"*, (2003)

[2] Prof. Stephen J. Sweeney, Univeristy of Surrey Level 2 Solid State Physics Lecture Notes, < http://personal.ph.surrey.ac.uk/~phs1ss/2SS/>

[3] C. Kittel, *"Introduction to Solid State Physics", Seventh Edition, (1996)*

[4] P. Y. Yu, M. Cardona, *"Fundamentals of semiconductors"*, (1996)

[5] P. Norton, *"HgCeTd Infrared Detectors"*, OPTO-ELECTRONICS REVIEW 10(3), 159–174 (2002)

[6] I. Vurgaftman et al., *"Band parameters for III–V compound semiconductors and their alloys"*, Journal of Applied Physics 89, 11, (2001)

[7] Y.P. Varshni, *"Temperature dependence of the energy gap in semiconductors"*, Physica 34, 1, 149–154, (1967)

[8] Coldren and Corzine, *"Diode Lasers and Photonic Integrated Circuits", (1995)*

[9] R. Fehse et al., *"A quantitative study of radiative, Auger, and defect related recombination processes in 1.3-μm GaInNAs-based quantum-well lasers"*, Selected Topics in Quantum Electronics 8, 4, (2002)

[10] Z. M. Fang et al., *"Photoluminescence of InSb, InAs, and InAsSb grown by organometallic vapour phase epitaxy"*, Journal of Applied Physics 67, 7034, (1990)

[11] R. A. Smith, "Semiconductors Second Edition", Pg 485-492, (1978)

[12] J. R. Dean, *"Atomic Absorption and Plasma Spectroscopy (Second Edition)"*, (1998)

[13] E. Rosencher et al., *"Optoelectronics", (2002)*

[14] Optical Society of America, *"Handbook of Optics, Volume 1: Fundamentals, Techniques, and Design. Second Edition"*, (1994)

[15] P-N Junction Diagram, available through GNU free documentation license, Accessed 2013,

<http://en.wikipedia.org/wiki/File:Pn-junction-equilibrium.png>

Chapter 3 - Experimental Techniques

3.1 Introduction

In this research two main spectroscopic techniques were used, photoluminescence and absorption. The theory behind each technique is discussed in the previous chapter. All of these spectroscopies were performed with a common experimental setup that will be detailed in this chapter.

All of the semiconductors investigated in this thesis are designed with target emission wavelengths in the mid-IR, therefore care must be taken when selecting appropriate apparatus. Many of the optical components suitable for work in the visible region, such as glass lenses are not suitable for work in the mid-IR as they have poor transmission outside of the visible spectrum. The change to infrared suitable apparatus is done to firstly minimise the amount of light lost to absorption in each piece of apparatus to ensure that sufficient light emitted actually reaches the detector. Secondly, so that there are no absorption peaks caused by the apparatus that may be mistaken for features of the semiconductor being examined. Thirdly, to ensure that the apparatus in question, such as the detector being used, is responsive in the wavelength region of interest.

3.2 Czerney-Turner Grating Monochromator

The key piece of apparatus used in all of the experiments is the monochromator. Its function is to take a broad spectrum of input light and output a narrow bandwidth of light. The type of monochromator used for these experiments is a Czerny-Turner type grating monochromator the operation of which is shown in figure 1 and detailed below.

A broadband light source is focused onto the first slit S_1. This light is then collected by the collimating mirror and directed onto a rotatable grating. The broadband light is then separated into a continuum of dispersed beams that are directed onto the focussing mirror. The focusing mirror then focuses the dispersed light on the second slit S_2. The wavelength band of the light directed at slit 2 is selected by the angle at which the rotating grating is positioned. Czerny-

Turner gratings are controlled by a computer program which allows the monochromated light to be scanned through producing a spectrum of light intensity vs wavelength. The resolution of the monochromator is controlled by the slit width, with narrower slit widths producing a finer resolution. Wide slits provide a stronger signal at the expense of resolution.

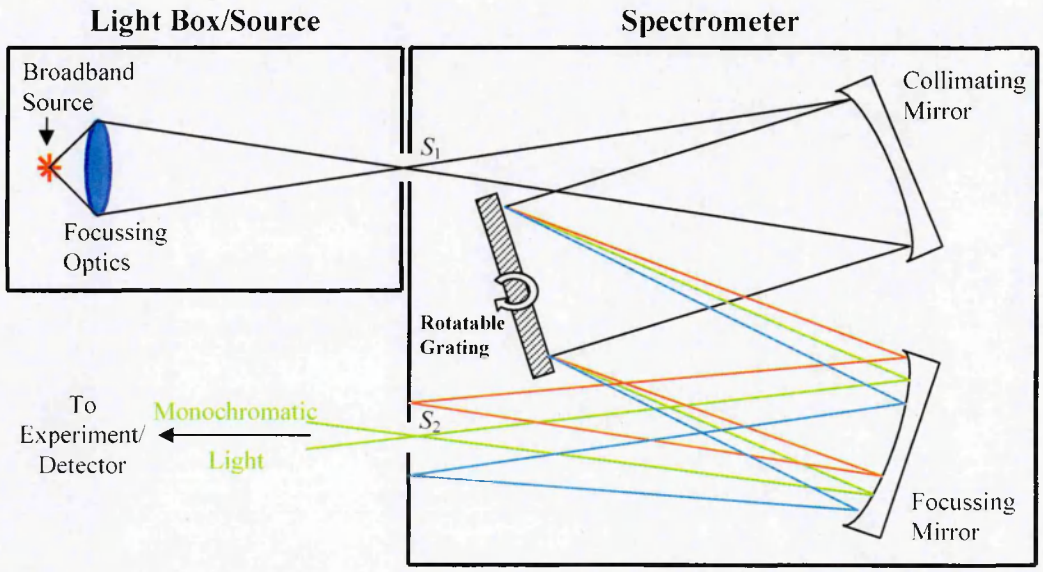

Figure 1: The schematic operation of a Czerny-Turner monochromator adapted from [1].

3.2.1 Triax 320 details

The specific type of monochromator used for the experiments in this thesis is the Triax 320 spectrometer produced by Jobin Yvon, a division of Horiba. The Triax 320 is a modified Czerny-Turner design monochromator. The primary difference in design is that the rotatable grating is replaced by a rotatable turret that allows computer controlled selection of one of three possible gratings. The grating in use determines the operating range of the monochromator, and this three grating turret allows a much wider wavelength range of operation than a one grating system, from the visible region to 30μm depending on the selected grating. The details of the available gratings in the Triax 320 and their operational range is shown in table 1. Though the Triax 320 has this wide wavelength range of operation, it does like all grating monochromators require a long pass filter to remove any higher order wavelength light, as shown by the grating equation [2]:

$$dsin\theta = n\lambda \qquad (1)$$

Where d is the grating spacing, θ is the angle at which the light is being measured, and n is an integer representing the order of the light. The filter must be selected so that light of order $n > 1$ in the range of interest is removed. The commercially available filters for the mid-IR region have a wavelength range much shorter than the operational range of the Triax. Details of the gratings used in these experiments can be found in section 3.3.3. It should also be noted that the reflection gratings are used in first order.

The other design difference from a standard Czerney-Turner monochromator is the inclusion of additional entrance and exit ports, shown in figure 2. These additional ports allow for the monochromator to be used in different configurations by using a computer controlled mirror to select the ports to use. It should also be noted at this point that there is no difference in operation when using the Triax 320 in reverse, i.e. using the entrance port as an exit port and vice versa. This fact coupled with the additional ports allows for virtually simultaneous spectra of PL and PR to be taken without disturbing any optics and only changing an internal mirror position [4].

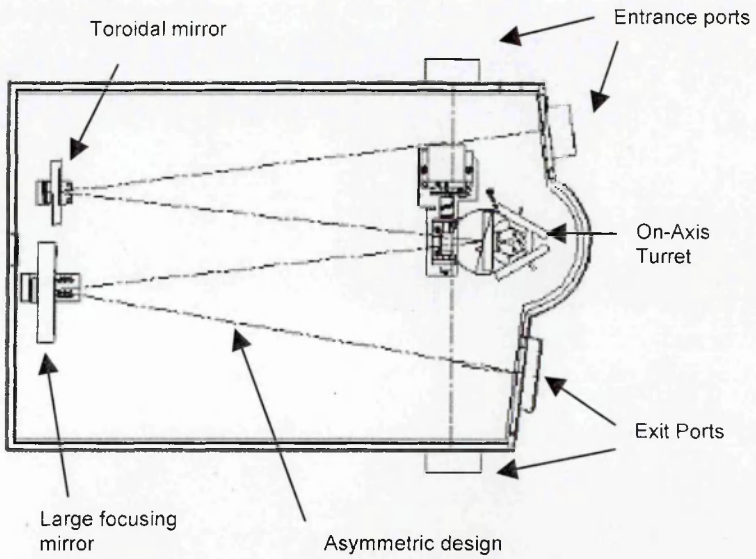

Figure 2: Triax 320 additional port design adapted from [3]

The bulb being used for the absorption experiments labelled as the broadband source in figure 3 ,is a commercially available Osram low voltage halogen lamp. The lamp is a tungsten filament surrounded by krypton gas, all encased in quartz glass. The bulbs listed output is 100W at 12V. Though there is no output spectrum available from the manufacturer, it is assumed that the bulb follows a typical blackbody spectrum with transmission features similar to the quartz window cryostat discussed later.

Grating Blaze (μm)	Operating Range (μm)	Grooves per mm	Dispersion (nm/mm)
1.5	1-3	600	5.28
5	3-10	150	2.12
15	10-30	60	52.8

Table 1: Triax 320 grating details [3]

3.3 Considerations for working in the Mid-IR

It was briefly mentioned earlier that special consideration should be taken when selecting apparatus to use in the mid-IR optical regime. This section details each apparatus used in the optical setup. In the case where no specialist mid-IR apparatus could be sourced then it will be shown that any mid-IR absorption caused can be accounted for when normalising the measured spectra.

3.3.1 Normalisation of the spectra

It is important to define normalisation of the spectra at this point and how it is practically performed. Normalisation is the process of trying to remove any features of the apparatus that have affected the measured output spectra, this is called the system response. When measuring any sample such as an LED the measured spectrum is:

$$m(\lambda) = s(\lambda)\, R(\lambda) \tag{2}$$

Where m(λ) is the measured spectrum, s(λ) is the sample spectrum and R(λ) is the system response. To remove this system response term, the sample being measured is replaced with a broadband light source of known output spectrum. In all of the experiments performed in this thesis the normalisation was performed with a Bentham light bulb with known output spectrum. The spectrum measured using the Bentham bulb in place of the sample is then:

$$m'(\lambda) = R(\lambda)\, B(\lambda) \tag{3}$$

Where m'(λ) is the measured spectrum and B(λ) is the Bentham lamp spectrum. As the Bentham Spectra is known then both sides of the equation can be divided by the Bentham Spectrum to gain the system response term:

$$R(\lambda) = \frac{m'(\lambda)}{B(\lambda)} \tag{4}$$

Substituting (4) into (2) then gives:

$$m(\lambda) = \frac{s(\lambda)m'(\lambda)}{B(\lambda)} \tag{5}$$

Rearranging this to find the "true" sample spectrum gives:

$$s(\lambda) = \frac{m(\lambda)B(\lambda)}{m'(\lambda)} \tag{6}$$

In the following sections the normalisation process is discussed and the extent to which is removes the absorption caused by each piece of apparatus from the measured spectra.

3.3.2 Atmospheric Absorption

The largest source of uncertainty when measuring spectra in the mid-IR regime is atmospheric absorption. Figure 3 shows the absorption coefficient of several

gases that absorb in the mid-IR region. While these absorption coefficients were measured in a 100% concentration sealed environment at 1 atmosphere[5] the features are still present at lower gas concentrations. Figure 3 shows a very broad range of wavelengths from 2μm to 16μm. The experiments for this thesis are in a more specific wavelength region of 2μm to 4μm. The composition of the atmosphere at sea level where these experiments were performed is: 78.09% nitrogen, 20.95% oxygen, 0.93% argon, 0.039% carbon dioxide and trace amounts of other gases [6]. This means in the 2μm to 4μm region the absorption features that will typically interfere with measured results are water and carbon dioxide.

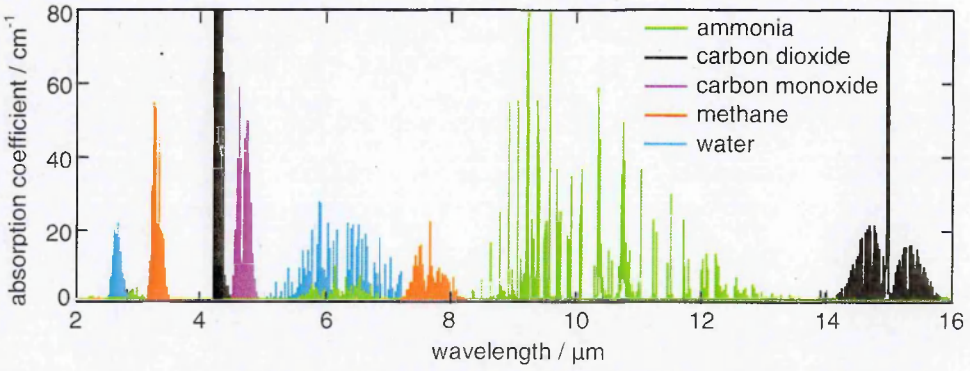

Figure 3: The absorption windows of atmospheric gases, adapted from [5].

While normalisation of the spectra should result on the removal of these features the practical application of normalisation finds this is not always the case due to their spectral abruptness. Both the spectra for water vapour and carbon dioxide gas are well studied and the absorption strength in the 2.4μm -3μm region is shown in figures 4 and 5 respectively. It should be noted that there are no features for either water or carbon dioxide in the 3μm - 4.15μm region. These figures show that there is a complex set of tightly spaced individual absorption peaks. This means the normalisation process will have difficulty in totally removing these features unless the sample spectrums resolution is of a similar scale.

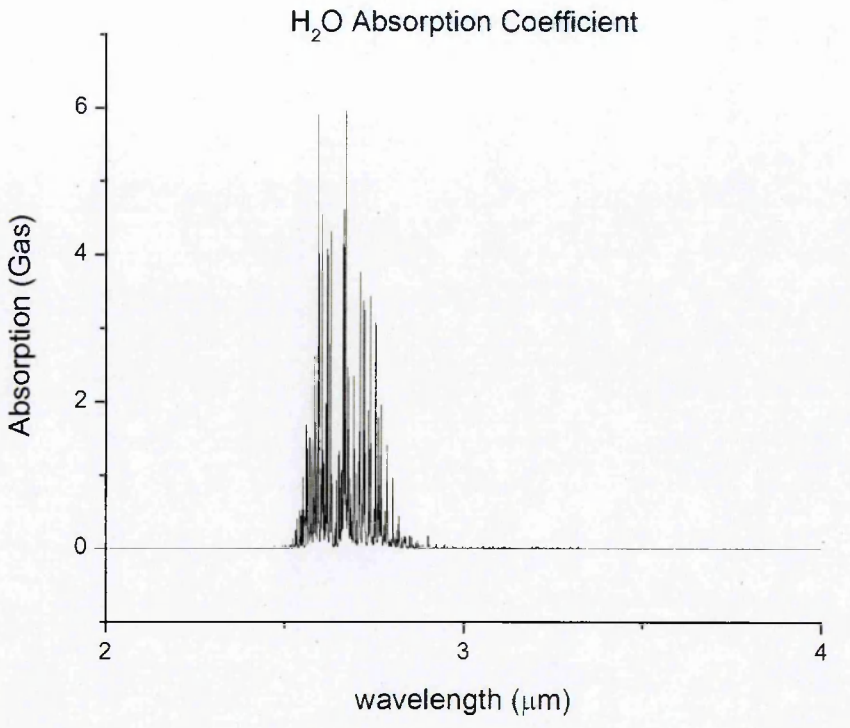

Figure 4: Detail of the water absorption features found between 2μm - 4μm, adapted from [7].

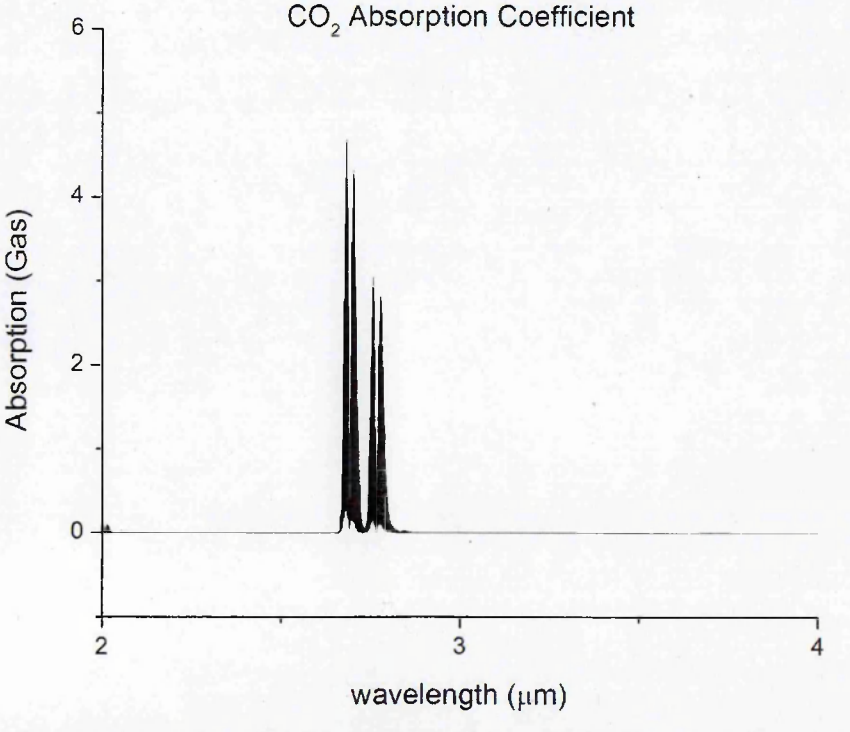

Figure 5: Detail of the carbon dioxide absorption features found between 2μm - 4μm, adapted from [8].

An additional problem when trying to normalise out these gas features is the concentration that the light is passing through. Though the distances between each piece of apparatus will not change, things like the concentration of water vapour in the air will change as the laboratory's humidity changes. While these issues are controlled up to a point by climate control like air conditioning, they are never completely removed.

3.3.3 Triax transmission

The operation of the Triax 320 was discussed in an earlier section, where is was stated that the Triax 320 had three selectable gratings on its rotatable turret. For the experiments in this thesis only gratings one (visible to 3μm) and two (3μm to 10μm) were used, and while the operational range of each is given in table 1, the grating efficiency is not constant over the entire range.

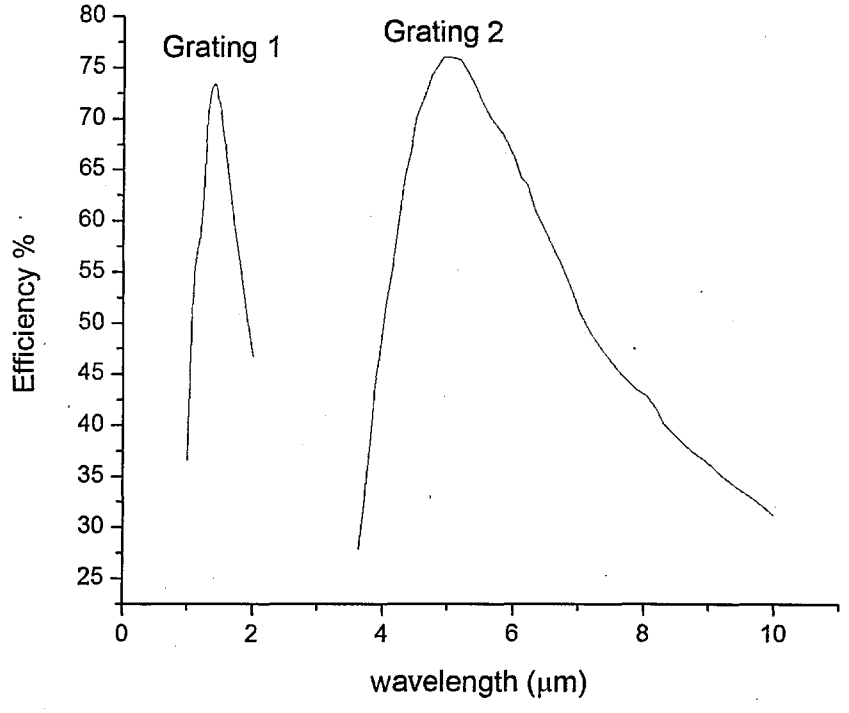

Figure 6: The theoretical efficiency curve of the Triax 320's grating 1 and 2. Adapted from [9].

Figure 6 shows the theoretical efficiency of grating one as provided by the manufacturer Horiba. The three curves represent the different available gratings

that cover the same wavelength range, and the dash-dot curve is the one used for these experiments. The listed peak efficiency is 80% at 1.5μm. Above and below this value the efficiency drops off. Though the maximum wavelength shown is only 2μm with an efficiency of 65%, the grating has been used in practice for measurements up to 3μm while still producing accurate spectra when compared with a Bomem FTIR working optimally in this range.

Figure 6 also shows the theoretical efficiency of grating two as provided by the manufacturer Horiba. The listed peak efficiency is 75% at 5μm, below which this drops off sharply and above which it drops off slowly. Again, although the spectrum only shows values down to 3.6μm where the efficiency is 30%, it has been successfully used down to 3μm, providing continuous wavelength coverage between gratings one and two.

From these spectra it can be seen that in the 2μm to 4μm region the Triax 320 is not very efficient regardless of the grating being used and by extrapolation of the curves a maximum of 20% of the input light reaches the output port. This low amount of output intensity compared to the input intensity will mean all spectra taken in this range will have lower SNR than expected.

3.3.4 Long Pass Filters

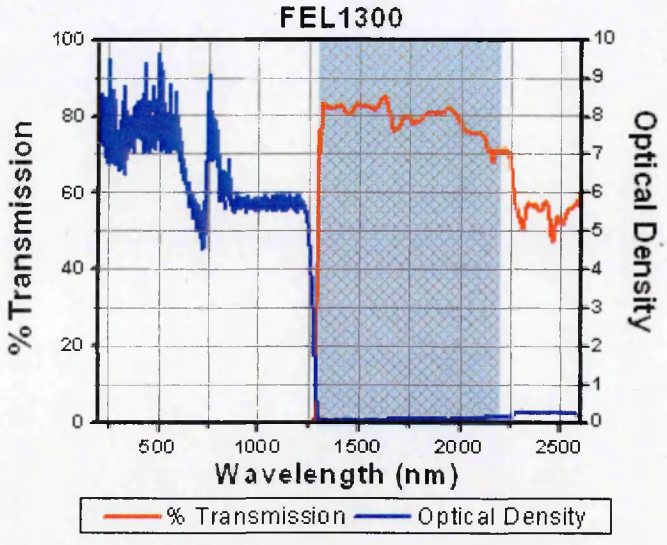

Figure 7: 1300nm Filter (FEL1300) supplied by Thorlabs [10].

As stated earlier in the chapter, when using a grating type monochromator higher orders of short wavelength light will also leave the output port. To remove these higher orders of light a long pass filter is used. While the use of a long pass filter removes these unwanted orders of light they do introduce an additional non-constant transmission factor when used over a long wavelength range. For this work there are three regions that long pass filters are required to cover; these regions are the same as the target wavelengths of the semiconductors measured. The quantum dots are target wavelength ~2μm at 300K. The type II superlattice structure is target wavelength ~4μm at 300K, though as will be discussed later, the type II superlattice investigations were performed at high pressure resulting in a wider wavelength coverage of 2μm to 4μm for a single filter to be used. The high-pressure studies also required a suitable near-IR pressure calibration sample with known change in emission wavelength with pressure; the gauge chosen emitted around 1.5μm and so a filter between 1μm and 2μm was chosen.

The filter chosen for the quantum dots study was a Thorlabs (FEL1300) 1300nm long pass filter. The transmission spectra of which is shown in figure 7. This model was selected as it has a transmission of between 70% and 85% when being used between 1350nm and 2200nm. Above 2200nm the transmission drops to 50% and below. The transmission in the rejection region is 0.01% [10]. Figure 7 does show that although the transmission value is high it is not constant. This means that normalisation of every spectra will be required to remove these features, and again accurate intensity values for comparison.

As the type II superlattice studies had a longer wavelength and also required a broader range due to the pressure studies being performed, more consideration in the selection of filter was required. The two options available that would cover the required region are of 1.7μm Germanium (Ge) long pass filter, and a 1.6μm Gallium Antimonide (GaSb) long pass filter. The transmission of each of these filters when measured by liquid nitrogen cooled InSb detector is shown in figure 8. Also shown in figure 8 is a custom-made 2.3μm long pass filter (IR), this is to illustrate that although it has a high transmission (greater than 80%) it also has a

large amount of oscillation in the amount of transmission even over this small wavelength range.

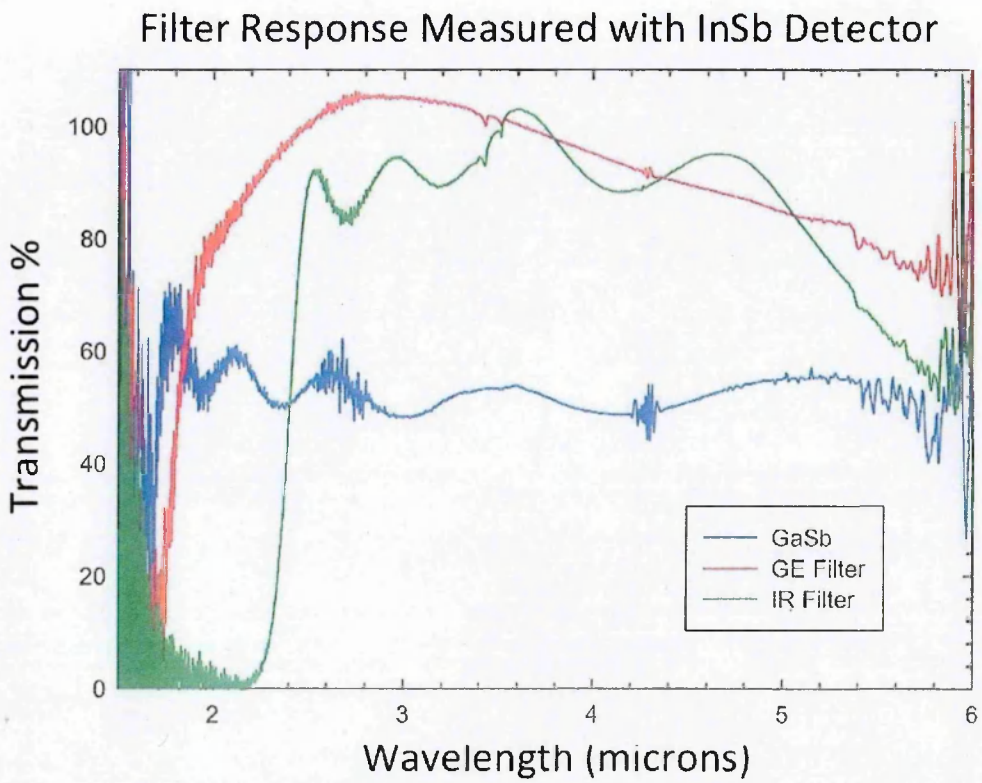

Figure 8: Transmission of a Ge, GaSb and commercial IR filters from Thorlabs measured using a liquid nitrogen cooled InSb detector.

The Ge filter was used for the final experiment as it has the higher transmission across the required wavelength, and the transmission spectrum is slowly varying with wavelength. However, when comparing the extreme of 2μm the transmission has dropped to 80% compared to the peak value of 100% at 2.8μm. While still an excellent transmission value this experiment had slightly unusual requirements as will be discussed in a later chapter, and with higher pressure (shorter wavelength) the measured signal was expected to decrease. This expected decrease could be mistaken for the decrease in filter transmission. Although the transmission is lower for the GaSb it was still considered for use as the variation between maximum and minimum transition was a 10% drop, while for the Ge filter is is found to be 20%.

The high-pressure gauge filter selected was a 1100nm filter from Thorlabs (FEL1000) the transmission of which is shown in figure 9. This filter has 80% or greater transmission up until 2μm. The transmission in the rejection region is 0.01% [12]. Although not constant with wavelength any features should be removed during normalisation.

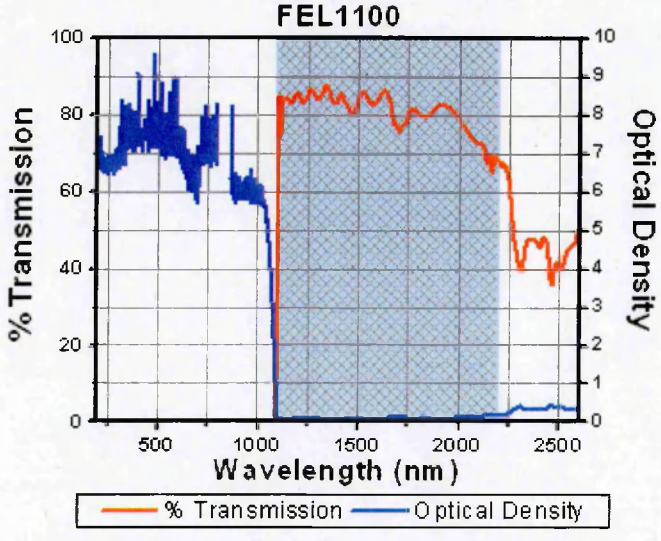

Figure 9: 1100 filter supplied by Thorlabs [12].

3.3.5 Lens Composition

There are two choices for focusing optics in the experimental setup; lenses and parabolic mirrors. In this work lenses were chosen for their simplicity of use. When using lenses fine tuning individual sections of the optical arrangement is done with ease, as each lens can be independently focused when light passing between the lenses is collimated. The negative aspect of using only lenses requires the apparatus to be arranged in a linear setup, as the light beams direction cannot be changed at right angles without the use of a mirror, in the same way that can be achieved with mirrors. When using parabolic mirrors, optical adjustments are much more difficult as each piece of the focusing optics also changes the light beams path by 90°. So although the light is collimated between mirrors, moving a mirror to achieve a good focus required movement of the preceding mirrors. The advantage of using mirrors is that they require far less space than lenses.

While the issue of space may seem like a luxury, this also reduces the distance travelled by the light beam. This reduction in the beam path will maintain more light intensity between the source and final destination due to beam divergence. Additionally there is some light absorbed and reflected by the lenses, however their ease of use heavily outweighs these issues.

3.3.5.1 Glass

While glass is the most commonly available and cheapest material to manufacture lenses from, not all types of glass are suitable for use in the mid-IR. Figure 10 shows the compositions of glass used for optical components. A standard optical lens is usually made of crown glass, BK7 and B270. These have excellent (90%) transmission in the visible region but a very sharp drop in transmission at 1.6μm, by 2.3μm the transmission is negligible. This makes them unsuitable for the mid-IR measurements.

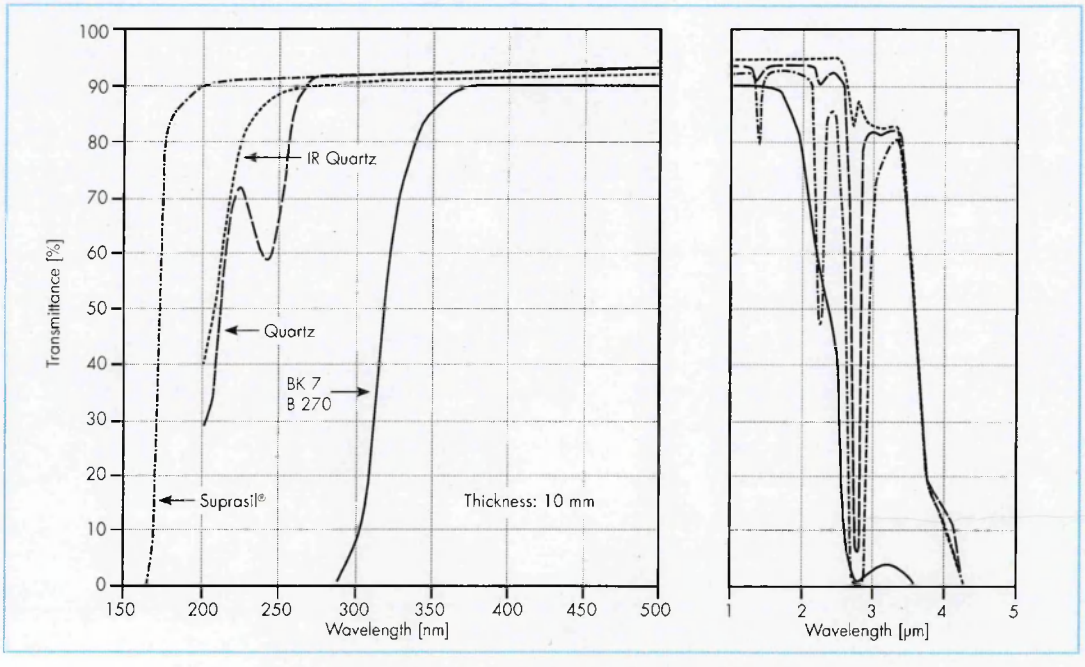

Figure 10: Typical optical glass transmissions, adapted from [13].

Quartz and IR Quartz are more suitable alternatives for work in the mid-IR with good transmission values above 80% up to 3.5μm. While this makes them suitable for use in the quantum dot section of this thesis they are less useful at longer wavelengths.

3.3.5.2 Calcium Fluoride

A far more suitable lens material for use in the mid-IR is Calcium fluoride. The transmission spectrum of which is shown in figure 11. The transmission is above 90% between 0.2μm to 7μm, making it ideal for use in the visible and mid-IR region. There are however two large disadvantages of using calcium fluoride lenses instead of glass. The first is that calcium fluoride lenses are significantly more expensive than glass. At the time of writing this thesis to purchase the equivalent lens from Edmund Optics would cost eight times more for calcium fluoride compared to glass.

The second disadvantage of calcium fluoride is that they are hygroscopic, meaning that they are sensitive to any moisture in the air. Exposure to moisture will cause them to become cloudy and unusable for optical measurements.

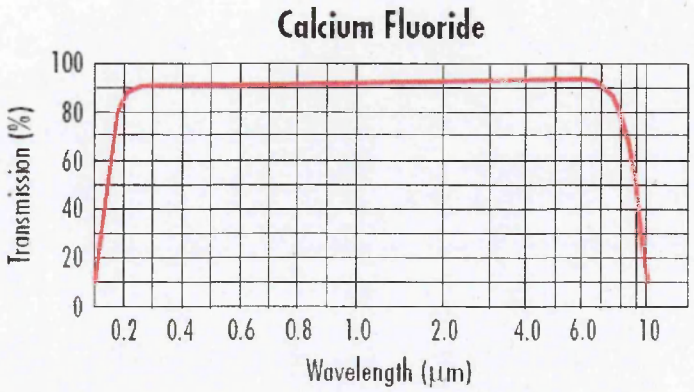

Figure 11: CaF2 Transmission adapted from [14].

3.3.6 Cryostat transmission

One component in the experimental setup not designed for mid-IR use, that cannot be substituted for a more suitable piece is the cryostat window. The cryostat used for this experiment has 360° optical access, and a large internal cavity as shown in figure 12. This is used in this work for mounting the sapphire ball cell inside the cryostat. Something that would not be achievable with a standard liquid nitrogen bath cryostat. The window is made from quartz, and has

been measured several times due the importance of having accurate knowledge of its transmission spectrum.

Figure 13 shows the manufacturer supplied transmission spectrum of the quartz window. It can be seen from the spectrum that there is a sharp drop in the transmission at 2.75μm and it decreases substantially at 3.4μm.These features are smoothly varying with wavelength and are removed during the normalisation process. It is worth noting however that this single piece of apparatus limits the ability to measure samples of emission wavelength greater than 4.75μm where this window no longer allows significant transmission.

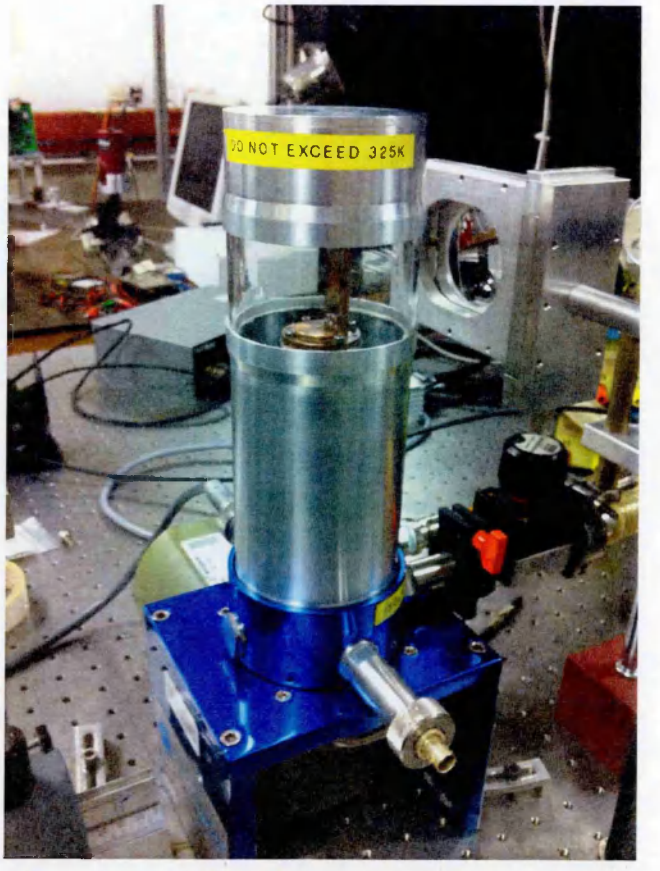

Figure 12: The 360° optical access cryostat used in this work.

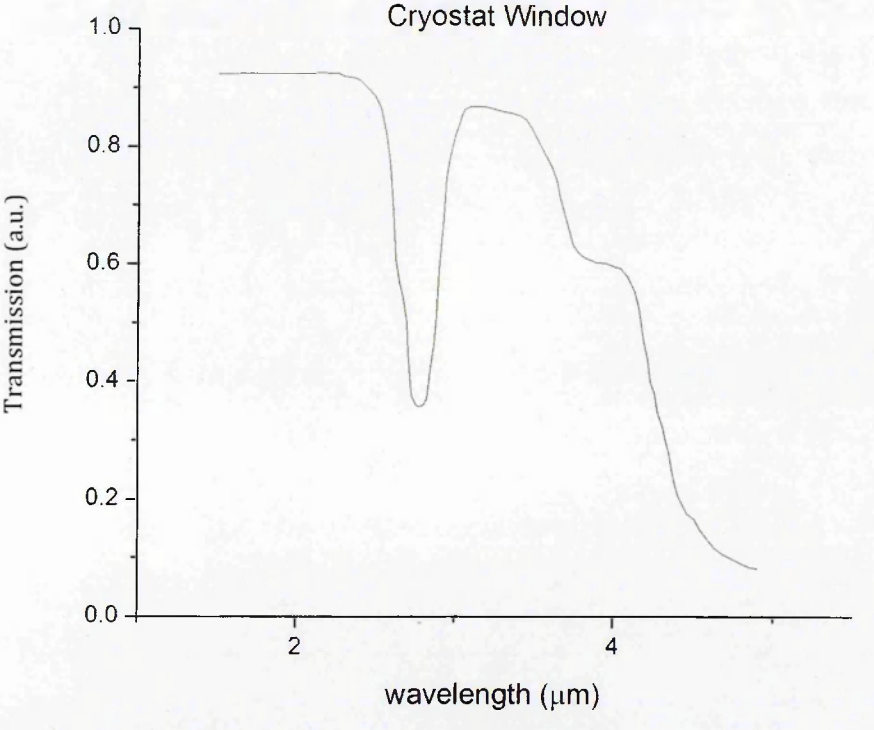

Figure 13: The cryostat window transmission, manufacturer data supplied by [15].

3.3.7 Detectors

During this experiment there are two types of InSb detector used. The option of an MCT detector was available but not implemented because its maximum response lies at ~18μm and the longest measurement wavelength in this experiment is 4μm, At 4μm the MCT is working at 10% of its maximum response. In contrast both InSb detectors have a 90% peak response at this wavelength. The reason two InSb detectors are used is primarily to allow the simultaneous measurement of PL and PR without disturbing the optical setup. Secondly they are slightly different in design as outlined below making them more suited to the measurement task assigned. They will be referred to as red and blue to differentiate between them, due to the colour of their casing.

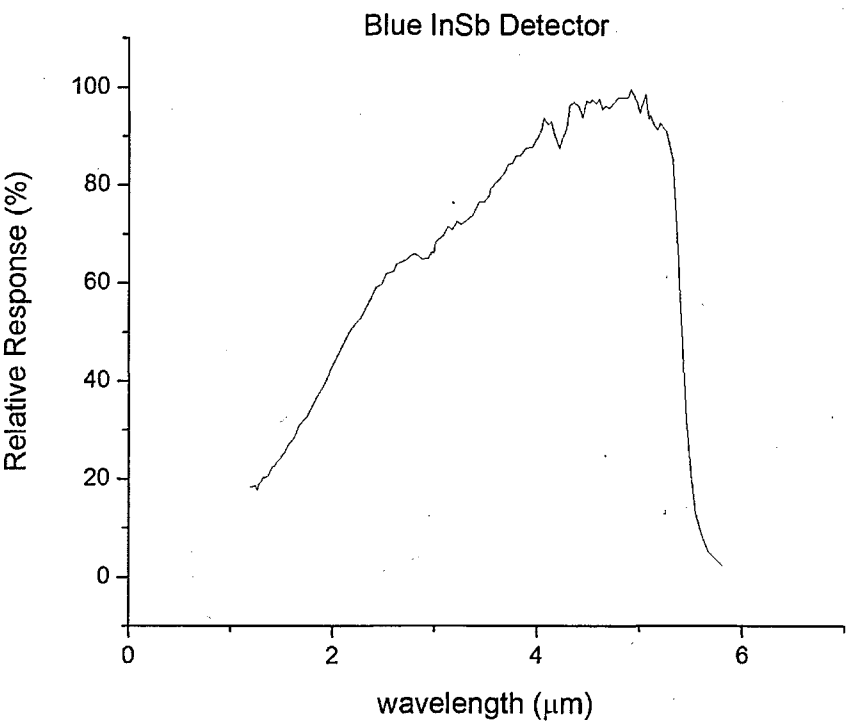

Figure 14: The response curve of the blue InSb detector [16].

The blue "Cincinnati" is a liquid nitrogen cooled InSb detector with a bottom window design, meaning you have must use a parabolic mirror to direct the light beam into it. While not convenient to use because of this bottom window design, it does have a large ~1cm^2 active element. This detector is used for the PL measurements taken in this thesis as this large active element allows for

collection of the most light. The detectors response is shown in figure 14. The maximum cut-off point for the detector is 5.56μm, well in range of the requirements of this work. It has a broad range of wavelengths where the response is above 90% of maximum, and has also been used down as far at 1.2μm where the response falls to 20% of maximum.

The disadvantage of using this detector is the sharp features it displays in the spectra, these are particularly prominent above the 4μm region. However, as the maximum measured wavelength is expected to be 4μm then they should not present a problem with any measured spectra.

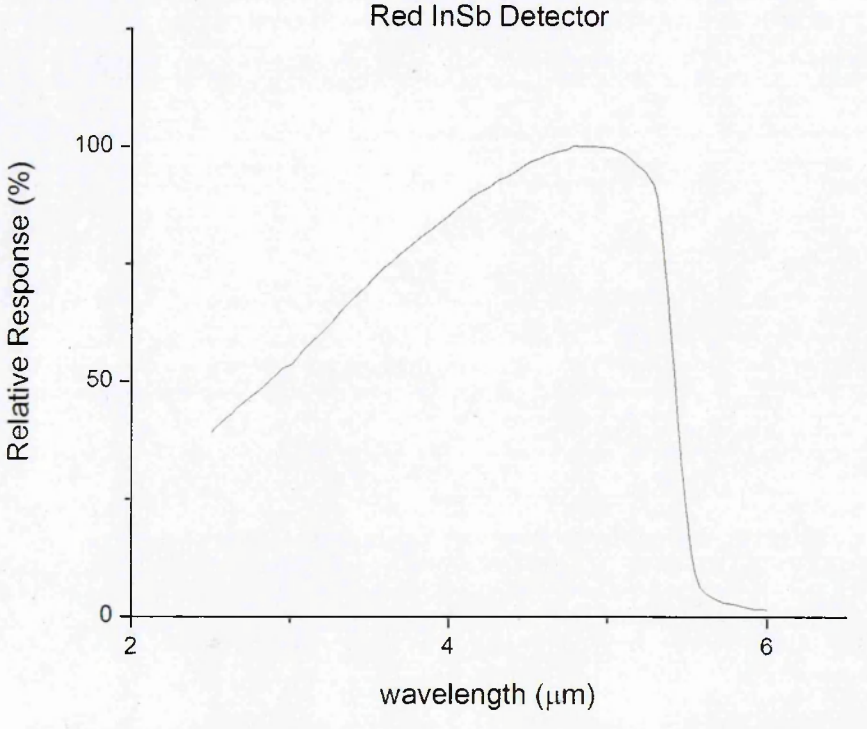

Figure 15: Response curve of the red InSb detector, adapted from [17].

The red InSb detector is liquid nitrogen cooled and has a side window design making it much easier to fine adjust as there no parabolic mirror needed, and being able to see directly where the light beam is hitting the active element. It also has a DC coupled preamplifier that outputs the measured signal as DC rather than AC allowing the simultaneous measurement of the ΔR and R signal during

PR experiments. The one disadvantage is the much smaller active element of the detector compared to the blue, being ~0.5cm^2 leading to less light collection.

The response curve for the red InSb is shown in figure 15. It has the same operational range as the blue InSb including the same cut off at 5.56μm and efficiency peak range. The spectrum does not have the same sharp peaks though, again making it more suitable for PR measurements

3.3.8 Sapphire Ball

While a full explanation of the operation of the sapphire ball cell is to follow, it is important to mention the transmission of sapphire in the mid-IR. Figure 16 shows the transmission spectrum of synthetic sapphire which is used to create the balls in the cell. The transmission is above 80% between 0.4μm and 4μm. The response between 2μm and 4μm is varying. This should not pose a problem to remove via normalisation as the curve is smoothly varying with wavelength.

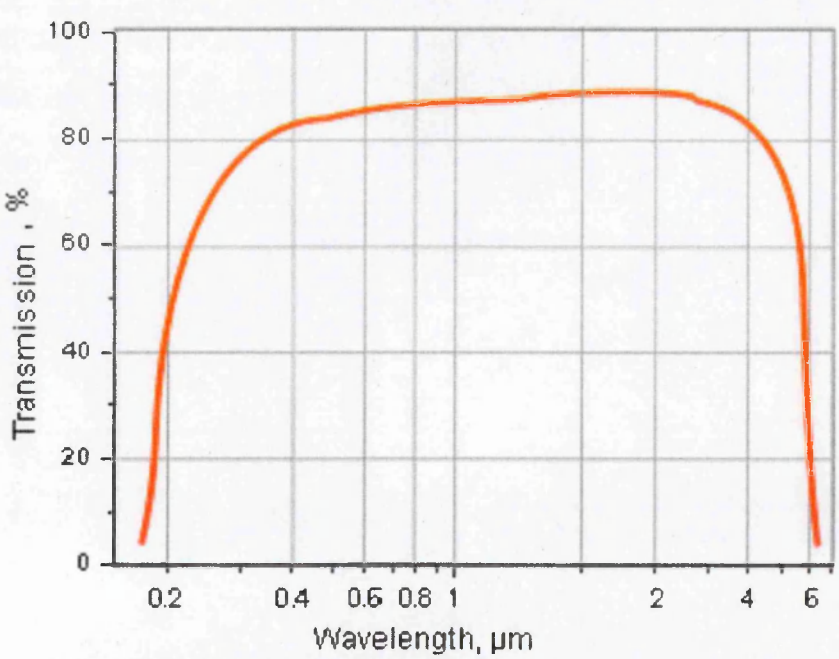

Figure 16: Transmission of synthetic sapphire, adapted from [18].

3.4 Temperature Control

The temperature control for all of the experiments was provided by a closed cycle helium cryostat working in competition against a proportional-integral-derivative (PID) controlled heating element. The lowest possible temperature to which the cryostat system can cool is 9K. The lowest temperature used for any measurement was 10K, going lower than this temperature will not activate the heating element. This means there is the possibility of a temperature gradient inside the cryostat. All of the PID settings for maximum stability had been previously experimentally determined.

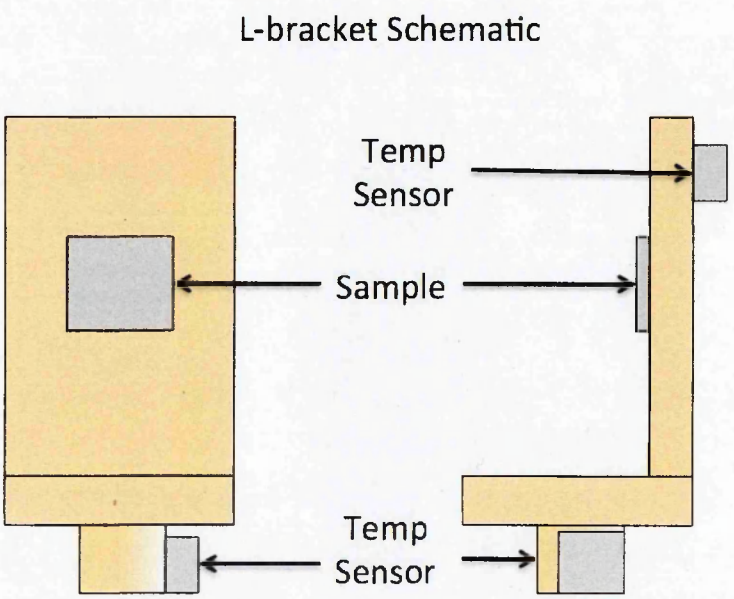

Figure 17: A schematic of the temperature sensors position relative to the sample, on the L-bracket holder.

The heating element is positioned directly below the L bracket to which the sample was mounted. There are two temperature sensors, one mounted on the L bracket above the sample, and one mounted on the L bracket below the sample, this is shown in figure 17. The position of these sensors allows one to determine when the cryostat chamber is at the same temperature with no gradient in temperature across the sample. This became especially important when using the sapphire ball cell, as it has a much larger thermal mass than a semiconductor sample. This twin temperature sensor approach allows one to see when the cell is at the same temperature as the chamber.

3.5 Photoluminescence

To actually perform PL the apparatus is configured as shown in figure 18. The Triax 320 is used in "reverse" mode for this experiment, with the input port being used as an output and vice versa.

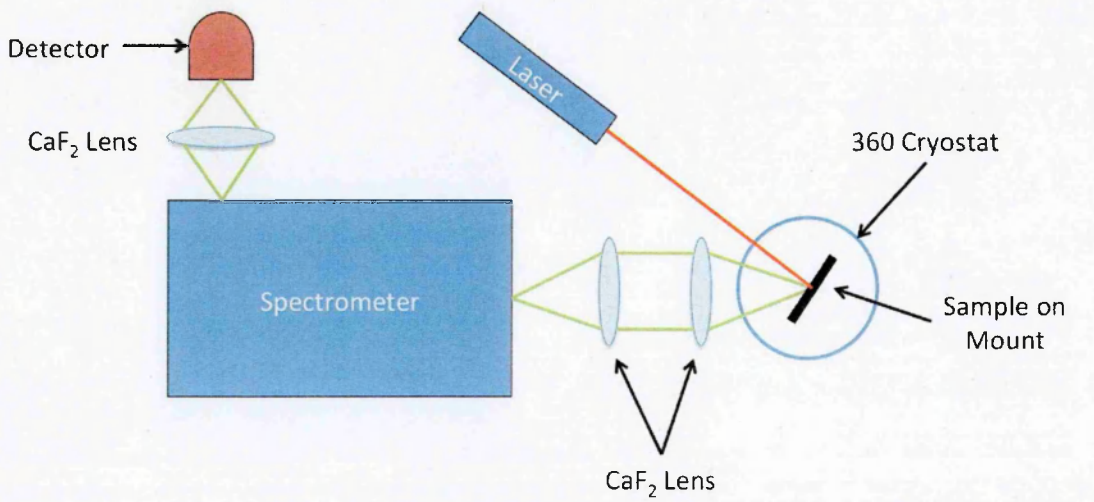

Figure 18: The experimental setup when performing PL measurements.

The sample is mounted on a copper "L" bracket inside the 360° cryostat. The sample is attached to the copper bracket via silver dag that allows for good thermal and electrical contact. The sample temperature is monitored via a temperature probe attached to the copper "L" bracket behind the sample mounting position. The cryostat chamber is evacuated, and then cooled to the required temperature. Cooling is achieved via the cryostat pump working against a heating element beneath the copper "L" bracket. To eliminate any possible condensation the chamber is evacuated to a vacuum of $1x10^{-3}$ mbar.

A chopped laser is used to excite the e-h pairs in the semiconductor. In this experiment there were two lasers available. The first is a BWTech diode laser, of wavelength 808nm and power 0-450mW [19]. This laser power may be current tuned and modulated. The laser beam is directed at the sample by way of an optical fibre, however the beam dispersion is quite large. This makes the laser ideal for power dependent measurements where a small beam spot size is not required, but where power control is important.

The second laser used is a ND:YVO_4 laser [20], of wavelength 1064nm and power 100mW. This laser is constant power, and has a very low beam divergence. This laser does not have an electrical chopping facility and requires the use of a mechanical chopper. This makes it ideal for experiments where beam accuracy is required such as the sapphire ball experiment or for very small wafer pieces where the 808nm laser would overlap the sample. It should be noted that both of these lasers pass through the cryostat window and sapphire ball cell with 90% transmission.

Once the sample has been excited by the laser, the e-h pairs recombine and any photons radiated are collected by the first CaF_2 lens. The output light beam is collected by the first CaF_2 lens is now collimated and directed on the second CaF_2 lens which focuses the beam onto the spectrometer's input port. The beam is monochromated by the spectrometer and directed out of the output port. This monochromated beam is then collected by another CaF_2 lens and focused onto the detector element. The detector signal is received by a lock-in amplifier so only light of the same frequency as the laser chopping frequency is recorded by the computer, this increases the signal to noise ratio of the measured spectrum.

The spectrometer is computer controlled and will scan through the desired wavelength range in steps of the desired wavelength. In this way a spectrum is then collected and outputted for later use. This process flow is shown in figure 19.

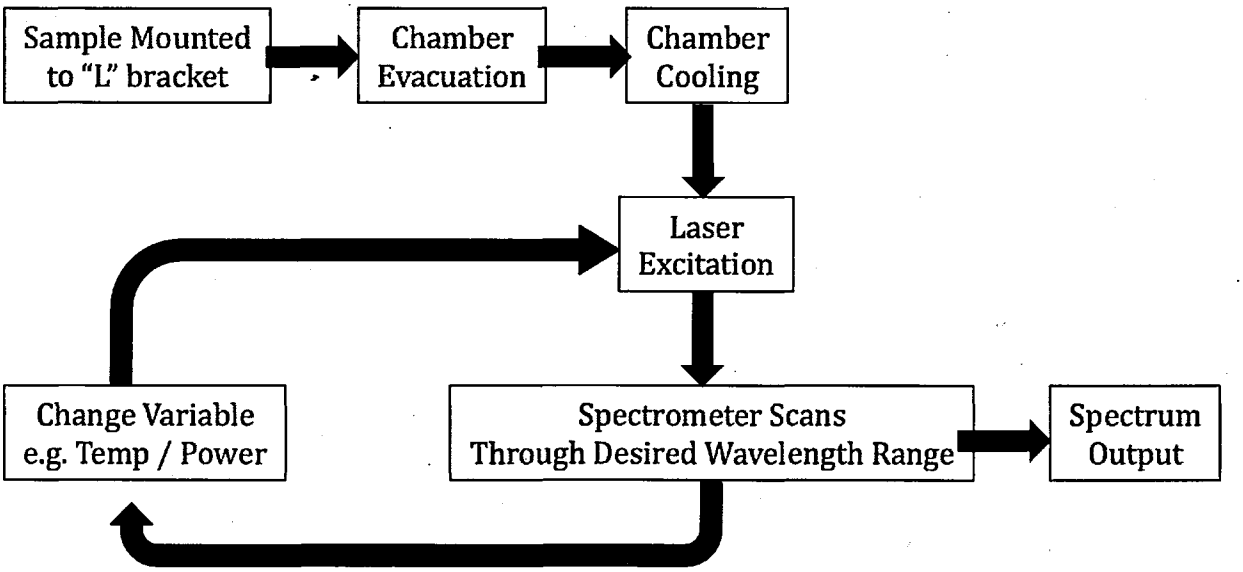

Figure 19: The process flow when performing PL experiments.

3.5.1 Pressure Dependent Photoluminescence

With addition of a sapphire ball cell to the experimental PL setup outlined above then it becomes possible to study a semiconductor with varying temperature, power and pressure. This gives further information about the sample band structure and is discussed in chapter 5 to determine the position of a defect level above the conduction band edge in a type II superlattice system.

3.5.1.1 The Sapphire Ball cell

The sapphire ball cell is a compact high-pressure system designed as an alternative to the diamond anvil cell [21]. The sapphire ball cell's main advantage over the diamond anvil cell is its ease of use; unlike the diamond anvil cell it does not require the sapphires to be perfectly parallel to function properly [22]. Additionally the cost of replacement sapphires is much cheaper than the cost of replacement diamonds. The largest disadvantage of the sapphire ball cell is that the pressure range achievable is much less than that of the diamond anvil cell ~30kbar compared to ~100kbar due to the larger sampl space in the sapphire ball cell. However, this pressure range is more than adequate for the studies described here.

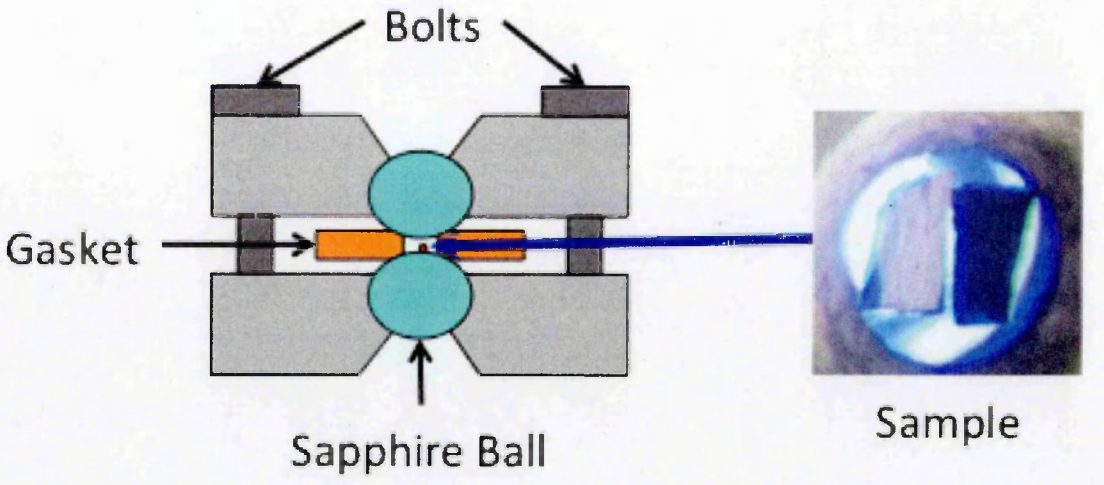

Figure 20: A diagram of the sapphire ball cell, and how the samples are usually mounted.

The cell design is shown in figure 20. The sample is mounted inside a rolled steel gasket between the two sapphires. Pressure is then created by tightening four threaded bolts spaced equidistant around the circumference of the cell. It can be seen immediately that some form of pressure medium is required to transfer pressure to the sample without requiring the sapphires to physically touch it. For this a solution of 1:1 methanol/ethanol is used [23]. This pressure medium also keeps the pressure applied to the sample hydrostatic.

To measure the pressure an additional light-emitting sample is included in the cell as shown in figure 20. Normally a ruby chip is used as its peak emission is very narrow and its pressure coefficient is well studied [24]. This allows the pressure inside the cell to be determined via first measuring the peak emission wavelength of the ruby chip ~684nm at room temperature.

3.5.1.2 IR pressure gauge

Ideally when performing an optical experiment such as PL, as much as possible of the optical apparatus should remain undisturbed between measurements. This ensures that the optical collection stays as constant as possible, allowing for comparison between results. It can be seen from the Triax 320 specifications that to measure a 4μm sample requires the use of grating 2, and a Ge long pass filter, neither of which will allow the measurement of a ruby chip since it emits at 694nm. To allow measurement of the ruby chip the grating and filter would both

have to be changed during the measurement taken and then apparatus replaced again to measure the mid-IR semiconductor sample. This situation is less than perfect and therefore a previously measured near-IR sample was chosen instead. The sample chosen was a piece of $In_{0.73}Ga_{0.27}As_{0.89}P_{0.11}$ quantum well sample with room temperature peak emission wavelength of 1.67μm, and a 10K peak emission of 1.44μm. The pressure coefficient had been previously measured to be 8meV/kbar for pressures up to 25kbar [25]. Using this sample as a pressure gauge will now allow grating number 2 of the Triax 320 to be used, but still requires a change of long pass filter. This however was the smallest optical change.

3.5.1.3 Unique Sample Mounting Technique

As stated earlier, the pressure gauge is normally mounted side by side with the semiconductor to be measured. However, in the Type II superlattice measurements reported in chapter 5 the emission from the semiconductor is thought to decrease with pressure. This leads to difficulty in the situation where changing the optical focus from sample onto the pressure gauge, adjusting and measuring the pressure, then adjusting the optical focus back. When trying to change the focus back onto the semiconductor being measured there is the possibility that the signal has decreased, or that the focus is not consistent with the last measurement. This process is also unavoidable, as the sapphire ball cell needs to be physically removed from the copper "L" bracket to have the pressure adjusted.

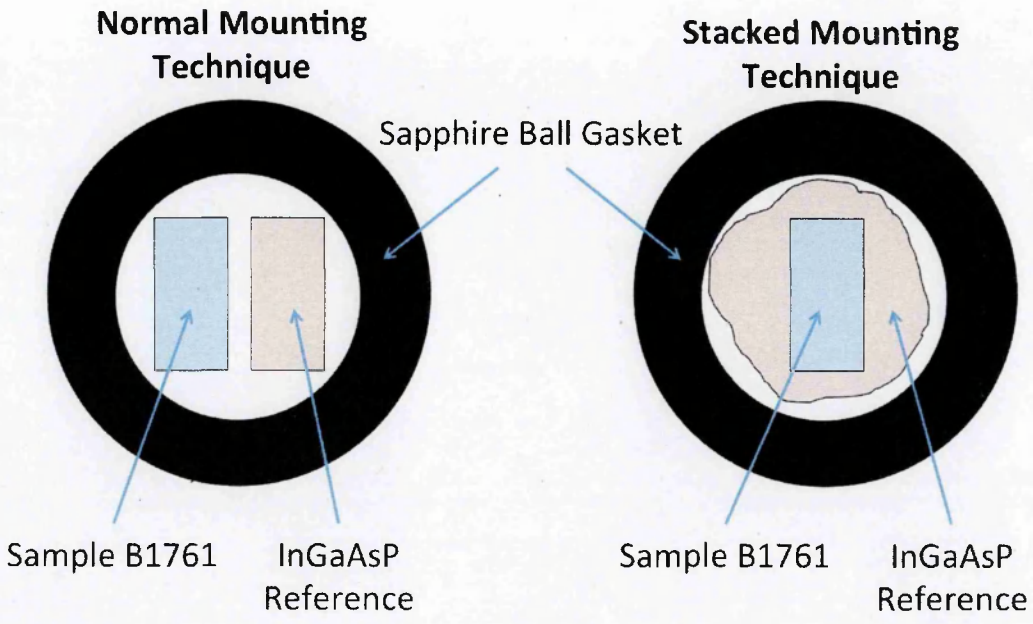

Figure 21: (Left) How the samples in a sapphire ball cell are normally loaded. (Right) The unique mounting method used for this experiment. This method allows for measurement of a decaying intensity signal with certainty, regardless of signal strength.

To counter this situation a unique "stacked" mounting technique was developed shown in figure 21. The sample and pressure gauge were both thinned, and a piece of the pressure gauge the approximate size and shape of the rolled steel gasket hole was cleaved. The sample was then mounted on top of the pressure gauge. The aim of this method is that is that the sample would create a positional drop in measured intensity of the pressure gauge. So when scanning across the gasket space there would be a "dark spot" in the gauge intensity where the sample is positioned on its surface. This would allow the sample to be found accurately and consistently every time, regardless of its output intensity.

The results of scanning across the gasket spacing is shown in figure 22. From this data, a central drop in intensity is observed, which leads to the conclusion that the excitation laser spot size within the sapphire ball cell is larger than the sample size, completely engulfing it. This allows for the sample to be found easily and consistently by focusing the optics on the pressure gauge. This can be done

because once the smallest amount of pressure is applied to the cell, the sample will be held in place by the pressure medium and no longer move, thus stopping it falling to one side of the gasket. The idea that the laser spot engulfs the entire sample does have a drawback however. This now means that an unknown amount of power from the laser is falling onto the sample, leaving it impossible to give absolute values in power dependent spectra. However, power dependent values presented are useful in determining trends, as the laser spot size and sample size are constant. It should also be noted that while the change in prism position is in mm, this is not the same quantity of movement inside the cell. As the light passes through the sapphire ball it is focused. This means that one mm of prism movement creates a smaller but proportional movement of the laser beam inside the cell.

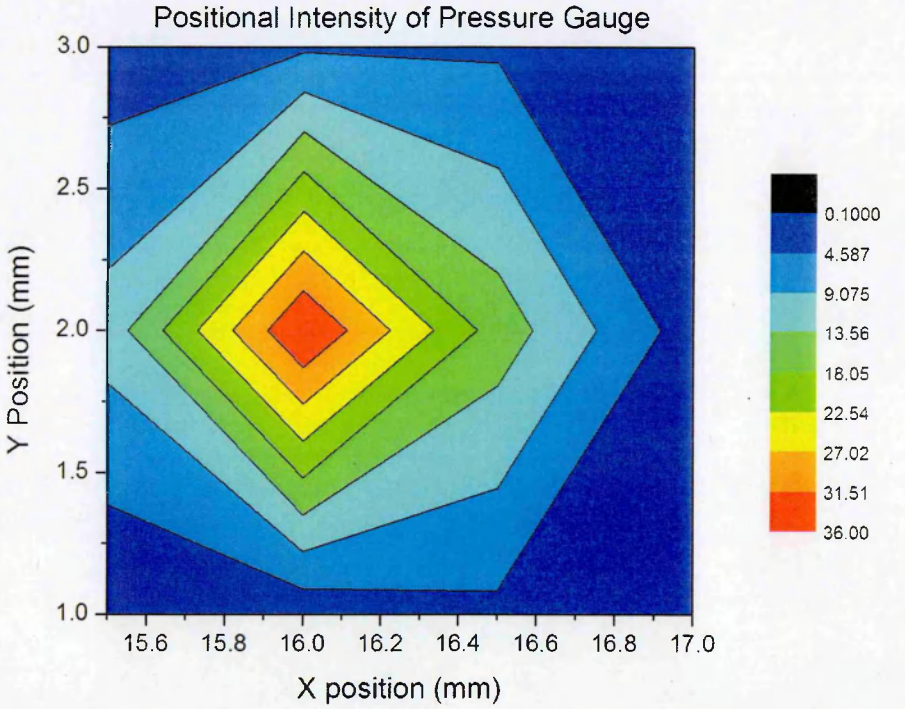

Figure 22: $In_{0.73}Ga_{0.27}As_{0.89}P_{0.11}$ output intensity as a function of laser spot position inside the sapphire ball cell.

3.5.1.4 High Pressure Experimental Setup

The adapted experimental setup to include the sapphire ball cell is shown in figure 23. The differences from the normal PL setup are as follows; only one CaF_2 lens is used between the cryostat and the spectrometer. This is because the

sapphire ball acts as a lens, therefore any light being emitted from the cell should already be collimated. The single CaF_2 lens is then used to focus this collimated light onto the spectrometer port.

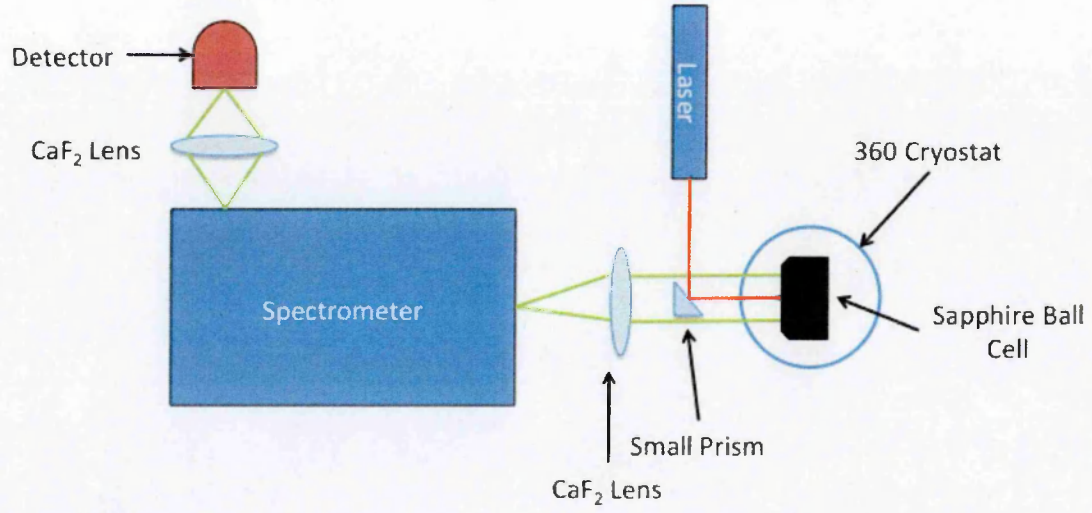

Figure 23: The experimental setup when performing high pressure PL experiments with the sapphire ball cell.

A small $1mm^2$ prism is used to direct the light into the cell at normal incidence. This is again because the sapphire ball acts as a lens, so introducing the laser beam into the cell at an angle which is not perpendicular to the sample will focus the laser spot away from the sample. This is illustrated in figure 24 and exaggerated to show the beam being able to miss the sample if the angle of incidence is high enough. This figure also shows that due to the mechanical nature of forcing the sapphire balls together to create pressure, the laser spot size inside the cell will have also have a small dependence on pressure. The sapphires are forced closer together making the distance between the ball and the sample decrease, at the maximum pressure achieved of ~21kbar the gasket has thinned by ~290μm. As the sapphire ball's focal distance is constant, the focus and therefore size of the spot will change. The calculated focal length from the edge of the sapphire ball is given by [26]:

$$F = \frac{(2 - N)R}{2(N - 1)}$$

Where N is the refractive index of the material i.e. 1.6753 for sapphire and R is the radius of the sphere in this case 6mm. Resulting in F = 1.44mm. However, this should make no significant impact on the results as the gasket thickness is 450μm, and the spot size is known to be larger than the sample from the

mounting technique. Since the sample size and therefore laser spot is many times larger than the gasket thickness this focal change is insignificant. Finally the largest source of error and difference from zero pressure PL measurements is the fact the sapphire ball cell must be removed from the optical setup to adjust the pressure.

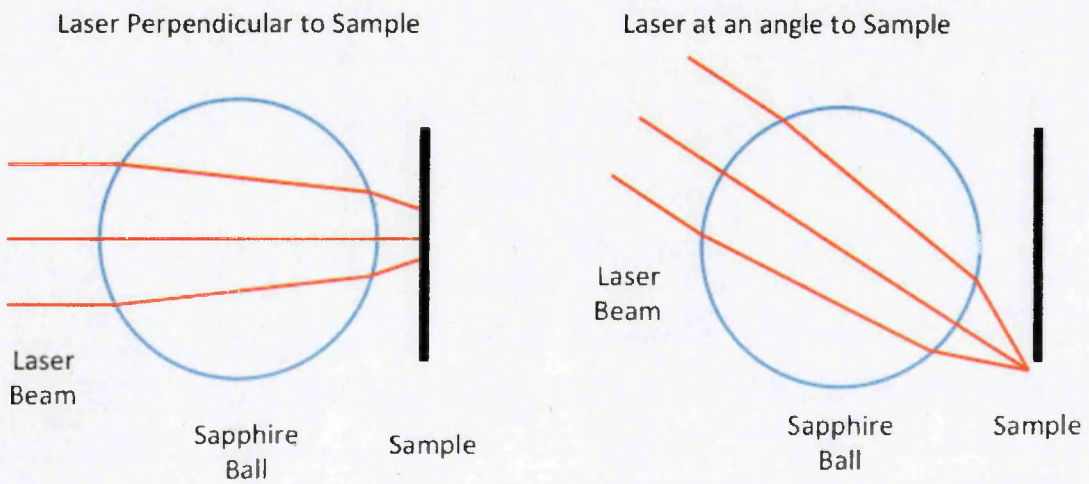

Figure 24: The importance of introducing the excitation laser perpendicular to the sample when focusing using a sphere.

The process to take pressure dependent measurements is shown in figure 25, it can be seen that there is significantly more time required to produce these measurements due to the temperature cycling of the cryostat and the need to measure the pressure gauge for every sample measurement taken. If the pressure is not being adjusted and temperature or power measurements are being performed then the process is that same as that of a normal PL experiment shown in figure 18. It should be noted that although the pressure can be measured at room temperature with the gauge used, it must be repeated at low temperature. This is because the pressure is held in the cell by threaded bolts which will expand and contract when heated and cooled. This usually results in some loss of pressure at 10K compared to room temperature.

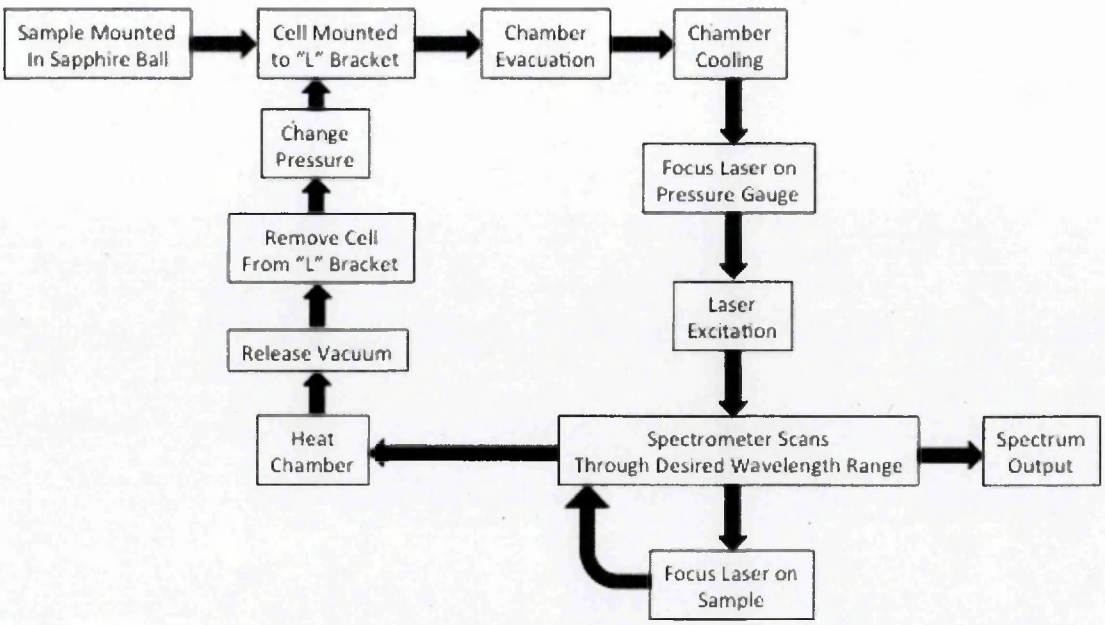

Figure 25: The process flow when performing pressure dependent PL measurements using the sapphire ball cell.

3.6 Absorption Spectroscopy

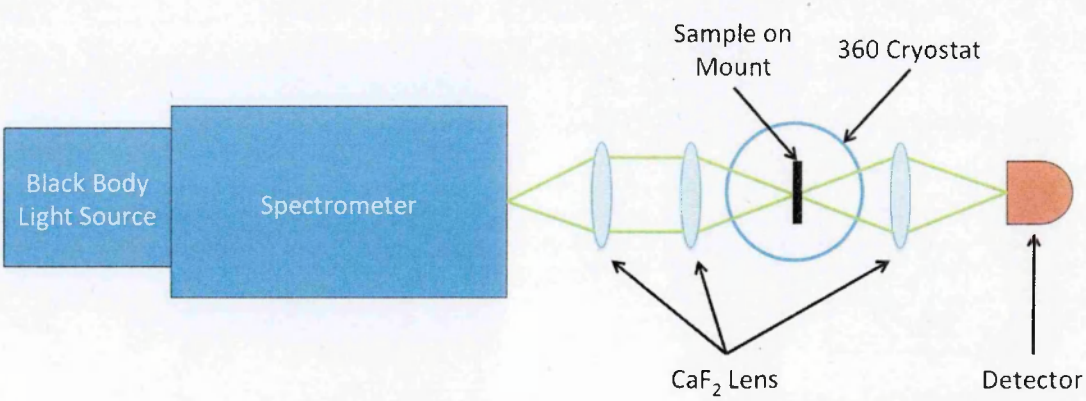

Figure 26: The experimental setup when performing absorption measuremnts.

Absorption spectroscopy shares much of the same experimental setup as PL, this is shown in figure 26. The sample is mounted on a copper "L" plate using silver dag, however in absorption spectroscopy a small hole is milled in the "L" bracket to allow light to pass through. For this mounting technique the sample must be of sufficient size to straddle the hole so that the silver dag can be applied above and below the hole, and no silver dag is left on the sample area covering the hole where it would interfere with the transmitted light. A broadband or black body

light source is then directed through the monochromator port using an internal focusing mirror. The spectrometer then outputs a monochromated light beam that is collimated by the first CaF_2 lens and focused onto the sample using the second CaF_2 lens, this is called the probe beam. The point of focus of this probe beam must be at the point where the hole is milled in the copper "L" bracket. This light is then transmitted through the sample, and collected by a third CaF_2 lens which collects the transmitted light and focuses it onto the detector element. It is worth noting the ease of using lenses for this technique when compared to parabolic mirrors, as each lens can be adjusted individually. The computer controlled spectrometer scans through the selected wavelength range in the desired step size producing a spectrum of the transmitted light. The process flow is shown in figure 27. The monochromated beam is also mechanically chopped in practice, this allows for the use of a lock-in amplifier to increase the signal to noise ratio of the measured signal in the same way as that of PL.

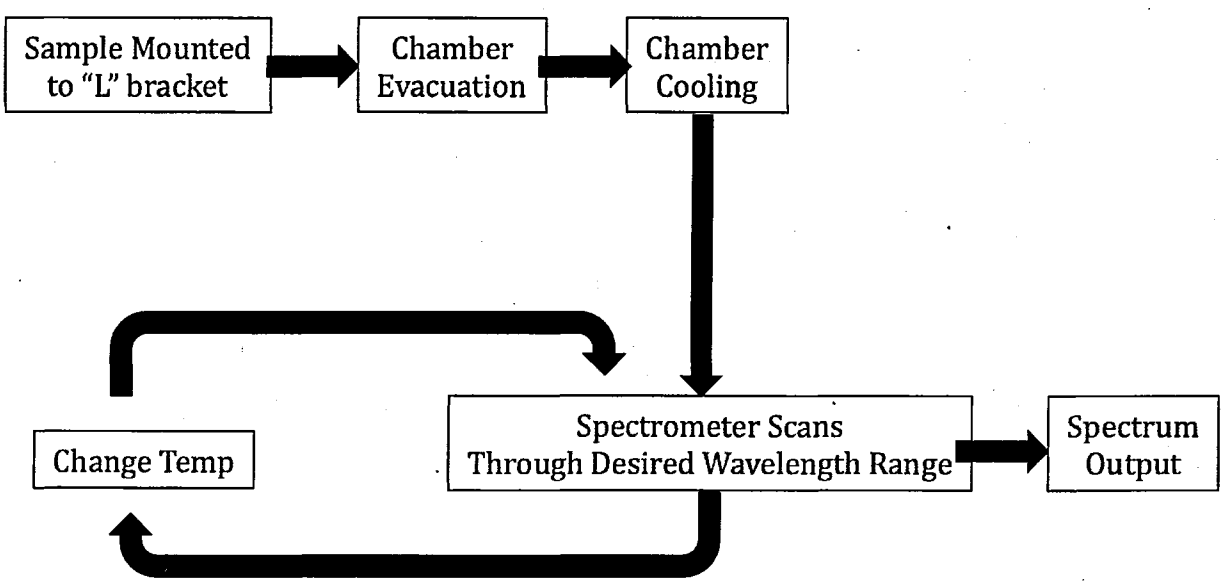

Figure 27: The process flow when performing absorption measurements.

3.7 Summary

All of the experimental techniques and apparatus in this work have had special consideration to their suitability for work in the mid-IR. All of the individual pieces of apparatus used have been selected for their good transmission in the

wavelength range of interest. Where no mid-IR alternative could be found, as is the case with the cryostat window, the impact upon the experimental results has been considered. All of the apparatus that has been considered during this chapter have wavelength dependent features, however, all of these features should be removed during the normalisation process.

3.8 References

[1] M. Merrick, PhD Thesis, University of Surrey (2006)

[2] Triax Series Imaging Spectrographs, Horiba Group , Accessed Jan 2013, <http://www.horiba.com/>

[3] E. Hecht, "*Optics fourth Edition*", Page 477, (2002)

[4] T. K. Sharma et al., "*A Method of Obtaining Simultaneous Complementary Spectroscopic Information on Self-Assembled Quantum Dots*", Japanese Journal of Applied Physics 48, (2009)

[5] J. Hodgkinson et al., *"Optical Gas Sensing: A Review"*, Measurement Science and Technology 24 (2013)

[6] U.S. Standard atmosphere, NASA, Acessed jan 2013, <http://modelweb.gsfc.nasa.gov/atmos/us_standard.html>

[7] L.S. Rothman et al., "*The HITRAN database: 1986 Edition*," Applied Optics 26, 4058-4097 (1987).

[8] C.E. Miller et al., "*Near Infrared Spectroscopy of Carbon Dioxide I.* $^{16}O^{12}C^{16}O$ *Line Positions,*" Journal of Molecular Spectroscopy 228, 329-354 (2004).

[9] Legacy Monochromators, Horiba Group , Accessed Jan 2013, <http://www.horiba.com/>

[10] Thorlabs 1300nm LP filter, Thorlabs, Accessed Jan 2013, <http://www.thorlabs.com/thorproduct.cfm?partnumber=FEL1300>

[11] Thorlabs Ge Windows, Thorlabs, Accessed Jan 2013, < http://www.thorlabs.co.uk/newgrouppage9.cfm?objectgroup_id=3980>

[12] Thorlabs 1100nm LP filter, Thorlabs, Accessed Jan 2013, <http://www.thorlabs.com/thorproduct.cfm?partnumber=FEL1100>

[13] Quartz or Glass?, LOT Oriel , Accessed Jan 2013, < http://www.lot-oriel.com/files/downloads/stroeher/en/quartzorglass.pdf>

[14] Calcium Fluoride (CaF_2) Windows, Edmund Optics Worldwide, Accessed Jan 2013, < http://www.edmundoptics.com/optics>

[15] Cryophysics, Accessed Jan 2013, < http://www.cryophysics.de/en/produkte.html>

[16] Cincinnati Electronics, Product no longer in production, <http://www.cinele.com>

[17] InSb Detectors, Infrared Associated, Accessed Jan 2013,

<http://irassociates.com/index.php?page=insb>

[18] Syntetic Sapphire, TYDEX Optics, Accessed Jan 2013,

< http://www.tydexoptics.com/pdf/Sapphire.pdf>

[19] Diode Laser, BWtech, Accessed Jan 2013,

<http://bwtek.com/technology/oem-laser-modules/>

[20] ND:YVO4 laser, Coherent, Accessed Jan 2013,

< http://www.coherent.com>

[21] W.B. Daniels et al., *"Simple sapphire ball cell for high pressure studies in the ultraviolet. In Recent Trends in High Pressure Research"*, pp. 809-11. Oxford & IBH Publishing Co (1991)

[22] M. Eremets, *"High Pressure Experimental Methods"*, Oxford University Press (1996)

[23] S. Casado et al., *"Direct Measurement of the Liquid 4:1 Methanol Ethanol Equation of State up to 5GPa"*, High Pressure Research 28: 4, 637-640(2008)

[24] H.K. Moa et al., *"Calibration of the Ruby Pressure Gauge to 800Kbar Under Quasi Hydrostatic Condictions"*, Journal of Geophysical Research 91, B5, 4673-4676 (1986)

[25] D. Patel et al., *"Optical Properties of Semiconductor Lasers with Hydrostatic Pressure"*, Journal of Applied Physics 74 (1), (1993)

[26] M. Riedl, *"Optical Design Fundamentals for Infrared Systems"*, Second Edition, (2001).

Chapter 4 - Quantum Dots

4.1 Introduction

Mid-IR lasers operating in the 2μm to 5μm wavelength region have many uses in fields including the military, biomedical, industry and trace gas sensing [1]. There is great difficulty covering this full wavelength range with simple structures such as direct bandgap quantum well structures. This is because they rely on interband energy transitions and therefore the bandgap largely determines the emission wavelength of the device. Figure 1 shows the bandgap of the main semiconductor materials, with the smallest bandgap being an alloy of InAs and InSb. While a wavelength of 6.2μm at room temperature is predicted for bulk InSb, making a useable hetero-junction structure requires confinement from a barrier material, and substrate on which to grow the structure, ideally one that can be easily integrated with existing electronic circuitry. A material suitable as a substrate would be GaSb, however this introduces a large strain in any potential device due to the large lattice mismatch, limiting both maximum emission wavelength and device performance due to strain related defects.

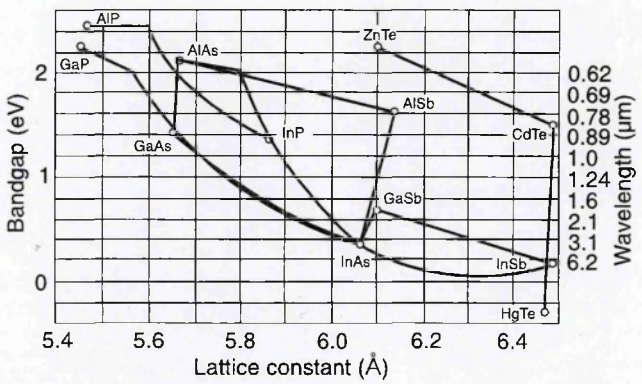

Figure 1: The lattice constant and bandgap of several common semiconductor materials. Adpated from [2]

As an alternative approach to the problem inter-subband quantum cascade lasers (QCLs) use only electrons (rather than electrons and holes) and emit at a wavelength inversely proportional to the spacing between conduction band energy levels. As this spacing is much smaller then the bandgap of the material very long wavelengths are achievable. However, to engineer smaller wavelengths the conduction band energy level spacing must be increased, making devices in the 2μ to 5μm region relatively difficult to achieve.

There is success in reaching the 2μm to 5μm wavelength range for both QW and QCL materials; however, success in reaching the desired wavelength often comes at the cost of another desirable parameter such as room temperature operation. Currently the longest emitting type-I quantum well device that could be found in the literature operating at room temperature is a GaSb based laser with an emission wavelength of 3.73μm [3]. However, as longer wavelengths are reached non-radiative recombination processes like Auger increase significantly. Type-II QW materials are predicted to have a lower Auger co-efficient than the direct gap devices. Once these type-II structures were grown this was found experimentally to be the case, C. L. Felix et al. [4] shows an example of such a Type-II QW where 4.2μm – 4.5μm emission is gained at 310K. QCL structures have achieved success in approaching this range N. Bandyopadhyay et al. [5] documents the room temperature operation of a QCL laser with an emission wavelength of 3μm, while wavelengths as low as 2.6μm have been reached with operating temperatures of 175K [6].

From the above it can be seen that by using a combination of type-II QW devices to cover the shorter wavelength region, and QCL devices to cover the larger wavelength range, complete coverage of the 2μm to 5μm wavelength region has already been achieved. Why then, is research being conducted to bring quantum dot devices into this wavelength region? This is because quantum dots offer potential advantages over the existing technology.

Quantum dot devices typically have a lower threshold current density and reduced temperature sensitivity than a QW or QCL due to their delta function like density of states. Once the dot growth parameters for a given material system have been achieved, then SK self assembled dot growth is both fast, and straight forward compared to the complex layered structure of the W quantum well and QCL structures. Dots are also more resilient to damage, since quantum dots are more immune to defect propagation than QW or bulk active regions.

These advantages have been realised in the telecoms industry where most IR quantum dot research has been conducted to develop lasers that emit at 1.3μm and 1.55μm. These wavelengths are of interest to the telecoms industry as there are loss minima for silica based optical fibres at these wavelengths [7]. Quantum dot devices emitting at 1.3μm manufactured from InGaAs/GaAs and InAs/InGaAs have been demonstrated, showing improved characteristics compared to QWs [8, 9, 10], 1.55μm devices manufactured from InAs/InP [11] are also the subject of investigation.

4.2 Quantum Dot Growth

Though it is possible to grow quantum dots using lithography techniques, the density of quantum dots is defined by the pattern and the space between dots is large, as are the dots themselves [12]. The ability to grow island like structures from a 2D wetting layer was proposed by Stranski and Krastanov [13], and is now the standard for growing dense arrays of quantum dots. A monolayer of the quantum dot material is deposited, and 3D quantum dots are formed as further monolayers are deposited via strain relaxation. The resulting islands are known as self-assembled SK quantum dots.

To illustrate the principle of why 3D islands form, a simple model of energy balance can be considered [14]. The energy of a coherently strained film on a substrate, is compared to the surface energy of a strain free island consisting of the same number of atoms as the film. This comparison shows that there is a point at which it becomes energetically favourable to form 3D islands instead of a film. If the islands are approximated as simple cubes with side length X, instead of releasing the strain energy the cubes have greater surface energy due to the increased surface area of the cube compared with the film. At some critical length X_c it becomes energetically favourable to form a 3D structure that has lower surface energy than the in-plane strain energy. So when $X > X_c$ [14]:

$$X_c \propto \frac{\gamma}{\varepsilon^2} \tag{1}$$

Where γ is the surface energy and ε is the in-plane strain. This means that when $\varepsilon \neq 0$ there is always a value of X above which islands will be formed. Although this model is simplistic it does illustrate some key points about quantum dot formation: (1) the size of the dot is related to the surface energy and hence shape of the dot. (2) The size is dependent on the in-plane strain created by the lattice mismatch of the dot and matrix material. This means introducing large atoms to a dot alloy will reduce the overall dot size.

To understand SK dot growth more fully, the problem will be analysed from a different perspective. The addition of a single atom to an in-plane strained material α is considered. The change in energy when the atom is added adiabatically and without change in volume is given by the chemical potential [15]:

$$\mu(n) - \mu_\infty \propto [\varphi_\alpha^\alpha - \varphi^\alpha(n)] + [\epsilon_d(n) + \epsilon_e(n)] \qquad (2)$$

Where n is an integer representing the monolayer number, μ_∞ is the chemical potential of the bulk material, φ_α^α is the binding energy of material α onto material α, $\varphi^\alpha(n)$ represents different binding energies depending on the monolayer number, for n=1 this represents the binding energy of material α onto material β, and for n>1 represents the binding energy of material α onto the underlying layers of material α. $\epsilon_d$is the dislocation energy caused by lattice mismatch, and ϵ_e is elastic strain energy per atom. Since quantum dot growth methods are epitaxial, the strain should be released elastically with no dislocations. This means the dislocation energy $\epsilon_d = 0$.

SK island formation occurs when $\varphi_\alpha^\alpha < \varphi_\beta^\alpha$ i.e. the binding energy of material α to β, is greater then the binding energy of α to itself. This results in $\mu(n)$ increasing as a function of n, resulting in layer by layer growth. At some critical value of n, $\mu(n)$ becomes a decreasing function and 3D islands are formed.

Although SK growth is the method of interest for this work, a similar analysis of equation 2 where the elastic strain energy ϵ_e is set to zero results in Frank-van der Merwe growth, where growth proceeds layer by layer with no island formation. If $\varphi_\alpha^\alpha > \varphi_\beta^\alpha$ then Volmer Weber growth is seen, where 3D islands are formed immediately with no wetting layer. The above techniques are graphically represented in figure 2, where a positive value to the chemical potential results in layer by layer growth, and a negative potential results in islands being formed as it is more energetically favourable. Figure 2 also shows that from this analysis of SK growth the wetting layer is self formed and will have a thickness of 3 monolayers, a significant width of the quantum dots themselves.

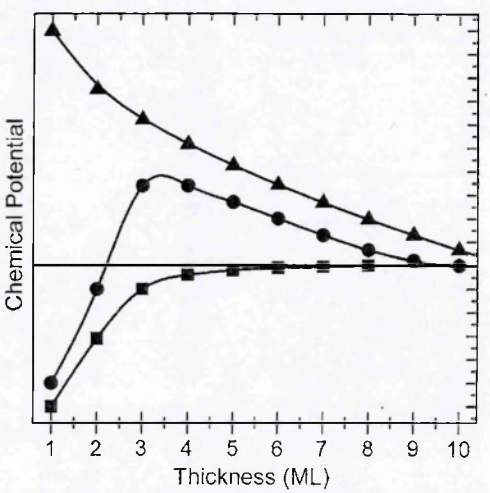

Figure 2: The change in chemical potential with monolayer thickness. Circles represent SK growth, triangles Volmer Weber, and squares Frank-van der Merwe. Adapted from [15].

4.3 Quantum Dot Bandgap Engineering

The above discussion on dot formation shows that strain is the largest determining factor in 3d island formation of SK quantum dots. In practice the dot emission wavelength is determined by dot morphology which is a function of the strain and alloy composition. For a fixed alloy composition dot width (as the height of real dots does not vary greatly) is the primary determining factor in the emission wavelength. We shall now look at practical dot examples, and show

how their properties relate back to strain, and the work being performed later in the chapter.

4.3.1 Quantum Dot Shape

The shape of the dot affects the emission wavelength by confinement of the dot wavefunction. While the overall effect on emission wavelength is small for similarly sized dots, the shape is determined by the plane upon which the dots are grown. This is illustrated by Lee et al. [16] who show a series of $In_{0.25}Ga_{0.75}As$ quantum dots grown on a substrate of GaAs. While not the material used in this work, figure 3 demonstrates that that the while the dot shape is based upon the growth plane, all of the dots show a similar truncated pyramidal structure and are of the same order of magnitude. The primary determining factor in the dot

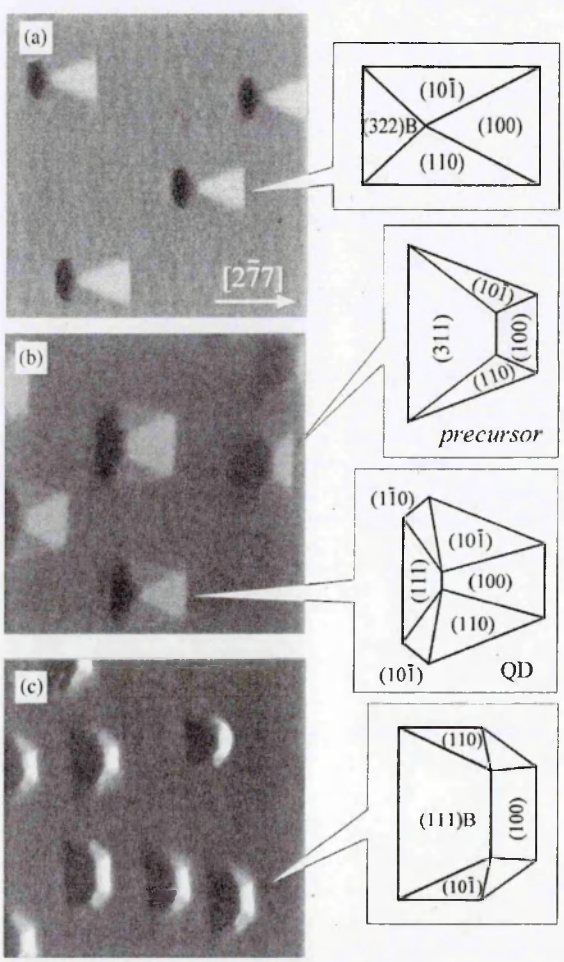

Figure 3: 500nm AFM images of quantum dots grown under the same conditions on the (a) (711)B plane, (b)(511)B plane, and (c) (211)B plane. Adapted from [16].

emission wavelength will be their width, and with them all sharing a similar width one would expect these dots to emit at very similar wavelengths. This means that when performing simulations later in this work that a square based truncated pyramid is acceptable as a simplified quantum dot modelling shape, and should give accurate simulations.

The dot shape is also affected by alloy composition. This is illustrated in figure 4, where two different InGaAs alloys are grown on GaAs, all growth conditions except alloy composition are kept the same. In this example the indium lattice mismatch generates strain proportional to the alloy fraction between the dots and matrix. Referring back to equation (1) it can be seen that a reduction in strain results in larger dots. Figure 4 (b) shows the same large well formed dots as figure 3, however with a larger indium fraction the dots are formed faster resulting in non-well formed hemispherical dots being formed as seen in figure 4 (a). It should also be noted that the density of the dots has also changed. The same quantity of material appears in each image, but the larger well-formed dots are less densely packed. This strain effect must be taken into account during the quantum dot modelling performed later. Although simulations will allow a truncated pyramid design to be used for any strain value, this is unphysical. In reality a very large strain between the dot substrate and dot alloy will cause the shape the dots to form quickly and not be of high aspect ratio i.e. they will form "blobs" rather than pyramids of defined height and width. This means that comparison between dot simulations of high and low strain are less meaningful as they cannot be grown in practise.

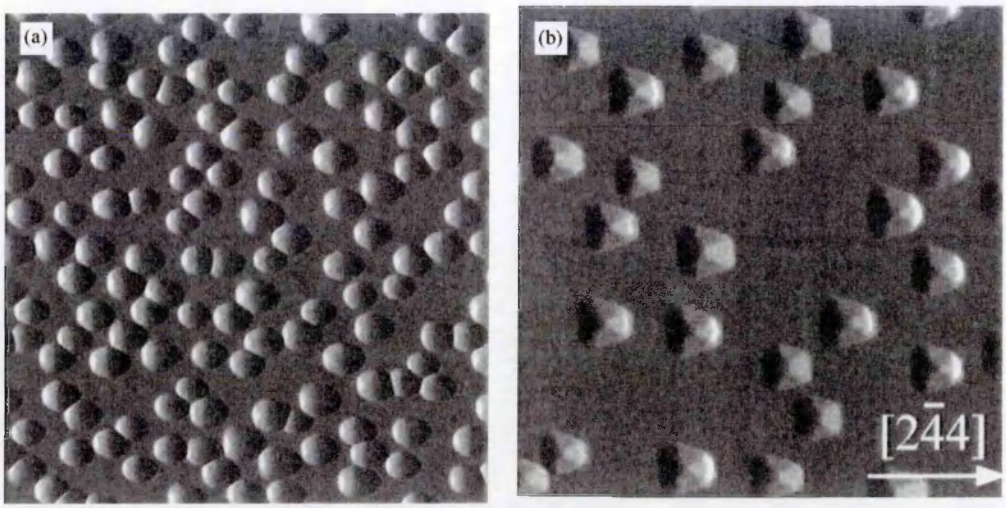

Figure 4: AFM images of the change in dot shape with composition, (a) $In_{0.5}Ga_{0.5}As$, (b) $In_{0.35}Ga_{0.65}As$. adapted from [16].

The growth temperature is also known to afect dot shape, Figure 5 shows $In_{0.25}Ga_{0.75}As$ on GaAs, grown at increasing temperatures, and finally annealed. Figure 3 shows the same alloy composition as a function of growth plane with well formed 3D structures. Use of a non-optimised growth temperature will cause the formation quantum dashes or small structures are formed instead. Therefore in this work, during both simulation and experimental ideal growth temperatures are assumed so that it can be assumed high aspect ratio dots are formed.

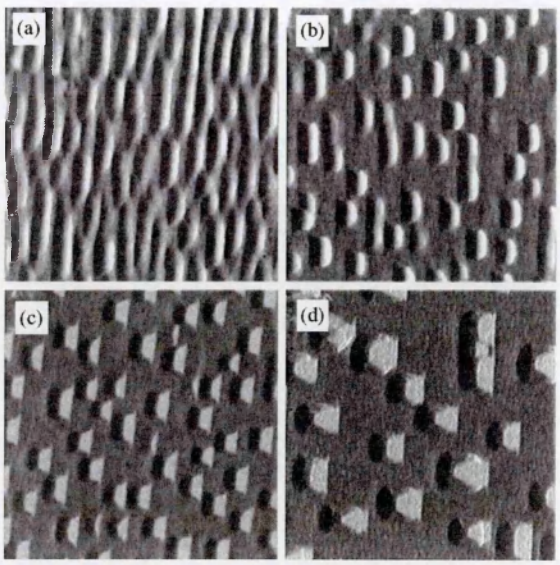

Figure 5: AFM images of $In_{0.25}Ga_{.75}As$ quantum dots grown at (a) 580°C, (b) 630°C, (c) 680°C, (d) the 580°C sample after annealing for 5mins at 680°C. Adapted form [16].

To further understand the effect growth parameters have on dot shape we look at a study by H. Saito et al. [17]. The first factor investigated in this study is the effect of growth temperature on InAs quantum dots in a matrix of GaAs. It is found by measuring the base diameter and height of the dots, that an increased growth temperature will result in larger volume quantum dots, as shown in figure 6. The "step" in this plot is thought to be caused by a transition from a low to high aspect ratio dot. The second part of this study investigates the spontaneous transition from high to low aspect dots by examining the RHEED

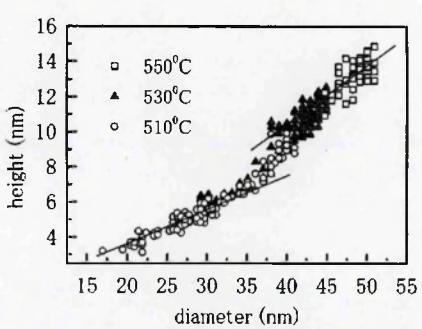

Figure 6: The mean diameter and growth heights of InAs/GaAs quantum dots grown at 510°, 530° and 550°. Adapted from [17].

patterns during growth.

The studies finding show that there is a critical dot volume at which it is energetically favourable to transition to a high aspect ratio shape as shown in figure 7. Given this new information, it can now be seen why in figure 5, as the temperature increases so does the dot volume, and at a critical volume the dots form the high aspect ration pyramidal structure.

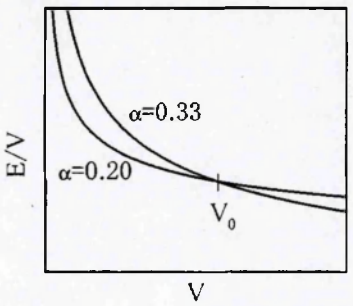

Figure 7: The energy dependence on volume for two facet angles (α) in radians. Adapted from [17].

4.3.2 Capping

It is normal practice to add a capping layer to a quantum dot semiconductor, this capping layer protects the quantum dot layer so that there is no damage from contact with the dot surface. Capping also allows for semiconductors with multiple quantum dot layers. This capping process itself changes the shape and therefore emission spectrum of the quantum dots. J. M. Garcia et al., [20] measured the size and emission spectrum of self assembled InAs quantum dots when capped with varying thicknesses of GaAs. It was found that increasing the capping layer thickness decreased the measured dimensions of the quantum dots and changed the emission spectra, as displayed in figure 7. Figure 7 shows (A), the substrate emission etched clean of quantum dots, (B) the dot sample capped with 50Å of GaAs, (C) the dots sample capped with 65Å of GaAs and (D), the 65Å capped sample emission after annealing. This again illustrates how annealing can alter the emission spectrum even for a capped sample, though to a lesser degree than an uncapped sample.

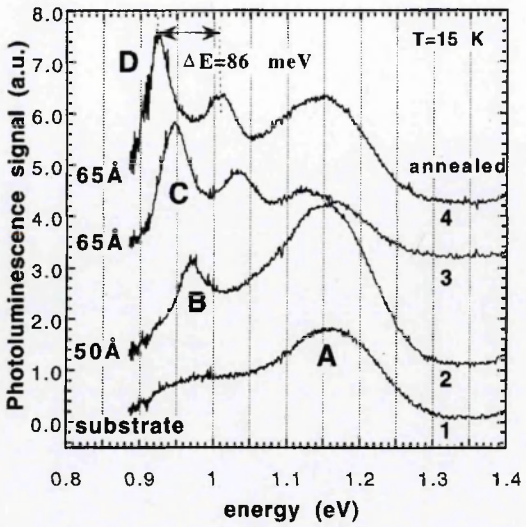

Figure 9: (A), the substrate emission etched clean of quantum dots, (B) the dot sample capped with 50Å of GaAs, (C) the dots sample capped with 65Å of GaAs and (D), the 65Å capped sample emission after annealing. Adapted from [20].

This change in dot emission implies a change in the dot shape by the addition of the capping layer. This leads to large problems when trying to measure the exact shape of quantum dots, for example the AFM images displayed in figures 1,2 and 3 were taken with an uncapped sample. The addition of a capping layer to these samples will influence any information on shape previously acquired. Furthermore the dot shape can no longer be measured fully as it is beneath the capping layer.

4.3.3 Barrier Imposed Strain

All of the above quantum dot studies are changing the growth parameters to affect the quantum dot emission peak, fundamentally each relies on strain. As the dot morphology relies so heavily on strain this can be used to engineer the dot bandgap. In a study by Z. Yin et al. [21], InAs quantum dots are grown in a matrix of InGaAs. Three samples were experimented upon with varying matrix alloys. The alloy of matrix (a) was $In_{0.53}Ga_{0.47}As$ lattice matched to the substrate, (b) was smoothly varied between $In_{0.53}Ga_{0.47}As$ and $In_{0.72}Ga_{0.28}As$, (c) was $In_{0.72}Ga_{0.28}As$ lattice matched to InAs. This leads to the situation where the InAs dots in (a)

should be under the most strain, (b) zero strain, and (c) zero strain. Under identical conditions same samples were also grown without the capping layer, enabling the use of AFM to measure the mean dot height and width, the results are as follows; (a) 9nm x 47.5nm, (b) 8.9nm x 54nm, and (c) 8.9 x 52nm. The high lattice mismatch between InGaAs and InAs in sample (a) has resulted in small dots to be formed. The low mismatch between InGaAs and InAs has caused larger but similar sized dots to be formed in samples (b) and (c).

The PL emission spectra measured at 12K are shown in figure 8, with the large dot sizes having a red shifted emission peak. It should be noted that the small change in emission wavelength and reduced PL intensity are attributed to a reduced carrier confinement due to the change in barrier shape [21]. While the previous dot engineering examples are secondary effects of strain, this study directly shows that strain can be used to engineer the bandgap of quantum dots, furthermore the dots consist of InAs as is the case in this work.

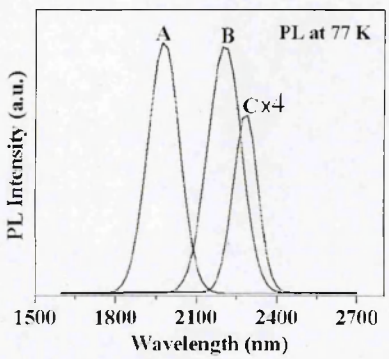

Figure 8: The emission spectra of InAs quantum dots when in a matrix (A) InP lattice matched, (B) graded to lattice match InP and InAs, (C) lattice matched to InAs. Adapted from [20].

4.3.4 Summary of Growth Issues

To summarize the above sections, strain strongly influences the dot growth behaviour outlined above, and therefore their emission wavelengths. This leads to interdependency between many of the dot growth parameters. The interdependency between parameters is one of the largest limiting factors

affecting new dot material systems, as there is an element of trial and error when growing real material systems from theoretical models.

4.4 Current Research

To extend the wavelength of quantum dot systems into the desired 2μm to 5μm wavelength range narrow bandgap materials such as In(As)Sb on GaSb substrates have been extensively investigated [22]. Fundamentally the bandgap range of a quantum dot material lies between the bulk bandgap of the barrier material used, and the bulk bandgap of the dot material. This makes the longest possible wavelength of InAs 2.97μm (0.417eV) [23] and InAsSb less than 5.27μm (0.235eV)[23] due to its large bowing parameter.

There has been some success in growing mid-IR dot materials using "standard" MOVPE techniques, a 2μm room temperature laser has been developed from InAsSb/InP [24]. Wavelengths of 2.46μm at 6K have been reached using InAs/InGaAsP/InP [25] quantum dots. To extend the wavelength limit even further, non-standard growth techniques are being investigated. When the large dots required for mid-IR wavelengths are grown they are not usually densely packed. To combat this alternate interruption growth (AIG) was used by T. Xiaohong et al. [26] to grow InAsSb/InP dots which emit at >2.8μm at room temperature which have 10x the density of standard growth SK dots. This growth technique involves cycling the flow of composition gas exposure, rather then exposing the substrate to all composite gasses simultaneously for a given time. A graded growth technique has been studied by W. Lei et al. [27], this involves changing the MOVPE growth conditions for each layer, this is shown to allow a larger antimony fraction into the InAsSb dot structure. While the results presented in this work are not the longest recorded dot emission wavelengths, they do show a promising method of potentially increasing the emission wavelength when used in conjunction with other work.

As can be seen from the work above, none of the current dot structures are reaching the maximum wavelength of the materials due to confinement within the dot. Work performed by O. Gustafsson et al. [28] have used this large confinement to produce weakly emitting quantum dots at wavelengths beyond 8μm at 77K. This is done by using a type III material, where there is overlap between the conduction and valence band. Due to the large confinement found in

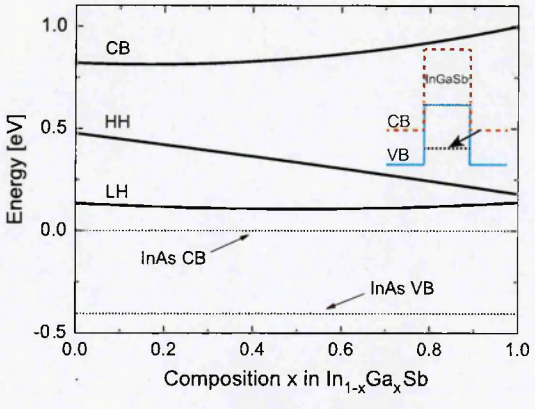

Figure 9: Type II transition found in the type III material. Adapted from [28]

the quantum dots, the energy transition is type II and very small as shown in figure 9. This type of quantum dot bandgap engineering is still in its infancy, with the PL signals measured being incredibly weak. However, it does show promise in creating very long wavelength quantum dots.

The dots systems studied in this work are investigated because they are direct bandgap, and are grown by MOVPE on InP substrates. This makes them cheap to grow because of the large size and low cost of the substrate, while being easily integrated into existing technology. Studying these dot structures also offers insight into future dot growth from understanding the underlying physics behind light emission. For example, the literature will often demonstrate working PL at a given temperature, but lacking discussion of the peak emission characteristics e.g. the number of transitions contained within the peak, or the dominant carrier recombination process within the sample. Understanding these underlying mechanisms can help make better devices. If non-radiative Auger recombination is found to dominate in a structure, engineering to supress this can lead to more efficient devices.

4.5 InAs Quantum Dot Samples

4.5.1 Introduction

The sample studied in this section consists of InAs quantum dots in a matrix of $In_{0.53}Ga_{0.47}As$ grown on an InP substrate. The dot structures are self assembled SK dots, grown using MOVPE. This structure was designed to be a mid-IR emitting sample with a target wavelength of ~2μm at room temperature that was relatively easy to grow compared to non quantum dot structures of the same wavelength. To achieve wavelengths of 2μm using quantum wells requires complex layer structures, and currently not attainable for intra-band QCLs, while this structure is simply strain InAs dots grown using the SK growth method. While this structure is not designed to have wavelengths longer than the samples mentioned in the previous section, it is used to gain an understanding of the underlying physics of a straightforward and commercially cheap growth technique.

The sample was grown by collaborative partners at Nanyang Technological University (NTU) in Singapore. A similar material composition from the same grower has been studied previously [29], and found to have a good PL emission at 10K with peak wavelength of 626.3meV (1979nm). The material being studied in this thesis has the addition of n-type doping to the substrate and p-type doping to the $In_{0.53}Ga_{0.47}As$ capping layer, this has been done to form a p-n junction diode for carrier injection.

4.5.2 Initial Photoluminescence Measurements

Photoluminescence measurements were performed using the apparatus outlined in chapter 3 and optically excited using a 450mW laser. The output spectrum at 10K is shown in figure 10, where is can be seen that there are two distinct peaks at energies of ~662meV, and ~788meV. Each of the peaks is fitted using a single Gaussian oscillator. This is considered a normal fit for SK grown quantum dots as they have a Gaussian size distribution. The equation used for the fit is:

$$I = I_{back} + Aexp\left(\frac{(E - E_c)^2}{2\Delta E^2}\right)$$

Where I_{back} is the Gaussian's background offset from zero, A is the Gaussian amplitude, E is the energy, E_c is the peak centre, and ΔE is the Gaussian width. The peak positioned at 788meV matches the band gap of $In_{0.53}Ga_{0.47}As$ [30] the matrix the dots are embedded in. The peak at 662meV is therefore attributed to emission from the InAs quantum dots.

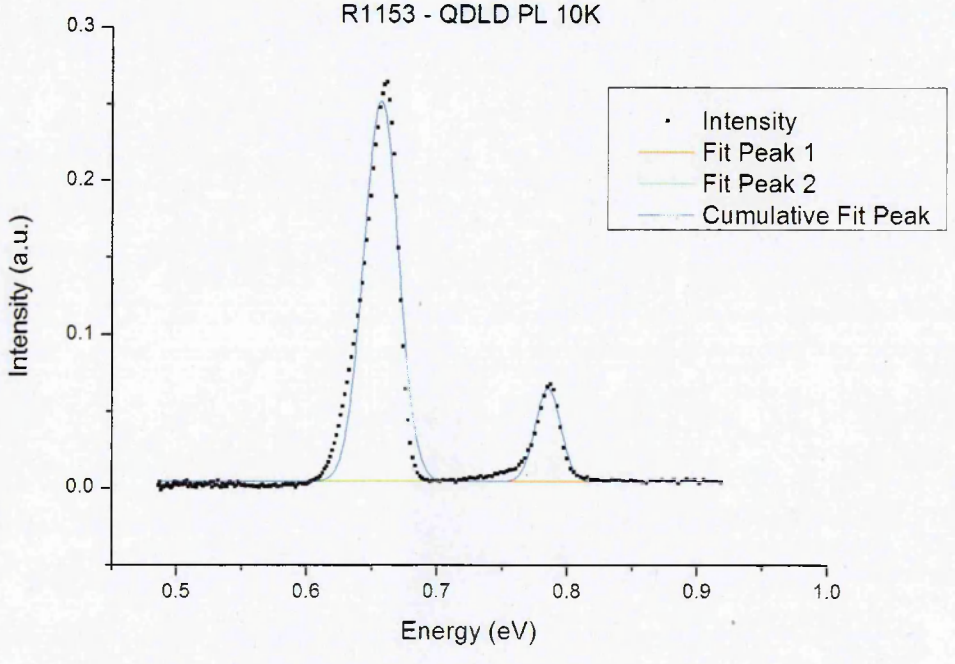

Figure 10: An example of the output spectrum from the InAs/InGaAs quantum dot sample, fitted using two Gaussian curves.

It can be seen from figure 10 that the InAs dot energy peak is not well represented by a single Gaussian peak, with discrepancies occurring at both the higher energy side and low energy side of the peak. This fitting discrepancy is displayed more obviously in figure 11, which shows a larger view of the InAs peak on a log scale. The red dashed line displays the fitted single Gaussian peak from figure 10. When viewed on a log scale a Gaussian centred around a point, has curves of equal gradient either side of the peak value. The "shoulder" indicated on the plot means that a single Gaussian does not sufficiently describe the curve and a second oscillator is required to achieve a reasonable fit.

Figure 11 also shows a two Gaussian fit, and the cumulative fit from these oscillators. The low energy shoulder feature is described by the blue curve, and the high energy peak is described by the green curve. This gives a closer fit to the experimental data. To compare the different fits statistically the coefficient of determination or adjusted R^2 value of the fit is used. The adjusted R^2 value gives a quantative value as to how well the curve fits the experimental data. The single Gaussian fit gives an adjusted $R^2 = 0.94224$, while the two Gaussian fit gives an adjusted $R^2 = 0.96483$. This means the visual fitting agrees with the statistical and the two Gaussian fit is used throughout the rest of this work. From the fitted curves the peak energies are found to be 646.4 ± 0.7meV and 662.0 ± 0.9meV, compared to the single Gaussian peak of 656.7 ± 0.3meV.

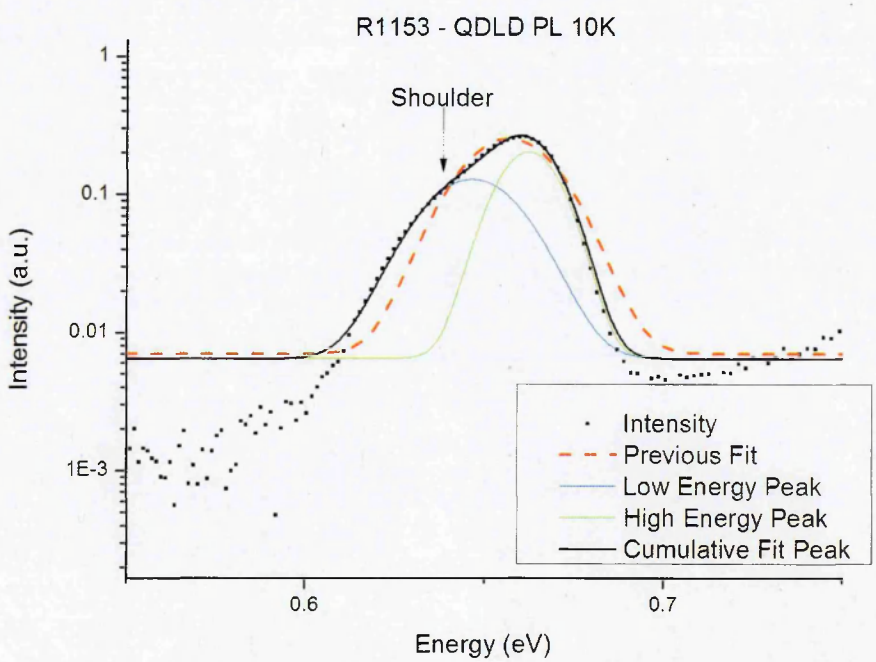

Figure 11: A larger view of the InAs dot peak from figure 10 on a log10 vertical axis. The low energy "shoulder" indicated on the plot shows that a second peak is required for fitting.

4.5.3 InAs Quantum Dot Modelling

To understand the physics behind the two oscillator fitting above, modelling of the quantum dot band structure was performed using Nextnano quantum device simulation software [31] (see appendix E for more information). To model the

structure a grid is defined in the growth direction, the barrier material then occupies all space where the quantum dot material is not found. The dot structure simulated is a common square base truncated pyramid design, the height and base width are definable parameters of the program with the side facet angle being fixed to correspond to the (011) plane, this structure is grown on a 0.5nm wetting layer of the same material as the pyramid. This does mean that for narrower pyramids the top facet becomes a decreasing sized square, until at a critical width the structure is no longer truncated and has a point like top, this is shown in more detail later.

After the grid and dot structure has been defined, a strain minimization calculation occurs, and the band structure and energy states are modelled using the effective mass model. Though the simulation can output any number of wavefunctions the first five eigenvalue are sufficient for this work.

4.5.3.1 InAs Quantum Dot Volume

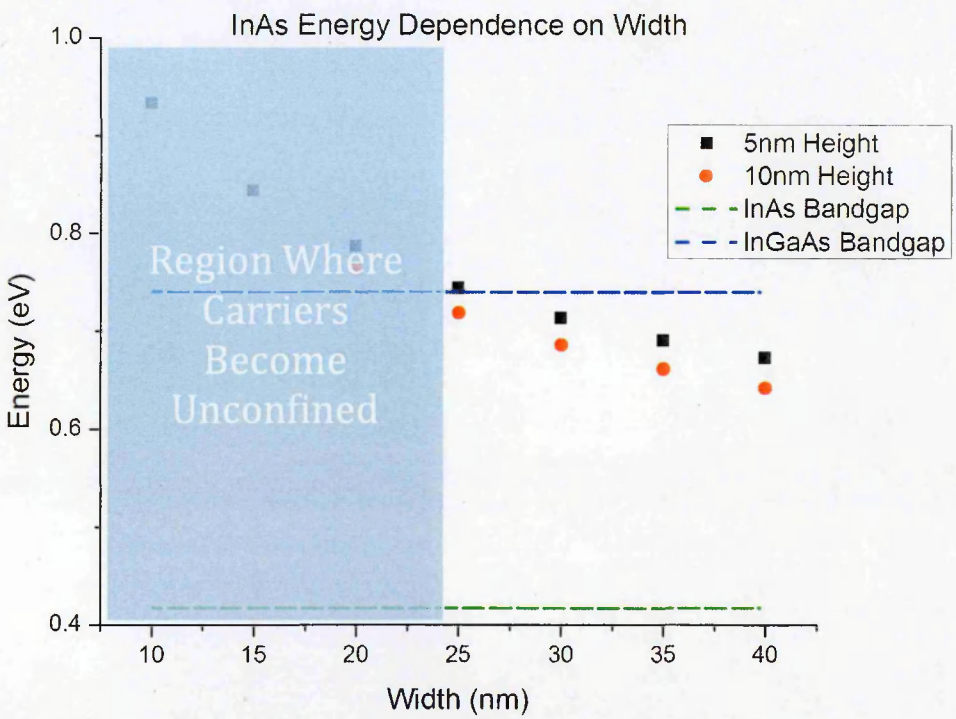

Figure 12: The calculated ground state transition for varying dot widths.

From the studies outlined above it was shown that dot morphology is the key factor in emission wavelength of quantum dot structures. As the dot shape is fixed in this simulation to a truncated pyramid, this eliminates all of the growth condition factors making the simulation for ideally formed dots. As the height of the dots is known not to vary greatly (between 5nm and 10nm in this simulation), this leaves dot width as the controlling factor in dot emission. The first stage of modelling the experimental data is to approximate the dot volume based upon the experimentally measured emission wavelength, a maximum and minimum dot height of 5nm and 10nm were chosen based upon previous studies [16, 17, 20]. The ground state energy transition for each dot width is shown in figure 12.

The data displayed in figure 12 shows firstly, that while the Nextnano software can calculate an energy state for all of the widths, some of the simulated data is unphysical as the dots have no confinement i.e. their ground state energy transition is above the bandgap of the InGaAs barrier. The ground state transition energy also tends to a value of 0.6eV with increasing width, the InAs bandgap minima is 0.417eV. This implies that even very large dot widths will have a maximum confinement of ~0.14eV i.e. the difference between the barrier and 0.6eV, note this is limited by the vertical confinement of the dot.

There is a constant gap of ~30meV between the 5nm and 10nm dot height energies at the same volume. This is to be expected as the energy levels of the system are dependent on the boundary conditions of the system. In this system the smallest boundary condition is the height and by increasing the dot height the system is given more freedom.

The two oscillators found in the experimental measurements can now be attributed to some underlying physics based upon the simulated model. Assuming that the lower energy peak is the ground state of the system, the higher energy peak can either be attributed to a higher energy level within the system or a second group of dots in the system. The system was simulated using

a dot height of 10nm and width of 38.5nm to give a conduction band to valence band energy transition of 647meV, these values are chosen to give a the simulation when performed at 10K and the experimental data when performed at 10K consistency. To ascertain if the higher energy oscillator fitted in the experimental data is a higher energy transition or a secondary set of dots, the first five conduction band and valence band transition energies for this dot size are shown in Table 1, it can be seen that there is no energy transition that is close to this value. To obtain an energy of 662meV by altering the dot size requires a height of 10nm and width of 35nm to gain a ground state transition of 661meV. Therefore based upon the higher energy transitions from the simulation it can be concluded that this sample has a bimodal dot distribution with average dot sizes of ~10nm x 38.5nm and 10nm x 35nm, a width change of 3.5nm between dot groups. It should also be noted that there is an energy degeneracy between the some of the HH states. It can be seen in figure 13 where the simulated probability densities are shown, that these states do share the same energy values, but not the same spatial orientation.

	Conduction Band $_1$	Conduction Band $_2$	Conduction Band $_3$	Conduction Band $_4$	Conduction Band $_5$
HH_1	0.647	0.678	0.682	0.711	0.730
HH_2	0.647	0.678	0.682	0.711	0.730
HH_3	0.649	0.680	0.684	0.713	0.732
HH_4	0.649	0.680	0.684	0.713	0.732
HH_5	0.652	0.683	0.686	0.715	0.734

Table 1: The first 5 conduction band to HH transition for a simulated dot size of 10nm x 38.5nm. All values shown are in eV.

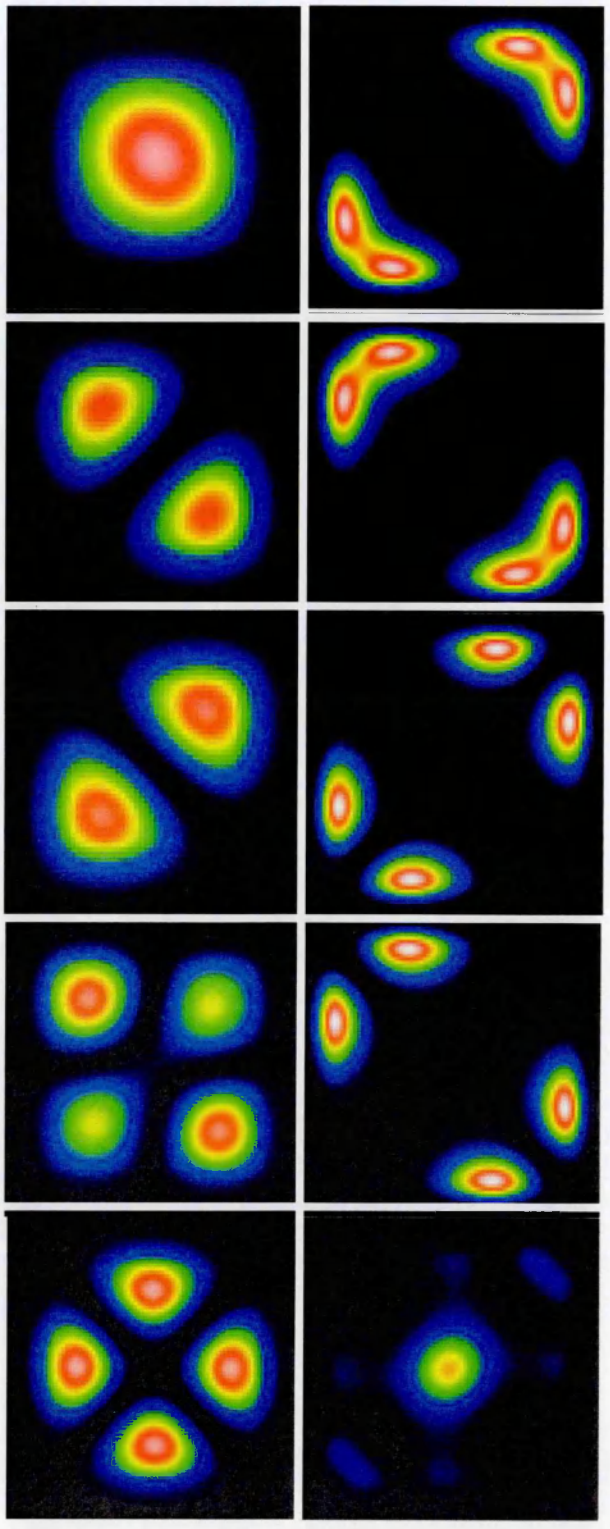

Figure 13: The first five simulated conduction band (left) and heavy hole (right) band wave functions for 10nm x 38.5nm InAs quantum dots.

4.5.3.2 InAs Quantum Dot Band Alignment

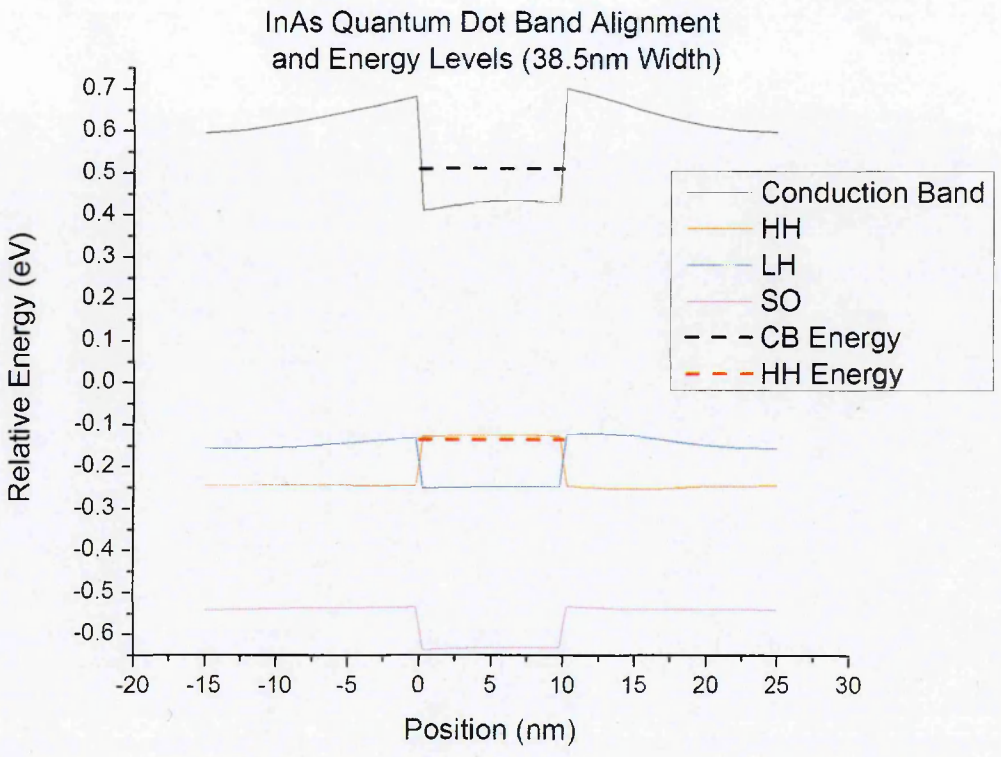

Figure 14: The simulated band alignment for 10nm x 38.5nm truncated pyramidal InAs quantum dots, where position indicates the growth direction.

Using the assumption of ideally formed, truncated pyramidal dots that have a corresponding wavelength to the experimental data, the size of the simulated quantum dots have now been established. From these values the simulated band alignment in the direction of growth is shown in figure 14 for the larger 10nm x 38.5nm dots, for the smaller 10nm x 35nm the profile is not shown as it is nearly identical. The small energy difference between the two dots is caused by the change in width as discussed earlier. A type I direct bandgap is observed with a large amount of confinement in both the conduction and valence bands.

4.5.4 InAs Temperature Dependent PL

The temperature dependence the InAs quantum dots were measured using photoluminescence apparatus as outlined in chapter 3, and the results of the experiment are shown on a $\log_{10}$ scale in figure 15. The figure shows that there are again two distinct peaks which were earlier attributed to the InAs dot emission and the InGaAs barrier emission. As the temperature is increased these

peaks begin to overlap, until the PL intensity has decreased to the point where the SNR is too low to detect any measureable signal. This point is reached at ~100K. The overlap of peak emission from the InAs dots and barrier means that at higher temperature the fitting is less reliable and this is reflected in the error bars. This overlap is primarily caused by the InGaAs barrier peak emission becoming less intense and broader with temperature, to the point that one Gaussian curve no longer fits the measured data. This thermal broadening of the InGaAs peak broadening effect has been documented previously [30].

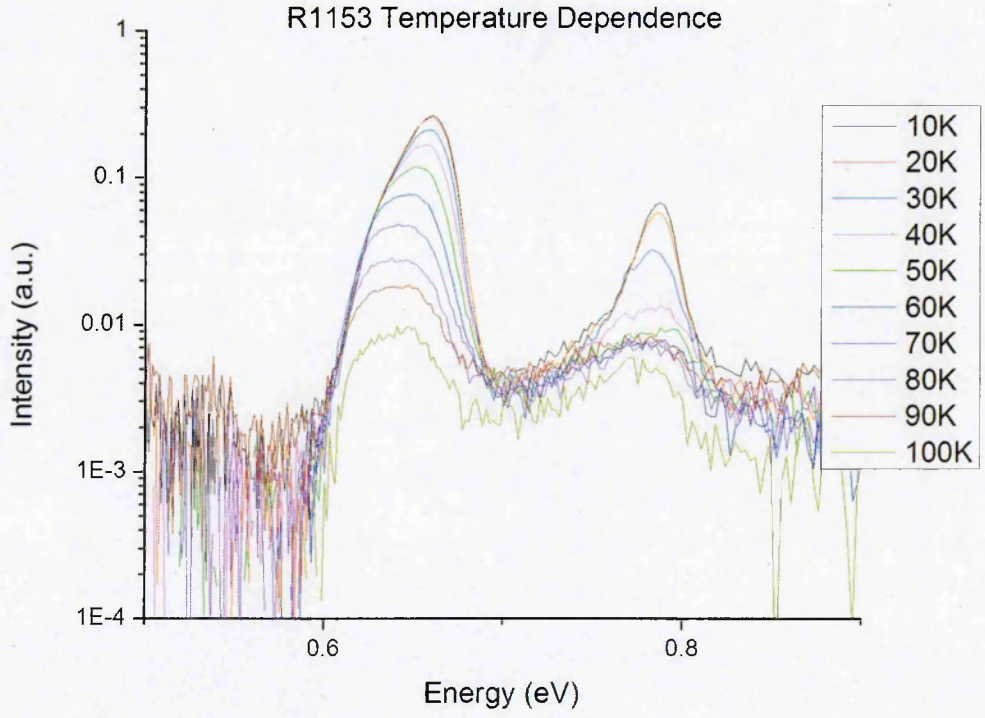

Figure 15: The temperature dependent spectra of the InAs dots, shown on a log vertical axis.

The shoulder feature that resulted in two Gaussian oscillators being fitted to the InAs dot peak earlier is even more apparent with temperature in figure 15. When this temperature dependent data was fitted using two oscillators the higher energy oscillator was found to decline in intensity, until it was no longer required to obtain a suitable fit, this decrease in intensity is shown in figure 16. The large error bars shown in the low temperature energy range show that although the oscillators have similar intensities there is ambiguity in the fit, their intensity relative to each other could be changed and still give an appropriate fit.

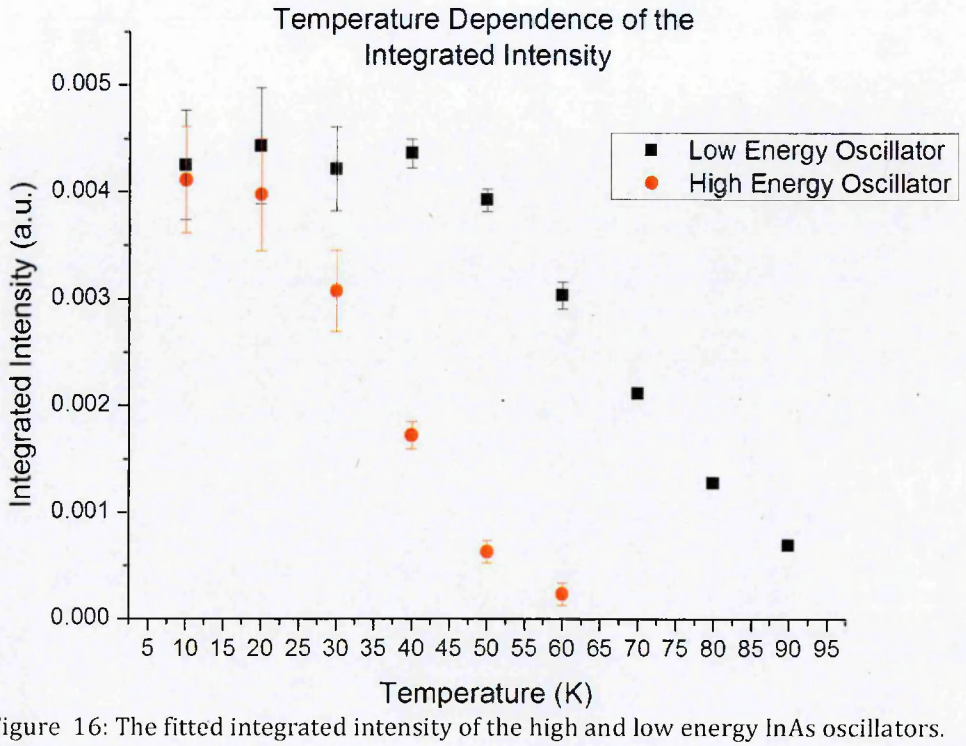

Figure 16: The fitted integrated intensity of the high and low energy InAs oscillators.

While these fits are appropriate normally the lower energy states of a semiconductor are filled first. This fit does show that the higher energy oscillator declines more rapidly with intensity than the low energy oscillator, with the low energy oscillator beginning to decline at a higher temperature. This can be explained by thermal redistribution of carriers between the two dot groups.

If there is a bimodal distribution of dots, then the shallower dots will have a larger band to band energy transition than the deeper dots. At low temperature the carriers are locked in place, as the temperature increases the carriers gain thermal energy and at a critical energy are no longer confined and can redistribute. This is shown schematically in figure 17. This redistribution will appear as a decline in intensity of the higher energy transition as the carriers redistribute to the lower energy dot states, with no change or an increase in the intensity of the lower energy dots as they receive more carriers. This process can be seen occurring in figure 16.

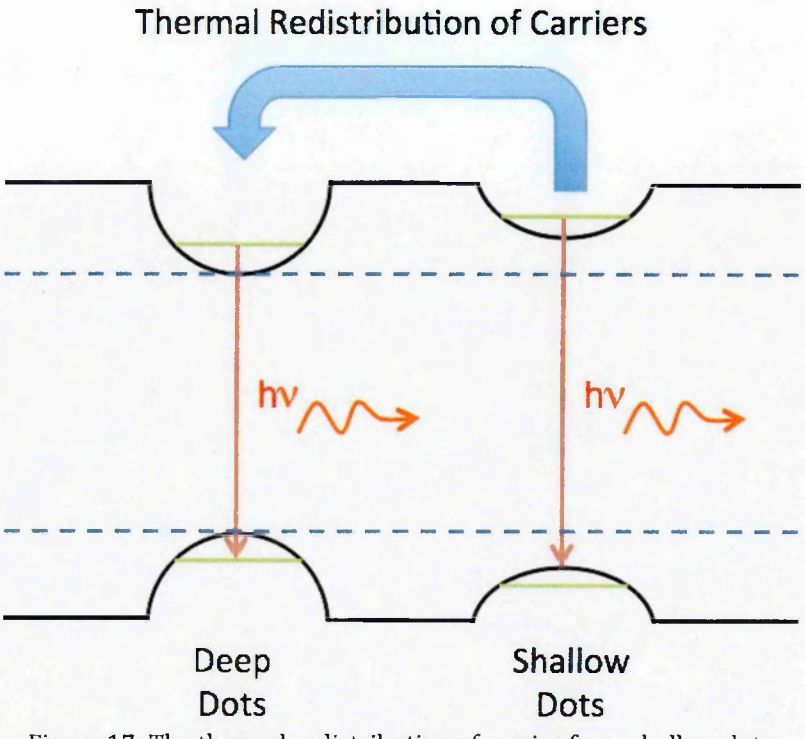

Figure 17: The thermal redistribution of carrier from shallow dots to deep.

Now that justification of a single Gaussian has been presented for the higher temperature measurements, the peak energy dependence of the sample is plotted in figure 18. The figure shows the measured peak energy temperature

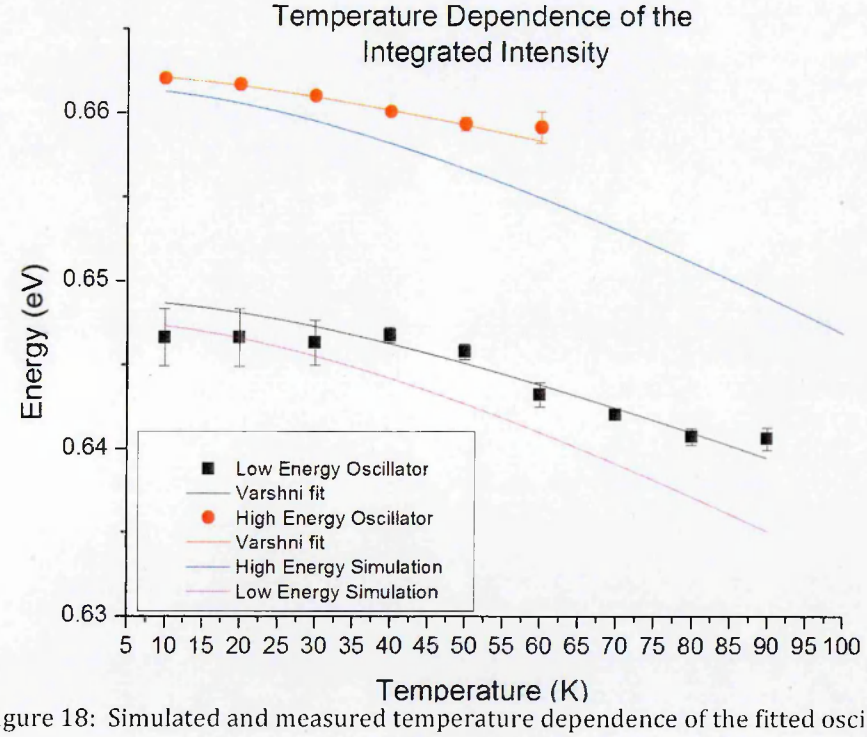

Figure 18: Simulated and measured temperature dependence of the fitted oscillators.

dependence for both high and low energy oscillators, and the simulated temperature dependence of each. The simulated data is modelled upon a Varshni temperature dependence, as the dots contain only InAs the simulated data follows the bulk value closely with only a small variation due to the strain contained in the dots. The high and low energy experimental data are also fitted using the Varshni equation in figure 18. The adjusted R^2 values for the experimental data are $R^2 = 0.904$ for the low energy curve and $R^2 = 0.979$ for the high energy curve. These R^2 values indicate that the curves are a good fit to the experimental data. Table 3 shows the Varshni parameters for Bulk InAs, the simulated data, and the experimental data. The table shows that there is a close agreement between the bulk InAs values for the Varshni parameters and the simulated data, as would be expected. However, there is a large difference between experimental values and the simulated. This indicates that though there is a reasonable fit as indicated by the adjusted R^2 values, the Varshni equation is not a good model to explain the experimental temperature dependence.

One possible explanation for the non-Varshni behaviour could be the thermal redistribution of carriers between the dot groups. The measured emission is always a combination of band and carrier behaviour, at low temperature the experimental data fits the modelled Varshni data well. As the temperature increases the fit becomes increasingly poor, but as the temperature increases more carriers are redistributed. This is something that the simulation would not be able to account for as it only models a single quantum dot rather than a bimodal pair as observed here.

	α (meV/K)	β (K)
Bulk InAs	0.276	93
High Energy Simulation	0.289±0.001	97.1±0.3
High Energy Experiment	0.123±0.071	51±58
Low Energy Simulation	0.286±0.001	95.4±0.4
Low Energy Experiment	0.200±0.21	81.7±19

Table 3: Simulated and experimentally fitted Varshni parameters

4.5.5 Power Dependent PL

The power dependent PL spectrum of the sample was measured to identify the dominant recombination process within the sample. This is important in the development of semiconductors as it gives and indication to device performance. Ideally all of the power input to the sample would recombine radiatively, making for an very efficient device. If it is found at this early stage of development that a defect or Auger related recombination process was dominant, modifications to the design can be made to try an minimize the carriers lost to these non-radiative processes. Furthermore, if the dominant recombination process is found to change as a function of temperature, this would indicate a decrease in efficiency with temperature.

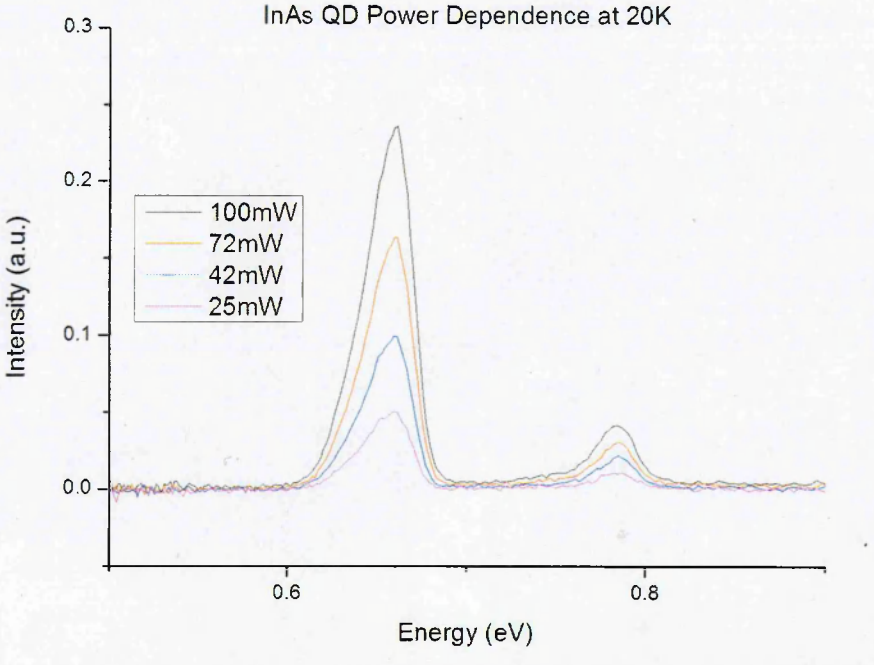

Figure 19: The measured power dependence of the InAs/InGaAs quantum dots sample.

Figure 19 shows the observed change in emission intensity with decreasing pump power, and shows that the peak attributed earlier to the InGaAs barrier emission begins to overlap with the InAs dot emission at low power. This is the same effect as seen earlier in the high temperature. The similarities between these effects indicate that the overlap of these peaks is always present but not

observable due to the very large SNR when at low temperature or high pump power, and becomes apparent once there is a sufficiently poor SNR.

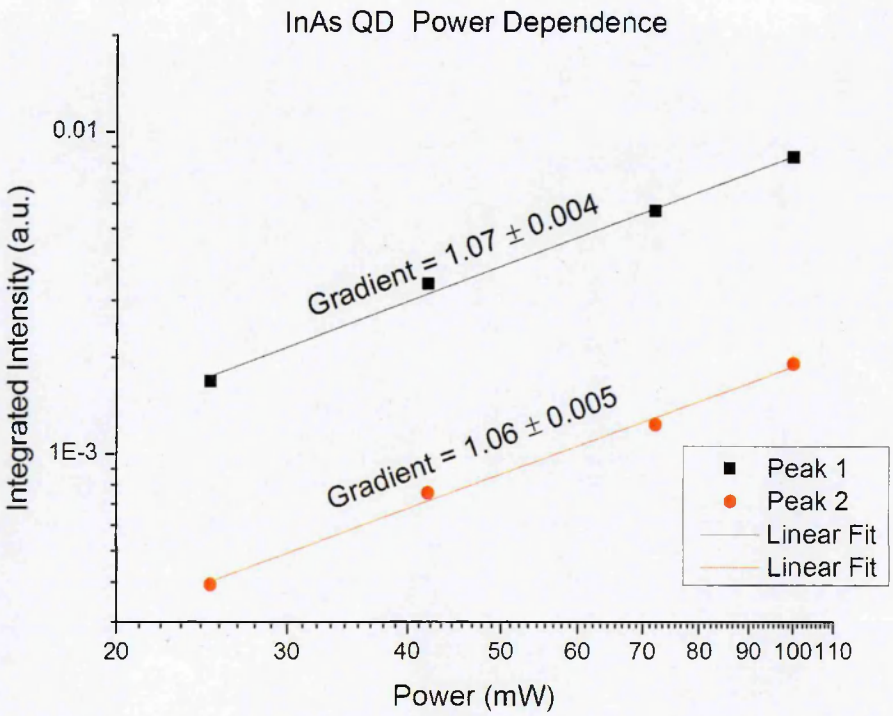

Figure 20: The integrated intensity of the InAs peak as a function of power.

Figure 20 shows the integrated intensity of the peaks as a function of power. The gradient of this curve is 1.07 ± 0.04 and 1.06 ± 0.05 for the InAs and InGaAs peaks respectively. These values indicate a dominant radiative recombination in both peaks at 10K. When measured again at 60K the power dependent gradient for the InAs dot peak is found to be 1.15 ± 0.07 showing again a dominant radiative recombination process. The measured gradient values of the curves are within error tolerances of each other implying that there is no significant change in the dominant recombination process of the InAs quantum dots over this temperature range.

4.5.6 Conclusions

A short review of how quantum dot morphology affects the emission wavelength has been carried out, and strain to found to be the underlying cause of dot

morphology. From the review realistic estimates for the size and shape of InAs quantum dots have been established for simulation using the Nextnano software package.

Using a truncated pyramid design with a height of 5/10nm InAs quantum dots have been simulated, and dot width shown to be the principle factor in determining the simulations output wavelength.

Experimental data determined that two Gaussian oscillators gave the best fit to the experimental data, from this experimental data and the simulation determined that these two oscillators were the result of bi-modal quantum dots with sizes of 10nm x 35nm and 10nm x 38.5nm as these gave a match to the experimentally observed oscillator peak energies.

The temperature dependence of the experimental data was found to vary from the simulated data based upon the Varshni equation. While the Varshni equation did fit the data with a high adjusted R^2 value the material constants were found to be very different from both the literature values and simulated value. This could be the result of thermal redistribution of carriers between bi-modal dots evidence for which was presented for in section 4.2.4.

Finally, the dominant recombination process in the sample was identified using power dependent PL. The dominant process was found to be strongly radiative at temperatures ranging from 10K to 60K. This indicates that the sample would have good device efficiency when pumped electrically.

4.6 Quantum Dot Sample R1433

4.6.1 Introduction

Sample R1433 is a quantum dot semiconductor grown by collaborators at NTU in Singapore. The sample has InAsSb quantum dots in a matrix of $In_{0.47}Ga_{0.53}As$, grown on an InP substrate. This material was designed as a mid-IR emitter with a target wavelength of ~2μm, and follows on from the previous InAs quantum dot sample by trying to increase the emission wavelength through the addition of antimony to the dot alloy composition. If previous dot dimensions can be maintained the addition of antimony should extend the emission wavelength further into the mid-IR due to the smaller material band gap.

There is one large drawback to the growth of SK self assembled InAsSb quantum dots, and this is exact knowledge of the antimony fraction within them. As there is no real control over the dot formation during the SK growth then the number of antimony atoms incorporated into each dot is unknown. On top of this the antimony is introduced to the MOVPE growth chamber in the form of TMSb gas, so only the flow rate of the gas, or the exposure time can be altered to change the antimony content. The two methods of antimony exposure are discussed below.

4.6.1.1 Antimonidation

Antimonidation is the process of opening the TMSb valve for a set time after the AsH_3 valve has been closed allowing for the Sb-As atoms to exchange. The results of such a growth method are shown in figure 21. The figure shows that with an increasing exposure time the peak emission wavelength is shifted to lower wavelength. It also shows that the main change in wavelength happens quickly with the largest difference being between 1 and 5 seconds.

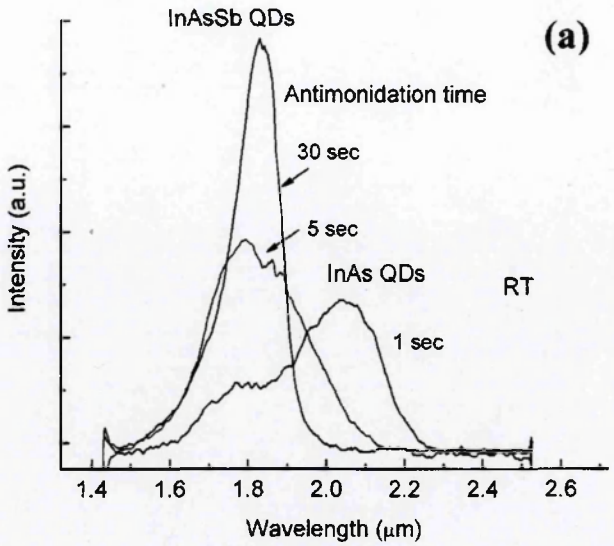

Figure 21: The change in measured spectrum as a result of increasing antimonidation times. Adapted from [32].

4.6.1.2 Alternating Supply Growth

Alternating supply growth is the process of having the TMSb valve and the AsH_3 valve open at the same time and instead changing the TbSb flow rate as a means of adjusting the antimony content. The results of this growth method are shown in figure 22. This figure again shows that increasing the flow rate the peak emission is shifted to lower wavelength.

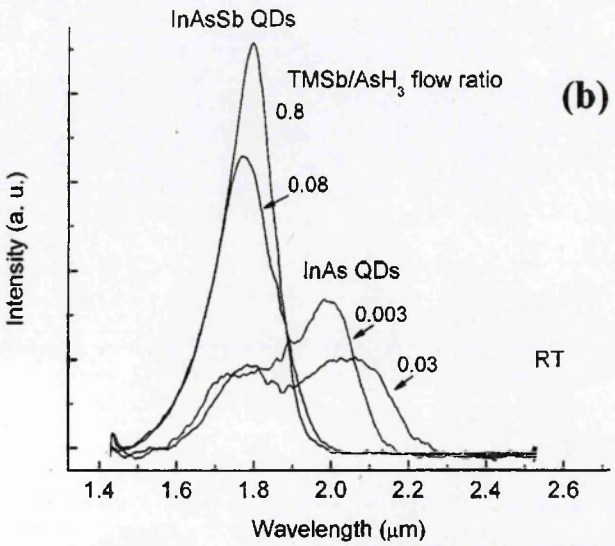

Figure 22: The change in measured spectrum as a result of increased flow rate during alternating supply growth. Adapted from [32].

Both of these growth methods display a blue shift when presented in this reference [32]. While this may first seem surprising as InSb has a lower band gap than InAs, as discussed earlier the morphology plays a large role in determining the output wavelength. In this case the antimony containing dots are much smaller, resulting in the blue shifted wavelength.

As was stated earlier, the amount of antimony in a given sample cannot be known exactly, and in principle the addition of antimony should increase the emission wavelength of the dot sample. However, for identical growth conditions the dot size is shown to decrease with the addition of antimony. This means that the growth conditions for the following InAsSb dots discussed in this chapter were not grown under identical conditions, and instead grown to make them as large as possible.

4.6.2 InAsSb Initial Photoluminescence

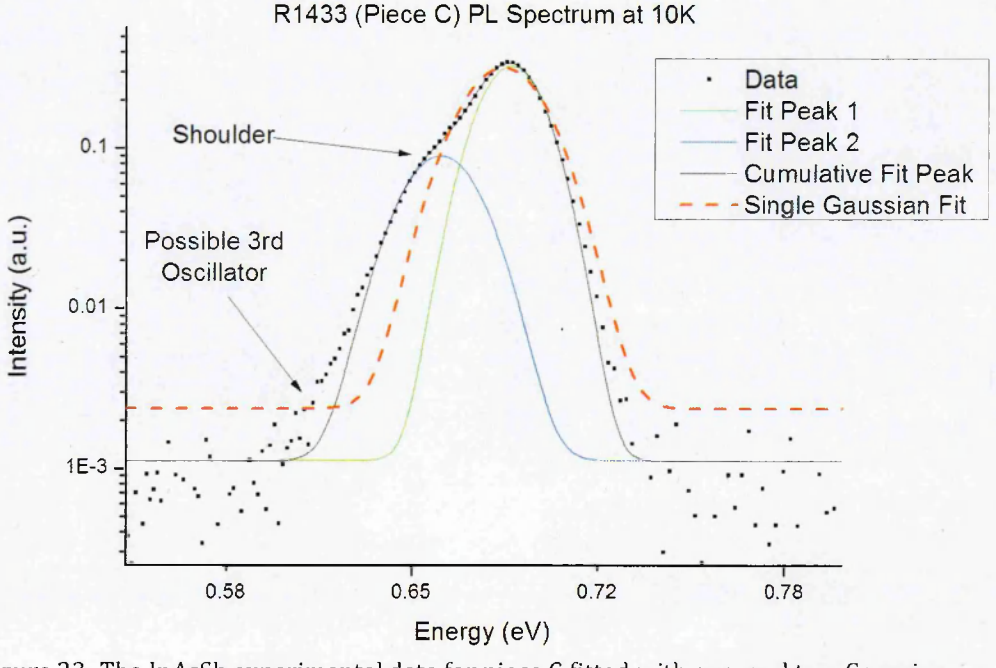

Figure 23: The InAsSb experimental data for piece C fitted with one, and two Gaussian oscillators.

Photoluminescence measurements were performed using the apparatus outlined in chapter 3, with the same 450mW laser used in the InAs quantum dot study. There were four separate pieces of sample R1433 provided and are labelled A-D,

each of them was measured using the same experimental techniques but displayed different properties. Figure 23 shows a typical PL spectrum obtained for samples C and D when measured at 10K. A Gaussian oscillator is used to fit the data with the equation:

$$I = I_{back} + Aexp\left(\frac{(E - E_c)^2}{2\Delta E^2}\right)$$

Where I_{back} is the Gaussian's background offset from zero, A is the Gaussian amplitude, E is the energy, E_c is the peak centre, and ΔE is the Gaussian width. It can be seen that a single Gaussian oscillator again does not adequately describe the curve. Instead, the "shoulder" feature indicates a second oscillator is required, and two Gaussian oscillators are used to improve the fit. There is possibly a third oscillator that could be centred at the low energy end of the curve to further improve the fit. However, when the reduced R^2 values are examined to determine how well the curves fit the experimental data it is seen that a single oscillator gives a reduced R^2 = 0.97539, and the two oscillator fit gives a reduced R^2 = 0.99909. A third oscillator was not used as the two oscillator fit is sufficient to accurately describe the data, furthermore there is no physical justification behind the addition of a third oscillator.

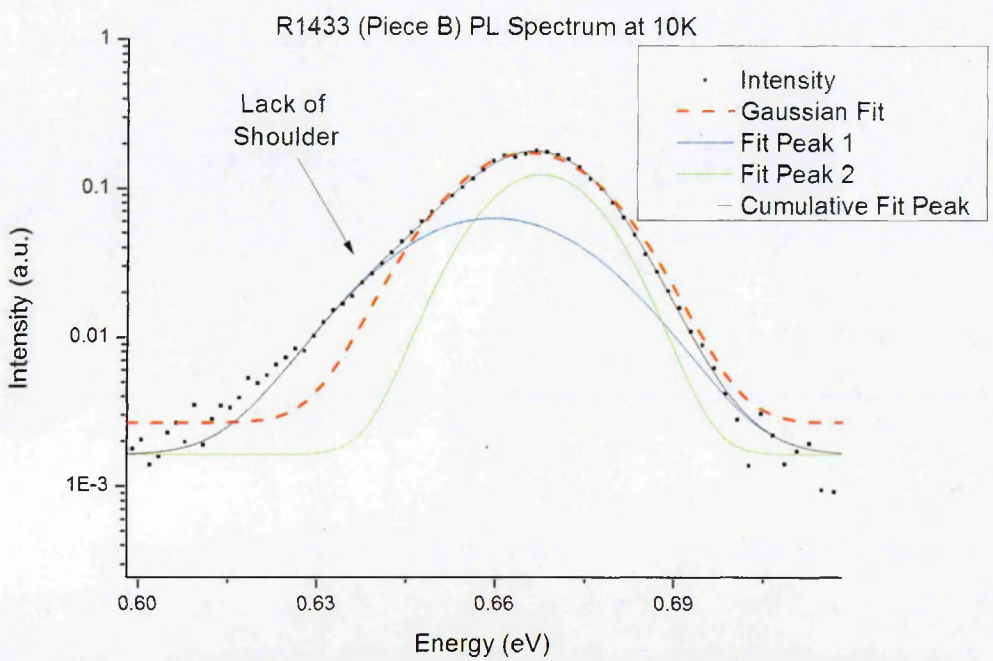

Figure 24: The InAsSb experimental data for piece B fitted with one, and two Gaussian oscillators.

A typical spectrum from the second group of samples A and B is shown in figure 24. In the figure fitting for a single Gaussian and two Gaussian oscillators are shown. As indicated on the plot there is no apparent low energy shoulder feature visible to indicate a second peak is required and the high energy side of the single Gaussian fits well. There is however a difference in fit between the experimental data and low energy side of the Gaussian curve. This poor low energy side fitting led to the fitting of two Gaussian oscillators which visually fits the data more accurately but with far more ambiguity in the peak positions.

To determine the best fit to proceed with the reduced R^2 values are again examined. The single Gaussian oscillator gives a reduced $R^2 = 0.99219$, and the two Gaussian fit gives a reduced $R^2 = 0.99893$. While two oscillator fitting does have the higher fitting accurately, the single oscillator fit was chosen for all future fitting. This is because there is a lot of ambiguity in the two oscillator fit as shown by the error when measured at 10K which would only resulting in an increase of the third significant figure of the reduced R^2 value.

The chosen fitting parameters give values for the peak energies as follows: samples C and D; 684.7 ± 0.1meV and 660.1 ± 0.7meV, and for sample A and B; 665.3 ± 0.1meV. From these initial peak positions it seems that the low energy oscillator from piece C and D, may correspond to the single fitted peak of samples A and B.

4.6.3 InAsSb Dot Modelling

To try and understand the physics behind the fitted oscillators from the previous section the InAsSb dots will now be modelled using Nextnano quantum device simulation software [31]. The simulation paramters are identical to that of the InAs simulation with the exception of InAsSb quantum dots being used.

While modelling the InAs quantum dots the only parameter required to change was the dot width until the output emission wavelength matched the experimental emission wavelength. With the inclusion of antimony this problem

becomes more complex as the antimony content will also adjust the emission wavelength. To estimate these values we shall consider the width first. When antimony atoms are added to the InAs structure the larger lattice constant increases the strain on the system causing the SK dots to nucleate more quickly, this means that the InAsSb dots cannot be larger then the previously measured InAs quantum dots imposing an upper width limit of 35nm. From equation (1) we can see that the point at which dots are formed is proportional to the surface energy divided by strain squared. Assuming that the surface energy is constant as the modelled dots are all truncated pyramids and the strain increase is directly proportional to the lattice constant mismatch, then the volume becomes proportional to the change in lattice constant squared. The lattice constant for InAs is 0.60583nm[23] and for InSb is 0.64794nm [23]. This gives a percentage change of 13.3%, from the above assumptions we can then assume a width change of ~13%.

4.6.3.1 InAsSb Antimony Content

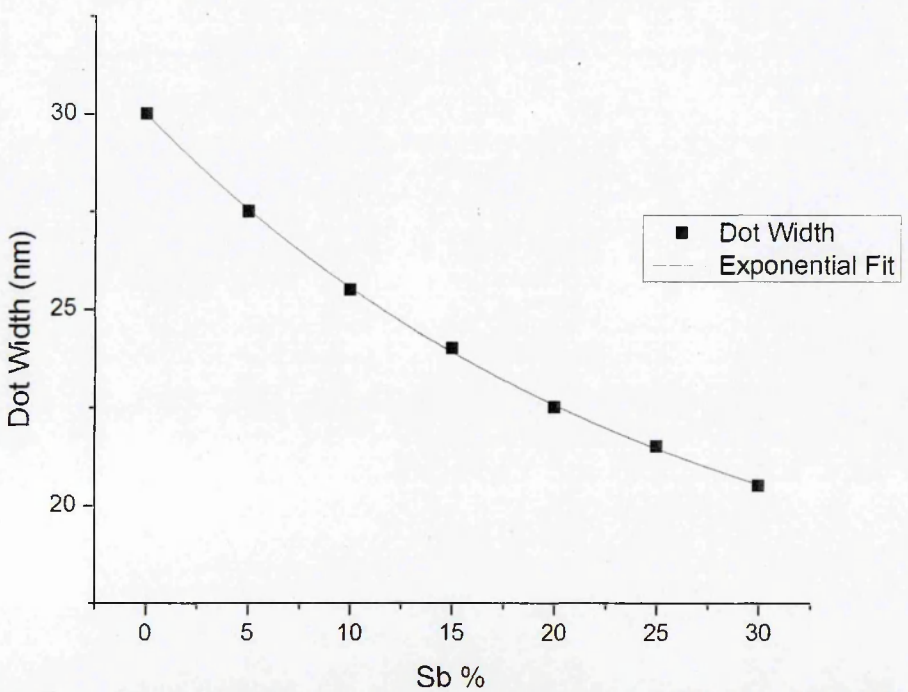

Figure 25: The required dot width to maintain an output energy of 682meV at 10K with increasing antimony content.

As the energy of the dominant peak is known to be 684.7meV for a fixed height of 10nm, the width and antimony content were varied so that the energy was constant at this value. The simulated results are shown in figure 25. At zero antimony content ie pure InAs dots, the width that gives an energy which corresponds to the experimental data is 30nm, reducing this by the calculated factor of ~13% a target width value of 26nm is gained. For a width of 26nm the antimonide content that gives the correct energy is then ~10%. These figures were then used and final values of 10nm x 25.5nm and 10% are used for future calulations which result in a conduction to valence band transistion energy of 681meV. For the selected value to be correct some assumptions must be made; the antimony fraction is constant in all of the dots. The dots always form a truncated pyramid the same shape as the pure InAs dots from earlier.

4.6.3.2 InAsSb Modelled Band Alignment

Using the approximated 10% antimony content the modelled band alignment including conduction band and valence band energy levels is shown in figure 26. The figure shows very little change from the InAs alignment shown earlier. The largest changes can be seen at the top of the pyramid (position =10nm) as the angle of the pyramid facets is fixed to the (011) plane, smaller width pyramids generate have smaller facets at the top, these smaller facets increase the strain on the top facet resulting in the band bending behaviour seen in figure 26 where at the pyramids top the LH band is found above the HH band, this is a known effect of tensile strain. This tensile strain can be seen in figure 27, where strain profile of 38.5nm InAs quantum dots and 26.5nm $InAs_{0.9}Sb_{0.1}$ quantum dots are viewed side by side. The increased strain can clearly be seen at the smaller top facet of $InAs_{0.9}Sb_{0.1}$ truncated pyramid.

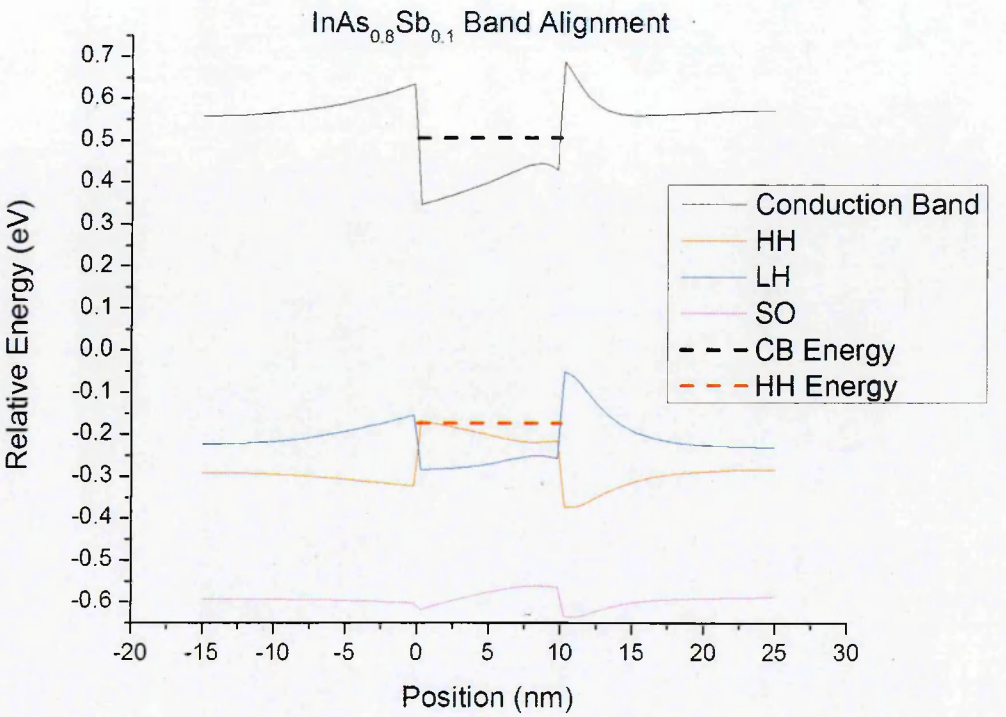

Figure 26: The simulated band alignment of $InAs_{0.9}Sb_{0.1}$ this differs from the pure InAs case by the addition of band bending at the 10nm position. This band bending is caused by increased tensile strain at the pyramid apex as shown in figure 27.

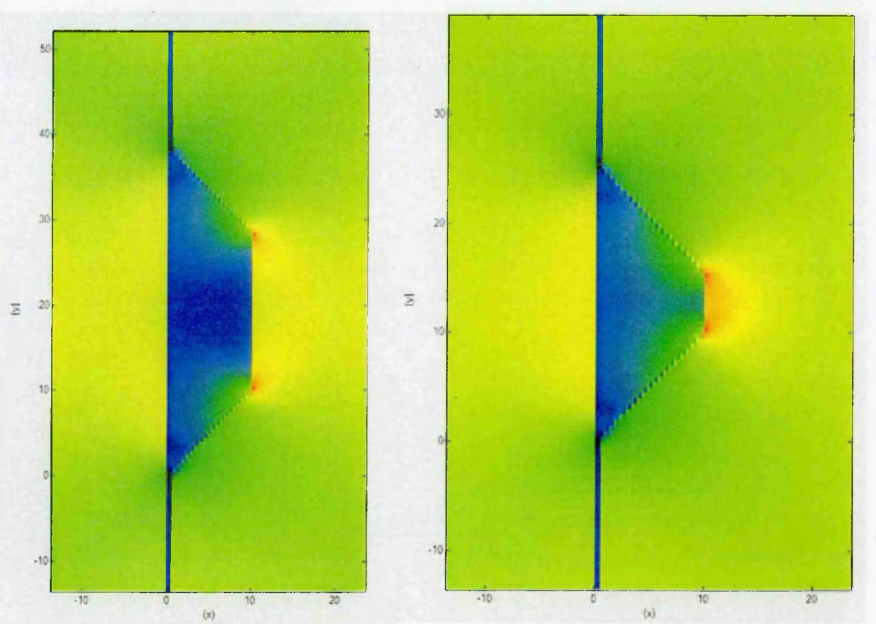

Figure 27: The simulated strain profile of InAs and $InAs_{0.9}Sb_{0.1}$ with red indicating increased strain. This shows an increase in strain at the pyramid apex as a result of smaller base widths being used.

4.6.3.3 InAsSb Effect of Width

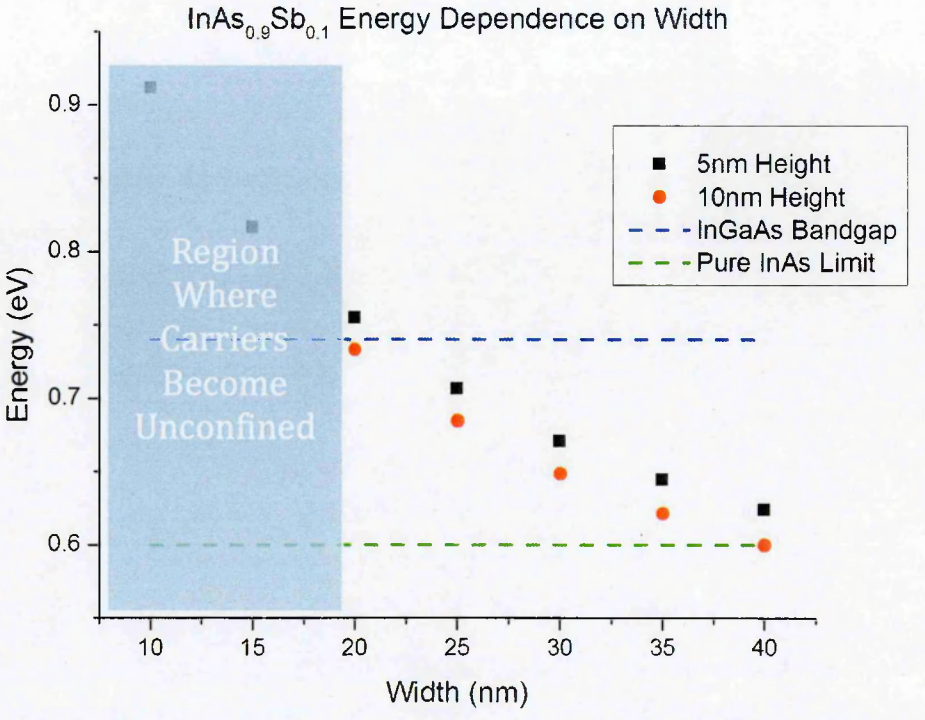

Figure 28: The InAsSb energy dependence on width calculated with a 10% antimonide content.

With the simulation model in place, we can now model the effect of dot width for a fixed antimonide concentration; this is shown in figure 28. As for the InAs quantum dots, increasing the highest of the dot lowers the energy due to a lowered wavefunction confinement. The model has already predicted the dimensions of the higher energy peak to be 10nm x 25.5nm , the lower energy peak would need to be ~10nm x 30nm to have the measured energy. The model again predicts a bimodal dot distribution as seen in the InAs case. The energy separation between the 5nm and 10nm height dots is now ~20meV, this reduction from the pure InAs case can be attributed to the reduction in top facet when the dot height is 10nm as shown in figure 27. Both of the data sets seem to trend towards 0.6eV as was the case with pure InAs dots, this is not unexpected as there is a small antimony fraction to the alloy.

4.6.4 Temperature Dependent PL Results

PL measurements were taken with increasing temperature, and each of the plots was fitted in the same way as outlined above. The resulting data of peak energy position with temperature for each of the four sample pieces along with the simulated data is shown in figure 29. As the temperature was increased past 40K for samples C and D the lower energy peak was no longer visible, and made no contribution to the integrated intensity.

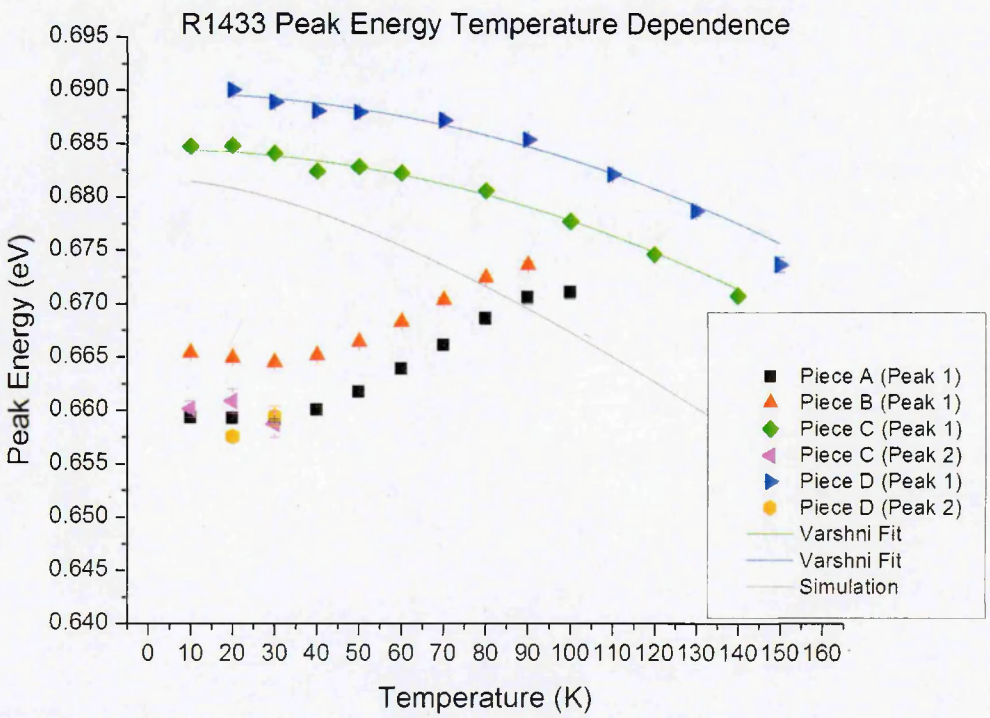

Figure 29: The fitted peak energy dependence on temperature for each of the four sample pieces A-D.

The primary peak for pieces C and D are fitted using the Varshni equation [33]. The reduced R^2 values for the fits are $R^2 = 0.86754$ for piece C, and $R^2 = 0.90395$ for piece D. These values indicate the Varshni fit is a reasonably accurate fit to the data. The material dependent parameters α and β, used to achieve this fit are given in table 4. While the values presented give a reasonable reduced R^2 value and visual fit to the data, they are far from both the accepted literature or simulated values. Therefore like for the previous InAs quantum dots the Varshni fitting is inappropriate for use on the InAsSb quantum dots.

	α (meV/K)	β (K)
Bulk InAs	0.276	93
Bulk InSb	0.32	170
$InAs_{0.9}Sb_{0.1}$ Simulation	0.289±0.001	97.1±0.3
Piece C	0.145±0.001	217±0.4
Piece D	0.110±0.1	174±19

Table 4: Simulated and experimentally fitted Varshni Paramters

There are two key points shown in figure 29 that must be addressed: (1) the sample pieces seem to be separated into two distinct groups. Pieces A and B display a temperature dependent blue shift, while pieces C and D display a temperature dependent red shift. The reason for this difference will be discussed in detail in a future section. (2) Within each blue or red shifting group, the samples emission wavelengths at 10K are within 5meV, yet are not identical as would be expected.

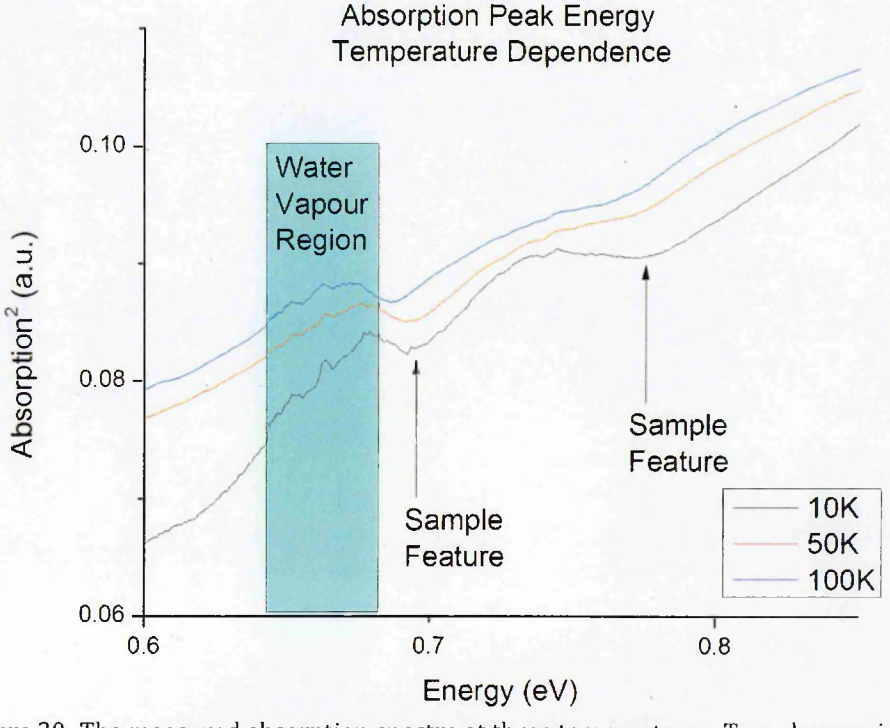

Figure 30: The measured absorption spectra at three temperatures. Two changes in gradient indicating features are seen at 690meV and 770meV.

As there are two pieces that red shift and two pieces that blue shift with temperature, absorption measurements were performed to try and establish the "normal" band edge behaviour independently of carrier occupation within the energy bands. Figure 30 shows the temperature dependent absorption spectra for sample piece B. In the figure a feature that red shifts with temperature can be seen at 690meV which is in agreement with the higher energy dot peak. It is also in agreement with the simulation as they both show a temperature dependent red shift. There is another feature at 770meV which corresponds to the $In_{0.53}Ga_{0.47}As$ barrier layer. There is no feature seen in the spectrum at 660meV to correspond to the lower energy dot peak. This could be due to interference in the spectrum due to water absorption between 640meV to 670meV that cannot be normalised out of the spectrum as the amount of water vapour present in the air changes with humidity.

4.6.2.1 Difference in Peak Emission Wavelength

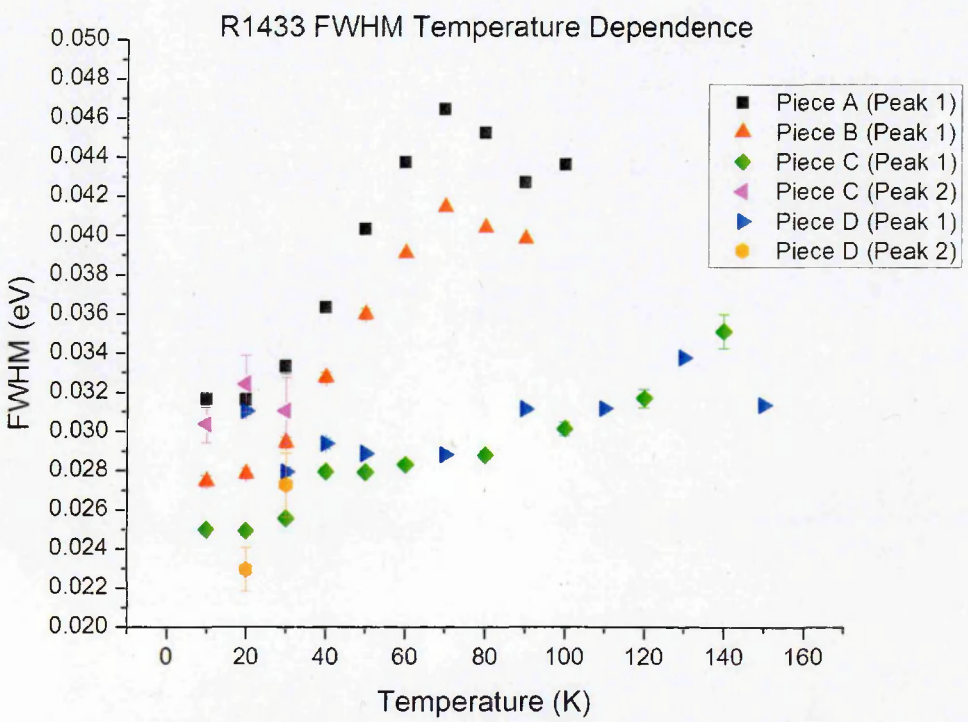

Figure 31: The fitted peak FWHM dependence on temperature for each of the four sample pieces A-D.

The difference in peak emission wavelength of ~5meV within the two groups can be explained by the samples originating from different points on the wafer. During semiconductor growth the wafer is constantly being rotated around its centre, this results in thicker mid-section when compared to the edge width. For this reason the very edge pieces of wafer are often discarded. This difference in growth thickness is often seen as slight variations in the emission spectrum wavelength. This argument can be justified by considering the measured peaks FWHM and integrated intensity with temperature. Sample pieces taken from the wafer edge often have wider less intense peaks. The FWHM and integrated intensity for all four pieces of sample R1433 are shown in figures 31 and 32 respectively. The figures show that the FWHM of both pieces C and D have a small linear dependence with temperature, the integrated intensity of piece D is shown to be less than of piece C. This is consistent with the pieces being from different positions of the same wafer, with piece D being closer to the edge. As it is not documented where these sample pieces originated from on the wafer this

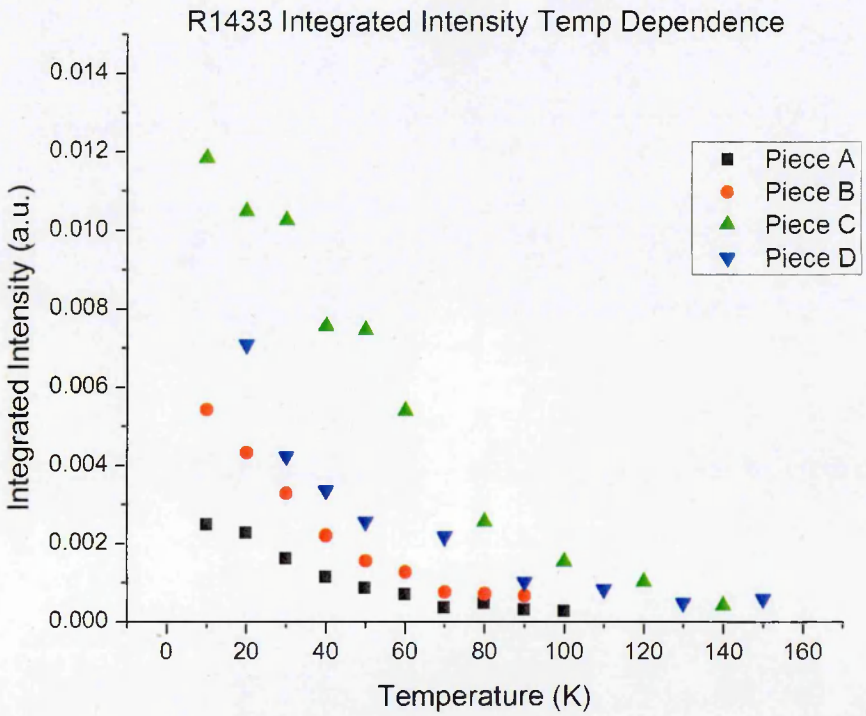

Figure 32: The measured spectra integrated intensity dependence on temperature for each of the four sample pieces A-D.

is speculation, but is a reasonable explanation for the shift. Furthermore during semiconductor growth the wafer is heated, this can cause a bowing of the wafer if the heat distribution is not constant, any bowing of the wafer would cause a non-uniform strain in the substrate. An important effect when considering SK quantum dot growth as the formation of 3D islands is dependent on strain.

4.6.2.2 Bi-Modal Dot Distribution

The idea of a bimodal dot distribution has been introduced by the simulation in a previous section. However, as was seen in for the InAs dot structure the carriers in the higher energy dots will usually redistribute to the lower energy dots with increasing temperature. This would not explain the disappearance of the lower energy peak with increasing temperature in samples C and D, and also the apparent blue shift for samples A and B.

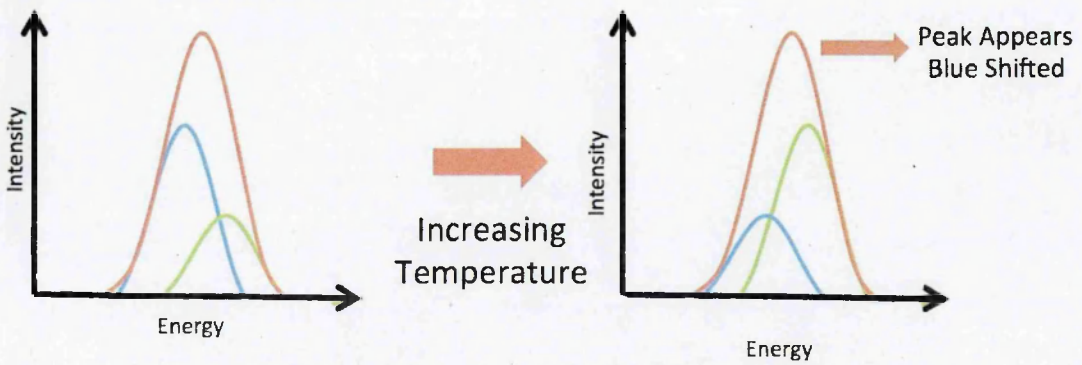

Figure 33: The apparent blue shift caused by a change in peak dominance.

The temperature dependence shown in figure 29, implies that the temperature dependent blue shift in samples A and B is reducing with temperature, and if extrapolated could conceivably begin to follow the red shifting behaviour of samples C and D. This can be explained using bimodal dots as a change in dominance from one dot group to the other. For this change in dominance to manifest as a blue shift, the experimental data would consist of two oscillators, a high energy and a low. As the temperature increased the low energy oscillator would reduce in intensity and the high energy oscillator increase. The overall effect would appear to be a blue shift in the resultant contribution of both

oscillators. As shown in figure 33. For this to occur carriers would need to transition from a lower energy dot to a higher energy.

There are two possible theories as to how this movement in carriers from a low energy dot to high energy dot occurs; (1) there is a strong band filling effect in the low energy dots. As the energy band is filled the carriers are at higher energy, at a critical point the ground state of the high energy dots may be a lower energy than the filled states of the low energy dots. Thermal redistribution would then move carriers from the low to high energy dots. (2) The low energy dots contain little to no antimony. It can be seen from the previous InAs dots that a dot energy of 662meV was obtained for an InAs dot size of 10nm x 35nm. To obtain the same energy using $InAs_{0.9}Sb_{0.1}$ requires a dot size of 10nm x 30nm. The dominant peak was simulated to have 10nm x 25.5nm dots. If the low energy dots do contain antimony then a change in strain is required to make the dots substantially larger while having the same alloy fraction. However, if the dots have no antimony then no change in strain is required to form the InAs dots. Furthermore, from the previous work it can be seen that the InAs have less confinement, allowing thermal redistribution of carriers from the low energy dots to the high energy dots.

4.6.2.2.1 Band Filling Effect

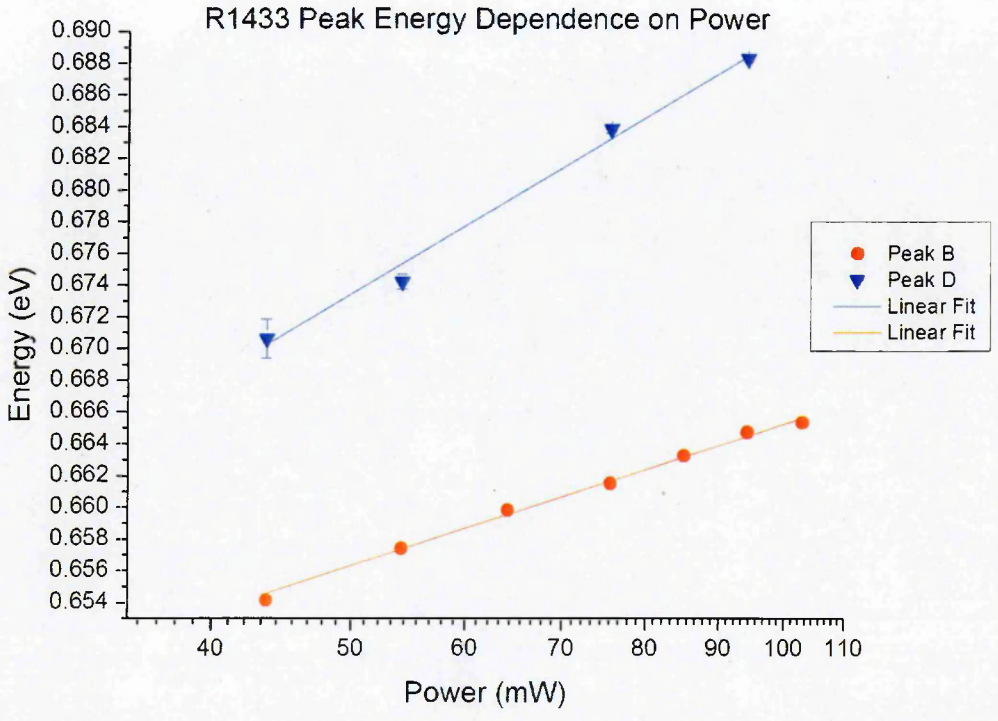

Figure 34: The measured change in peak energy with increasing power, the laser spot size was 1mm^2.

The band filling theory can be tested directly using power dependent measurements. The peak emission energy of sample B and D were measured at different pump powers. A band filling effect was found as can be seen in figure 34, this is shown by the peak energy value increasing as a function of increasing power. Note, although piece D has been fitted with two oscillators throughout this chapter, the SNR decreased so rapidly that a two oscillator fitting could not be accurately used., instead a one oscillator was used. The data was fitted using a linear fit as the power range is small. For larger power ranges it is expected that a non-linear dependence is found as the band curvature dictates the energy level spacing, and for higher energies the spacing between levels is smaller. The filling effect in piece B is calculated to be 0.43 ± 0.05 meV/mW, and for piece D is calculated to be 0.99 ±0.19 meV/mW for a 1mm^2 spot size. If the high energy oscillator had no band filling effect then piece D the combination of both oscillators would have the same filling gradient as piece B. Since the gradient is approximately twice the value found for piece B it can be deduced that both the

high and low energy oscillators display a band filling effect and this effect is approximately equal in both.

Due to these findings the transition of carriers from the low energy to high energy dots due to the band filling argument outlined above is not correct for this sample. Instead it is likely that the lower energy dot group contains no antimony.

4.6.2.2.2 Power Dependent Measurements

The power dependence of the sample was also measured to determine if the dots would make efficient devices i.e. is the dominant recombination process radiative as was the case for pure InAs dots. This power dependence was also performed at two different temperatures 10K and 50K. This was done to determine if a change in dominant recombination process was occurring with temperature, and thus would there be a limitation on the device efficiency with temperature of a device made from these dots. Also as the sample contains bimodal dots any difference in the recombination process between the dot groups will become apparent.

The integrated intensity of the emission was determined at increasing powers and the results are shown in figure 35 for piece D and 36 for piece B. Referring back to the power analysis performed during the theory chapter of this thesis the gradient of these lines reveals information about the dominant recombination process in a semiconductor. In the case of piece D a gradient of 2.00 ± 0.11 is measured at 10K and 2.00 ± 0.05 at 50K, this indicates that the dominant process being observed here is defect-related recombination and remains that way at all measured temperatures. This change to a defect dominated recombination process is not unexpected as the addition of antimony to an InAs dot structure would increase the number of defects because of the larger lattice mismatch if the atoms.

In sample B (figure 36), there is a change in gradient, at 10K the gradient is 1.13 ± 0.04 meaning a dominant radiative recombination process, while at 50K the

gradient has changed to 2.00 ± 0.11, a dominant defect related recombination process. This indicates a change from a dominant radiative recombination process to a dominant defect related recombination process with increasing temperature. This provides evidence that the observed blue shift is the result of a change in oscillator dominance from the low energy dots (the radiative dominated type) to the high energy dots (the defect dominated type).

Furthermore, the change from a radiative to defect related process implies that the lower energy bimodal dot group contains very little antimony. The pure InAs dots investigated earlier show the same peak emission wavelength and recombination process as the low energy dot group.

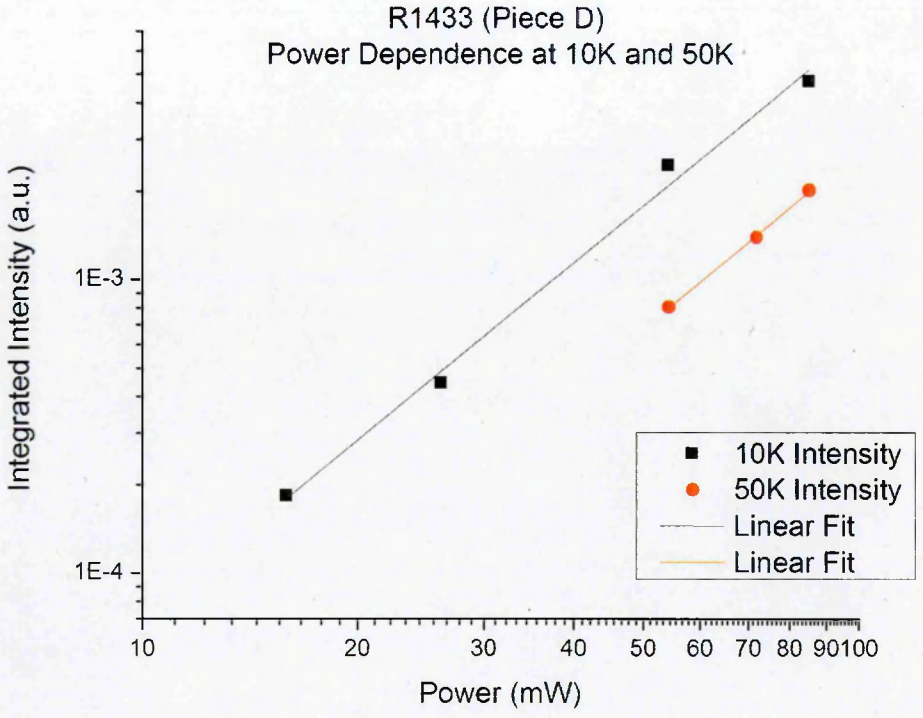

Figure 35: The measured power dependence of R1433 piece D, showing a dominant defect related recombination process at 10K and 50K.

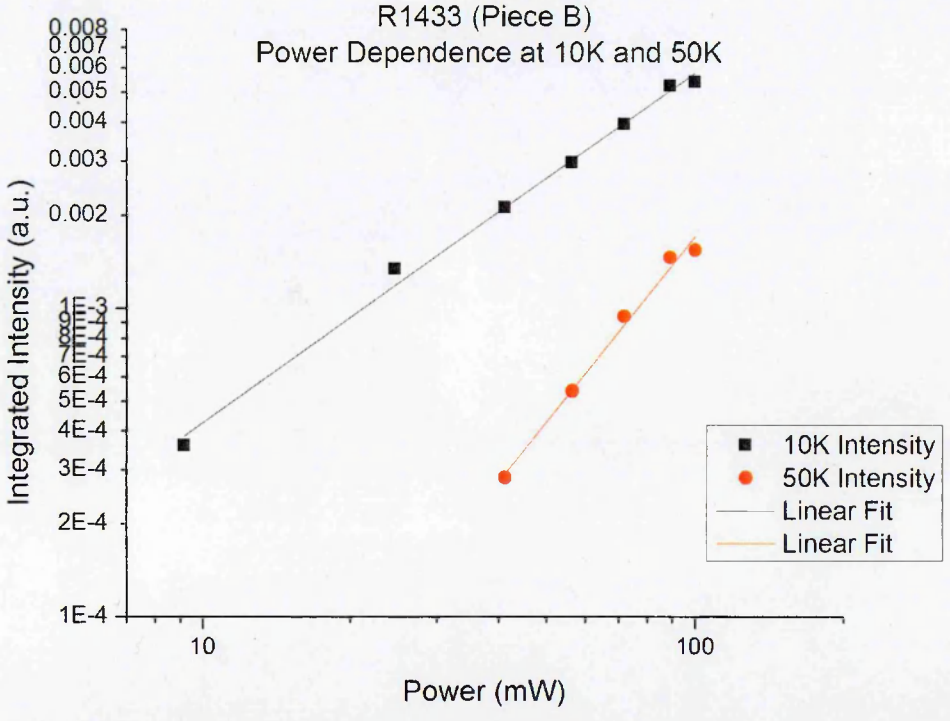

Figure 36: The measured power dependence of R1433 piece B, showing a dominant radiative recombination process at 10K, and a dominant defect related recombination process at 50K.

4.6.5 Conclusions

As a follow on piece of work from the previous InAs quantum dots, Antimony was added to the quantum dot layer. It has been described though how using the SK dot growth technique it is impossible to accurately know the antimony quantity added during growth, instead only an antimony exposure time is known. Using the dot morphology review an estimate for the reduction in dot size due to the increased lattice mismatch of antimony was estimated to be 13%. Based on this assumption truncated pyramidal dots of InAsSb were simulated using an antimony fraction of 10%, as this best fitted both the calculated reduction in dot size and experimentally fitted emission wavelength.

The experimental data showed two distinct groups of samples, one that undergoes a temperature dependent red shift, and another which undergoes a temperature dependent blue shift. After fitting the data the blue-shifting group was found to be accurately modelled by a single Gaussian oscillator, while the red shifting dot group required two oscillators. From this fitting it was also noticed that the single blue shifting oscillator was identical to the low energy oscillator of the red shifting group.

From this information it was theorised that there were bi-modal quantum dots in the sample. This bimodal behaviour explains the two oscillators found in the red shifting group, and through a change in dominance with temperature could also explain the temperature dependent blue shifting behaviour.

Power dependent studies confirmed this change in dominance by showing that he blue shifting group moved from a dominant radiative recombination process to a dominant defect related process with temperature. This also indicated from the earlier work on InAs dots that some of the dots contained no antimony. Therefore showed a dominant radiative recombination as previously observed in the InAs dots. The Antimony containing group were dominated by defect related recombination due to the increased lattice mis-match.

4.7 Overall Conclusions

During this chapter two similar groups of quantum dots have been investigated. These pure InAs and InAsSb dots both emitted at a similar wavelength ~657meV and 665meV, but achieved this wavelength by different means. The Pure InAs dots had a larger width than the InAsSb dots allowing a longer wavelength, while the antimony containing dots had a smaller bandgap. This indicates that if the InAsSb dots could be grown to a larger width a longer wavelength peak could be achieved.

Through modelling of the dot structure using the Nextnano software package it has also been shown that under these growth conditions the InAs(Sb)/InGaAs/InP dots tend to form a bimodal dot distribution. This illustrates the point made during the justification of this work, that understanding the physics behind the emission can help future work. While each of the experimentally measured peaks appear at first glance to consist of a single oscillator, the modelling and fitting performed in this work proves this assumption to be false.

Furthermore, the study of the InAsSb dots temperature dependent blue shift, reveals that a likely explanation for the behaviour is bimodal dots. One group of which contains no antimony at all, while the other has ~10% antimony composition. This indicates a problem during growth, with the lack of antimony inclusion in one group this indicates a non-uniformity of antimony across the wafer, but no metallic clustering of antimony. This is important for future growth and extending the dot emission wavelength through higher antimony fractions.

4.8 References

[1] Z. Yin et al., *"A review of energy bandgap engineering in III–V semiconductor alloys for mid-infrared laser applications"*, Solid State Electronics 51, 6-15, (2007)

[2] P. Norton, *"HgCeTd Infrared Detectors"*, OPTO-ELECTRONICS REVIEW 10(3), 159–174 (2002)

[3] K. Vizbaras et al., *"Room-temperature 3.73 μm GaSb-based type-I quantum-well lasers with quinternary barriers"*, Semiconductor Science and Technology 27 (2012)

[4] C. L. Felix et al., *"High-Temperature 4.5μm Type-II Quantum-Well Laser with Auger Suppression"*, IEEE Photonics Technology Letters 9, 6 (1997)

[5] N. Bandyopadhyay et al., *"Room temperature continuous wave operation of λ ~ 3–3.2 μm quantum cascade lasers"*, Applied Physics Letters 101, 241110 (2012)

[6] O. Cathabard et al., *"Quantum cascade lasers emitting near 2.6μm"*, Applied Physics Letters 96, 141110 (2010)

[7] S. J. Sweeney et al., *"The Effect of Temperature Dependent Processes on the Performance of 1.5μm Compressively Strained InGaAs(P) MQW Semiconductor Diode Lasers"*, IEEE Photonics Technology Letters 10, 8, 1076 (1998)

[8] D. L. Huffaker et al., *"1.3μm room-temperature GaAs-based quantum-dot laser"*, Applied Physics Letters 73, 2654 (1998)

[9] Y. Qui et al., *"High-performance InAs quantum-dot lasers near 1.3μm"*, Applied Physics Letters 79, 3570 (2001)

[10] K. Mukai et al., *"1.3μm CW Lasing of InGaAs–GaAs Quantum Dots at Room Temperature with a Threshold Current of 8 mA"*, IEEE Photonics Technology Letters 11, 10, 1205 (1999)

[11] S. A. Sayid et al., *"Efficiency limiting processes in 1.55μm InAs/InP-based quantum dots lasers"*, Applied Physics Letters 97, 161104 (2010)

[12] Y. Masumoto et al., *"Semiconductor Quantum Dots: Physics, Spectroscopy and Applications"*, Page 149 (2002)

[13] I. N. Stranski et al., Sitzungsber. Akad. Wiss. Wien, 146 (1938)

[14] M. Sugawara, *"Self Assembled InGaAs/GaAs Quantum Dots"*, Semiconductors and Semimetals Volume 60, Page 120 (1999)

[15] B. J. Reil, *"An introduction to self-assembled quantum dots"*, American Journal of Physics, 76, 750 (2008)

[16] J. S. Lee et al., *"Low-index facet formation in InGaAs islands on GaAs (n11)B substrates "*, Journal of Crystal Growth 221, 586 (2000)

[17] H. Saito et al., *"Shape Transition of InAs quantum dots by growth at high temperature"*, Applied Physics Letters 74, 1224 (1999)

[18] Q.D. Zhuang et al., *"Effects of rapid thermal annealing on self-assembled InGaAs/GaAs quantum dots superlattice"*, Journal of Crystal Growth 208, 791 (2000)

[19] H. Saito et al., *"Shape Transition of InAs quantum dots by growth at high temperature"*, Applied Physics Letters 74, 1224 (1999)

[20] J. M. Garcia et al., *"Intermixing and Shape Changes During the Formation of InAs Self Assembled Quantum Dots"*, Applied Physics Letters 21, 2014 (1997)

[21] Z. Yin et al., "Effect of $In_xGa_{1-x}As$ matrix layer on InAs quantum dot formation and their emission wavelength", Journal of Applied Physics 100, 033109 (2006)

[22] R. M. Biefeld, *"The metal-organic chemical vapor deposition and properties of III-V antimony-based semiconductor materials"*, Materials Science Enginering R 36, 105 (2002)

[23] I. Vurgaftman et al., *"Band parameters for III–V compound semiconductors and their alloys"*, Journal of Applied Physics 89, 11, (2001)

[24] Yueming Qiu et al., *"Room-temperature continuous-wave operation of InAsSb quantum-dot lasers near 2 μm based on (001) InP substrate"*, Applied Physics Letters 84, 263 (2004)

[25] J. Kotani et al., *"Mid-infrared emission from InAs quantum dots, wells and dot on well nanostructures grown on InP (100) by MOVPE"*, Journal of Applied Physics 106, 093112 (2009)

[26] T. Xiaohong et al., *"Mid-infrared emissive InAsSb quantum dots grown by metal–organic chemical vapor deposition"*, Crystal Engineering Communications , 15, 604 (2013)

[27] W. Lei et al., *"Engineering the composition, morphology and optical properties of InAsSb nanostructures via graded growth technique"*, Applied Physics Letters 102, 033111 (2013)

[28] O. Gustafsson et al., *"Long-wavelength infrared photoluminescence from InGaSb/InAs quantum dots"*, Infrared Physics & Technology 59, 89–92 (2013)

[29] Z. Yin et al., *"Effect of $In_xGa_{1-x}As$ matrix layer on InAs quantum dot formation and their emission wavelength"*, Journal of Applied Physics 100, 033109 (2006)

[30] T.P. Pearsall et al., *"Photoluminescence and Impurity Concentration in GaInAsP Lattice-matched to InP"*, Journal of Applied Physics 52, pg.1037-1047 (1983)

[31] Nextnano Semiconductor Software Solutions, Accessed March 2013, http://www.nextnano.de

[32] Y. Qui et al., *"Self-Assembled InAsSb quantum Dots on (001) InP substrates"*, Applied Physics Letters 84, 1510 (2004)

[33] Y.P. Varshni, *"Temperature dependence of the energy gap in semiconductors"*, Physica 34, 1, 149–154, (1967)

Chapter 5 - High Pressure, Low Temperature investigations of an InAs/InAsSb Type II Superlattice

5.1 Introduction

Infrared photo-detection has many applications in the military, medicine, and for gas sensing [1]. In this chapter the key parameters that need to be considered when designing a new semiconductor material with photo-detection in mind will be discussed, and how well the existing technology fits these parameters. The suitability of new material systems will then be discussed, including the current development of InAs/InAsSb type II superlattice structures that are investigated in this chapter.

The experiments performed in this chapter have two main aims. Firstly to experimentally locate and identify the position of a defect state above the conduction band edge. This is achieved by the application of hydrostatic pressure to the semiconductor using a sapphire ball cell. This will push the conduction band ground state of the system to higher energy. If the defect state is present then it is predicted to cause a decrease in the measured PL intensity as carriers recombine via defects instead of recombining radiatively.

The second aim is to demonstrate the use of the sapphire ball cell to provide the ability to make high pressure measurements at low temperatures. While this can be achieved with other systems such as the diamond anvil cell (DAC) or hydraulic gas pressure systems, neither of these can compare with the operational simplicity of the sapphire ball cell.

5.1.1 Useful Parameters in Photo-detector Design

When designing new material systems with the aim of photo-detection there are key parameters which should be considered [2]. The primary concern is the semiconductor band gap and the ability to tune this band gap. Detection will occur when an incident photon of energy greater than the band gap (E_g) excites an electron from the valence band to the conduction band. This means the semiconductor band gap determines the photo-detector's operational range, and the materials sensitivity to alloy composition and temperature will change this band gap.

The importance of the material band gap and the requirement to be able to absorb incident photons leads to the second parameter; This is having a direct band gap with high absorption coefficient. While a direct band gap is not a strict requirement for a good photo-detector, a direct band gap semiconductor will give a sharp optical absorption onset compared to an indirect band gap semiconductor [3]. Indirect band gap semiconductors such as silicon have a smoother optical absorption onset [3]. A high absorption coefficient is required to absorb most of the incident photons while remaining as thin as possible. Increasing the thickness of the active region will increase the fraction of photons absorbed, but this also increases the growth complexity and cost [2] and can lead to fabrication difficulties.

The thermal expansivity of the semiconductor material is an important factor when designing liquid nitrogen cooled detectors. The temperature dilation of the lattice will alter the band gap approximately linearly at high temperature, but at low temperature it is non-linear and behaves according to the Varshni equation [4] thus changing the detection range. A large thermal expansivity will mean that small variations in temperature lead to large variations in the detector response range.

The choice of photo-detector active region is limited by the availability of lattice matching both alloy materials and growth substrate. As the semiconductor photo-detector will be used with traditional silicon based electronic circuitry a choice of growth substrate that will allow this easily integration is preferential, materials such as silicon, gallium arsenide, or indium phosphide are ideal. Lattice mis-match between the active region material or substrate leads to strain that will change the band structure of the semiconductor [5], as well as generating possible dislocations that could propagate through the device. However, strain is not always detrimental, in some devices for example strain has been shown to lower the threshold current and increase the efficiency through suppression of non-radiative Auger recombination processes in semiconductor lasers and to increase hole mobility in transistors [6].

	$Hg_{1-x}Cd_xTe$	InSb	$InAs/Ga_{1-x}In_xSb$ Superlattice	$InAs/InAs_{1-x}Sb_x$ Superlattice
Peak Detectivity (D*) ($cmHz^{1/2}W^{-1}$)	10^{10}	10^{11}	TBC	TBC
Bandgap Wavelength Range (μm)	0.7 - 25	2 - 4	3 - 25	4 - 12
Absorption coefficient (cm^{-1})	10^2 - 10^3	10^4	2500	TBC
Operating Temperature	77K	77K	10K	10K

Table 1: The important parameters for photo-detector design, and the known values for each of the photo-detectors in this work.

5.1.2 Mercury Cadmium Telluride (MCT)

While there are many detectors available for purchase that cover the infrared region with varying sensitivities, Mercury Cadmium Telluride ($Hg_{1-x}Cd_xTe$) (also known as MCT) detectors are currently the commercially available standard for mid-IR photo-detectors. They were first engineered as a direct band gap material for the long wavelength infrared region in 1957 [2], and have been under development since then.

The reason that they have become the standard is because they cover so many of the previously outlined parameters so well. One of the largest benefits is the very large wavelength coverage achievable. Through alloy composition the bandgap can be engineered to vary between 0.7μm and 25μm. This wide range of detection is not available in a single detector however, it is sectioned into ranges covered by individual detectors. The commercially available options from Infrared Associates Inc. is shown in figure 1 where D* is the specific detectivity of

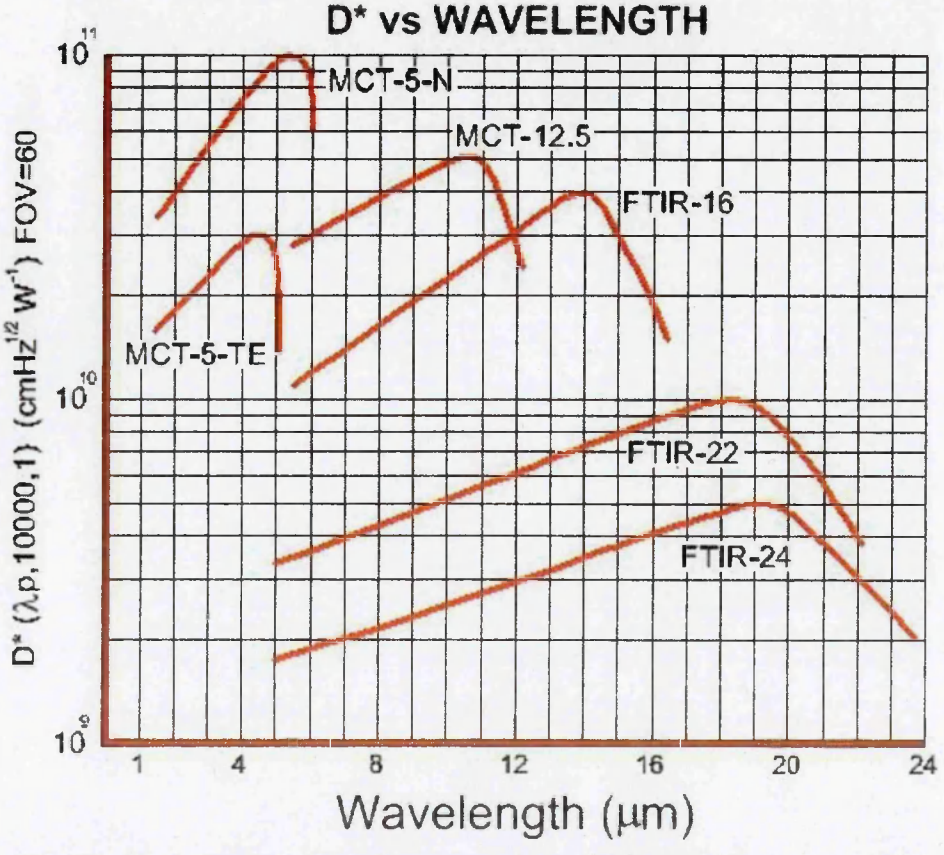

Figure 1: The response curves of commercially available MCT detectors available from Infrared Associates Inc. [7]. This shows the large wavelength coverage of MCT detectors.

the detector, defined by [8]:

$$D^* = \frac{\sqrt{A}}{NEP} \qquad (1)$$

Where A is the area of the active region, and NEP is the noise equivalent power i.e. the signal power that gives a SNR of one to one [8].

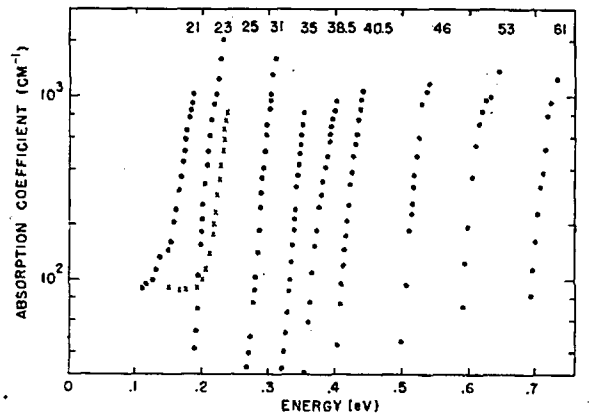

Figure 2: The room temperature absorption coefficients for $Hg_{1-x}Cd_xTe$. The numbers indicated the alloys x fraction. Adapted from ref [9].

$Hg_{1-x}Cd_xTe$ semiconductors also have the ideal direct band gap structure. This has been studied previously by M. W. Scott [9] and shows a sharp optical absorption onset and high absorption coefficient through a wide range of alloy compositions. The data from these experiments taken at room temperature is shown in figure 2. This effect can be seen in commercially available detectors in in figure 1, as the range of detection becomes longer the response of the detector is reduced. This is a direct effect of the higher *x* fraction in the $Hg_{1-x}Cd_xTe$ alloy reducing the absorption coefficient.

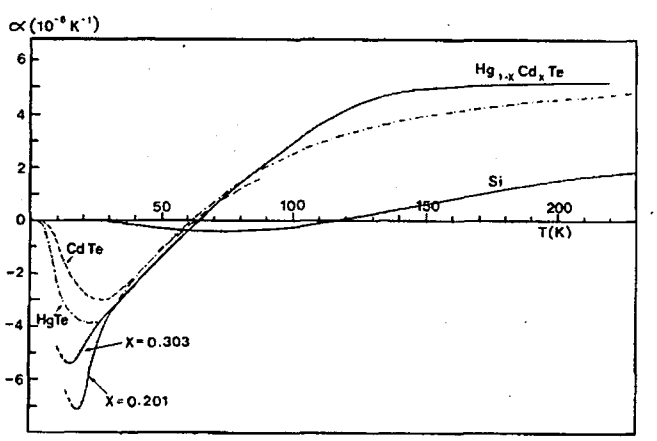

Figure 3: The thermal expansivity coefficient α vs Temperature for $Hg_{1-x}Cd_xTe$. Adapted from [10]. At 77K the alloy independent region is shown.

As stated earlier the thermal expansivity is important as this will effect the lattice dilation and therefore band gap. The thermal expansivity of $Hg_{1-x}Cd_xTe$ has been

well studied and does not vary greatly with temperature; this is shown in figure 3. Also shown in figure 3 is the expansivity of silicon for camparison. It has also been documented that above temperatures of 30K the alloy thermal expansivity is independent of alloy composition within 5% [10], which is the case at liquid nitrogen cooled temperatures under which MCT detectors are usually operated.

When considering the availability of lattice matched substrates for II-VI materials there are materials of similar lattice constant with higher bandgaps

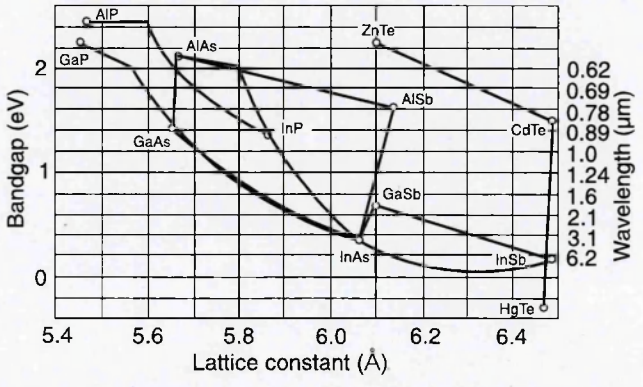

Figure4: The lattice constant and bandgap of several common semiconductor materials also included are the II-VI materials. Adpated from [2]

readily available, unlike for the III-V materials. The lattice constants of several common semiconductor materials is shown in figure 4 including the II-VI materials HgTe, CdTe, and ZnTe. There is a 0.023Å difference in lattice constants of HgTe (6.468Å)[11] and CdTe (6.491Å)[12] measured at 300K, resulting in a negligible amount of strain being produced between the materials from lattice mismatch. The substrate usually chosen for growth is then an alloy of $Cd_{1-x}Zn_xTe$, this is because adding 4% ZnTe to CdTe results in an alloy lattice matched to $Hg_{1-x}Cd_xTe$ [2], again resulting in a negligible amount of strain between the substrate and active region.

5.1.2.1 Indium Antimonide (InSb)

Indium Antimonide detectors are used throughout this work, for the spectroscopic studies. InSb detectors are not considered as $Hg_{1-x}Cd_xTe$ replacements, as they have a much narrower wavelength range of operation. They are used in this work however as they have a much higher detectivity in the 2μ-4μm wavelength region of interest. Figure 5 shows the D* values for all of the commercially available detectors from Hamamatsu [13], from it can be seen that there are detectors with a higher D* value than InSb, but InSb has the most stable response over the 2-4μm range.

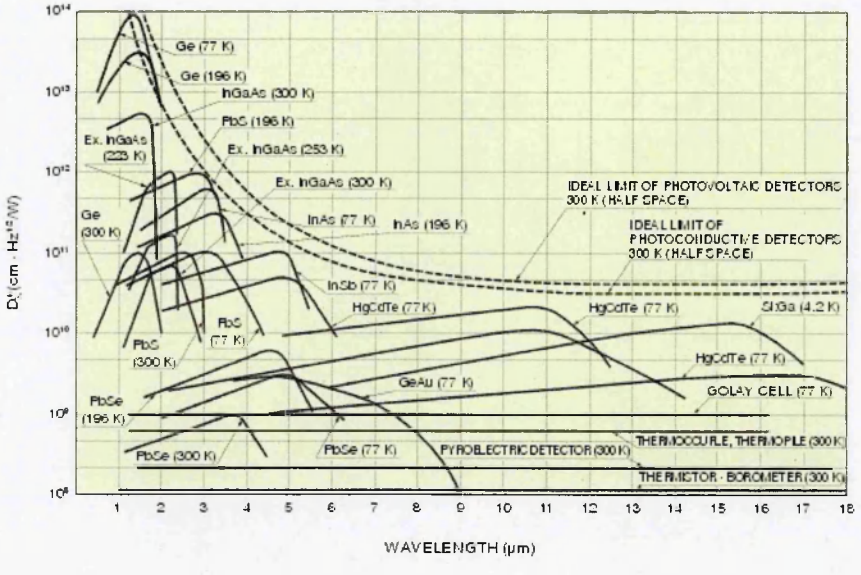

Figure 5: The detectivity of various photo-detectors with increasing wavelength. Adapted from [13].

5.1.3 Superlattice alternatives

Despite the dominance of $Hg_{1-x}Cd_xTe$ photo-detectors in the mid-IR detection market, there are alternatives in the form of antimonide based type-II superlattices. These superlattice structures are predicted to have similar optical properties as the $Hg_{1-x}Cd_xTe$ mid-IR detectors, while having much improved electrical properties. The first structure to be considered is the InAs/InGaAs

type-II superlattice, this is the first generation of superlattice structure able to compete with $Hg_{1-x}Cd_xTe$ detectors. This also provides the theoretical foundations upon which the currently developing InAs/InSb type-II superlattice structure experimented on in this thesis is based. Secondary to the predicted electrical improvements, these superlattice materials are also less harmful to the environment than mercury and cadmium.

5.2.3.1 InAs/$Ga_{1-x}In_xSb$

The InAs/$Ga_{1-x}In_xSb$ superlattice structure was proposed by D. L. Smith et al. in 1987 [14] as an improvement over existing InAs/GaAs superlattice structures. In an InAs/GaSb superlattice the bottom of the InAs conduction band is below the top of the GaSb valence band. In this situation the electrons and holes become localised to layers, with the electrons occupying the InAs layer and holes the GaSb layer. With sufficiently thin layers the electron and hole wavefunctions are weakly confined resulting in an electron/ hole mini-band being formed. This leads to the optical energy gap being created from the separation between the mini-bands [15]. This results in an unusual band alignment where the resulting optical band gap can be smaller than the band gap of either of the constituent materials. Furthermore, the optical transition energy is now also controlled by the layer thickness, and is also affected by the conduction and valence band offset, and the electron and holes effective mass. InAs/$Ga_{1-x}In_xSb$ superlattices share this localised carrier structure but the addition of indium reduces the defect related recombination in the forbidden bandgap region, this will be discussed further in a later section.

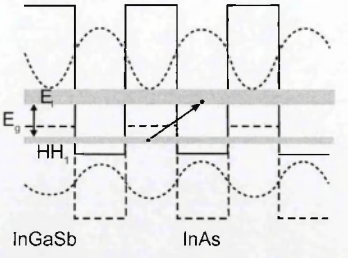

Figure 6: The InAs/$Ga_{1-x}In_xSb$ band structure formed including the electron and hole miniband. Adapted from [16].

In this structure the electrons and holes are now confined to different layers, making the bandgap spatially indirect. For optical transitions with a good oscillator strength the E1 and HH1 wavefunction need sufficient overlap [15]. To get the maximum overlap the layers are required to be thin, however to reach the mid-IR wavelengths thicker layers are needed. This results in the InAs/GaSb structure having poor optical properties for photo-detection. The addition of indium to the GaSb structure allows for the use of thinner layers while still reaching longer wavelengths. As a result the InAs/$Ga_{1-x}In_xSb$ superlattice has greatly increased optical properties compared to the InAs/GaSb superlattice. The band alignment is shown in figure 6.

Now that the formation of the electron and hole mini-band has been explained, the InAs/$Ga_{1-x}In_xSb$ superlattice will now be compared to the key parameters in

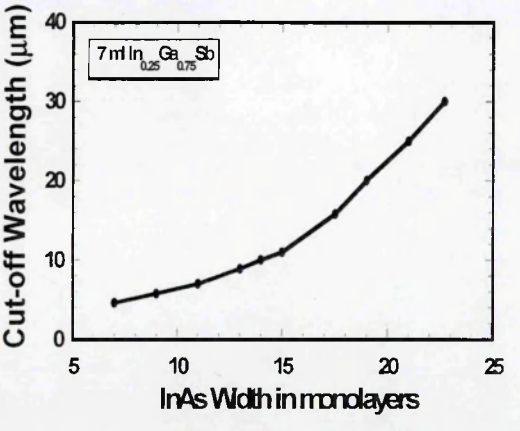

Figure 7: The change in cut off wavelength of the InAs/$Ga_{1-x}In_xSb$ superlattice ,while varying only the of InAs monolayer thickness. Adapted from [17].

the same way the $Hg_{1-x}Cd_xTe$ alloy has been. In the case of a superlattice structure however this is not as simple as the direct band gap case, due to the interdependency of variables. The band gap in the InAs/$Ga_{1-x}In_xSb$ superlattice can be varied by adjusting the InAs, or $Ga_{1-x}In_xSb$ layer thickness, as well as changing the *x* alloying fraction of indium content. However, changing the indium fraction will also change the absorption [15] coefficient of the superlattice. This allows for a response range of between 3μm and 25μm [16], with multiple alloy or layer combinations to reach these values. An example of the ability to change the optical band gap by changing only the InAs layer thickness is shown in figure 7. Figure 7 shows a superlattice of 7 monolayer thick $In_{0.25}Ga_{0.75}Sb$ and varying monolayer thickness InAs. There is a non-linear increase in the measured energy required to excite one electron from the valence band to the conduction band as the number of monolayers is increased.

It was discussed earlier that a direct band gap is required for a sharp absorption onset. The superlattice structures being discussed have a type-II band alignment, however, because of the de-localisation of electrons and holes, and in the case of thin layers the electron and hole wavefunctions are larger than the separation between layers. These effects lead to electron and hole mini-bands being formed. These mini-bands allow for the absorption onset to be sharp. The absorption coefficient for InAs/GaSb was already discussed to be poor due to the balance between thin layers to allow wavefunction overlap and thicker layers for longer detection wavelengths. The solution to this problem while increasing the detection wavelength and maintaining thins layers was the addition of indium. The effect that this has on the optical properties is shown in figure 8. This figure shows two effects; firstly the absorption coefficient increases across a range of wavelengths, rather than at one peak value, and secondly that the peak in the absorption coefficient is increased by almost a factor of four with the addition of 25% indium.

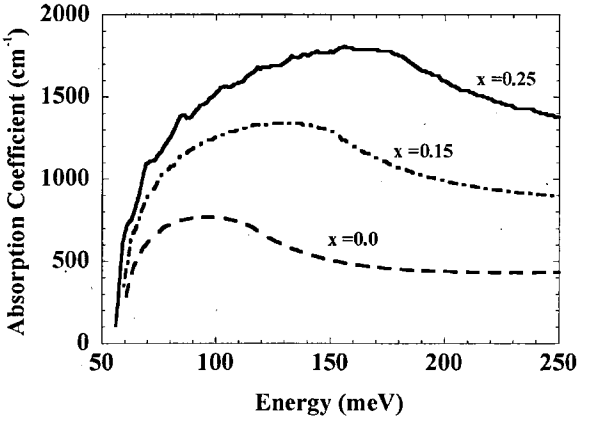

Figure 8: The increase in absorption coefficient by increasing the indium fraction in the InAs/$Ga_{1-x}In_xSb$ superlattice. Adapted from [15].

The thermal expansivity of the material is primarily a concern because the associated lattice dilation affects the detectivity wavelength of the semiconductor. The electron and hole mini-band wavelength are controlled by the layer thickness and alloy composition, as each layer in the superlattice has a different thermal expansivity, and in the case of the GaInSb layer this will also depend on the alloy composition, this becomes a very complex problem to examine. Instead we shall look at the case of an extreme wavelength change which has already been measured, the difference between 5K and 300K [18] shown in figure 9. The theoretical curve in the figure has been calculated for 0K, and the curves for 5K and 300K have been measured using a 37Å InAs, 19Å $Ga_{0.65}In_{0.35}Sb$ superlattice [18]. There is a shift in the absorption onset value to lower energy with increasing temperature of approximately 200meV which is a 20% change over the full temperature range. Most III-V semiconductors have a Varshni like shift with temperature [4], this function is approximately linear at higher temperature with a lower rate of change at lower temperatures. Without access to the data between 5K and 300K it shall be assumed the change is linear across the entire 5K to 300K range, this is much worse than the real behaviour at low temperature. This gives a calculated bandgap change of 0.6meV/K. This means for the cryogenic temperatures of liquid nitrogen (77K) the change in bandgap per Kelvin is less than and is considered negligible when compared with the semiconductor bandgap.

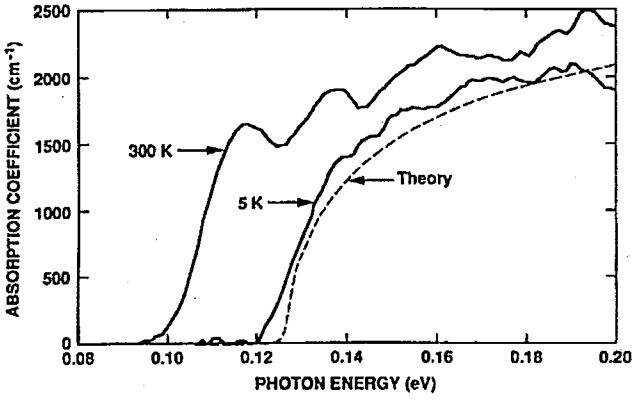

Figure 9: The change in band gap and absorption coefficient with temperature for a 37Å InAs, 19Å $Ga_{0.65}In_{0.35}Sb$ superlattice. Adapted form ref [18].

Finally we consider the lattice constant of the superlattice, and the potential for growth substrates. Figure 4 shows the lattice constant for the III-V materials, and it can be seen from this why low InSb fractions are used for superlattice growth. The large mismatch between InSb and GaSb will cause strain at the InAs / GaInSb interface because of the increasing lattice mismatch. It can also be seen that the choice of growth substrate is limited because of this large lattice constant. GaSb is usually chosen because of its close lattice match to both of the superlattice materials, however groups have attempted growth on lower cost GaAs and silicon [15], both of these substrates lead to a large amount of defects propagating through the structure due to the large lattice mismatch.

From the points made so far, it is noted that the InAs/$Ga_{1-x}In_xSb$ superlattice is at best equal to the currently available $Hg_{1-x}Cd_xTe$ photo-detectors. However, the ability to engineer the InAs/$Ga_{1-x}In_xSb$ superlattice to optimise the required properties makes it potentially superior. The higher effective mass of conduction band electrons in the superlattice ($m_e=0.03m_0$) compared to $Hg_{1-x}Cd_xTe$ ($m_e=0.01m_0$) leads to a lower tunnelling length. Tunnelling is a component of the dark current and is a limiting factor in the performance of very long wavelength infrared (VLWIR) $Hg_{1-x}Cd_xTe$ detectors [19]. As the tunnelling is reduced in superlattice structures, the tunnelling contribution to the dark current is negligible. This means a lower overall dark current [19, 20].

The Auger recombination component can also be reduced through engineering the HH and LH bands to have a larger separation. This reduction in Auger recombination leads to longer carrier lifetimes for superlattice structures [21, 22]. The reduction in Auger recombination has been used to theoretically calculate the high temperature operation of a superlattice detector; this work found that superlattices have the potential to maintain the same D* performance as the equivalent $Hg_{1-x}Cd_xTe$ detector while being at a temperature 15K higher [23].

5.2.3.2 InAs/$InAs_{1-x}Sb_x$

Though it has been shown that there is a small contribution to the dark current from tunnelling effects, InAs/$Ga_{1-x}In_xSb$ superlattice structures still have very large (~10^{-6}A/cm^2 at 77K) dark currents in practice. This comes from generation-recombination current, when a impurity or defect level state is found in the forbidden energy gap this defect state can trap carriers, and allow them to recombine via a two stage non-radiative process [24] details of which can be found in chapter 2. This is referred to as Shockley-Read-Hall (SRH) recombination and is usually only found under very low injection. This is the case for photo-detectors however, and is found to be the dominant recombination process in InAs/$Ga_{1-x}In_xSb$ superlattice structures causing the large dark current values [15, 25].

These large dark currents have been shown to be a function of the minority carrier lifetime [26] with longer carrier lifetimes reducing the dark current values. Minority carrier lifetimes have been reported to be between 50-80ns [27, 28] for the InAs/$Ga_{1-x}In_xSb$ superlattice structures compared to 1μs [25] for $Hg_{1-x}Cd_xTe$. Another superlattice alternative to $Hg_{1-x}Cd_xTe$ has been suggested in the form of InAs/$InAs_{1-x}Sb_x$ superlattices [29]. By comparison of the minority carrier lifetimes in bulk InAs (325ns) [30] and $InAs_{0.8}Sb_{0.2}$ (250ns) [27] with GaAs (100ns) [30], it is thought the SRH recombination centre is caused by the addition of Ga. If this is the case, these InAs/ $InAs_{1-x}Sb_x$ superlattices are predicted to have a longer minority carrier lifetime and therefore reduced dark

current. The minority carrier lifetime in these superlattices has recently been measured to be 412ns [31] and places $InAs/InAs_{1-x}Sb_x$ an order of magnitude better than $InAs/Ga_{1-x}In_xSb$, yet still an order of magnitude worse than $Hg_{1-x}Cd_xTe$.

Against the other parameters outlined to make a good photo-detector, the $InAs/InAs_{1-x}Sb_x$ superlattice is also well suited though studied in far less detail than previous materials. The band gap is engineered in the same way as the $InAs/Ga_{1-x}In_xSb$ superlattice using a combination of layer thickness and alloy composition to determine the wavelength. The wavelength range of these superlattice structures is still being extended, with the documented range being 5μm to 10μm in 2009 [32] and the current generation of samples having a range of 4μm to 12.1μm in 2013 [33].

The optical absorption is found to be comparable to $Hg_{1-x}Cd_xTe$ detectors [34] though much work is still to be done as the temperature affects the photo-response significantly. An example of the temperature dependent spectral response is shown in figure 10 when under two different applied bias voltage. Increasing the bias voltage increases the SNR of the signal and allows for higher temperature measurements at higher bias. This figure shows that although these devices are promising alternatives to available photo-detectors they are still in development.

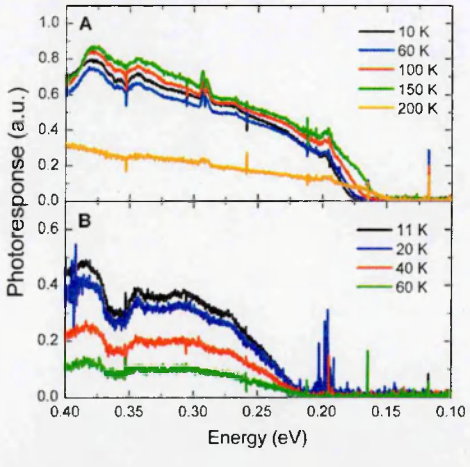

Figure 10: The temperature dependent spectral response for two $InAs/Ga_{1-x}In_xSb$ superlattice structures. Adapted from [34].

With InSb having the largest lattice parameter available of the conventional III-V materials the choice of growth substrate is limited. Referring again to figure 4, as was the case for InAs/$Ga_{1-x}In_xSb$ superlattices the only viable substrate currently is GaSb. Using another material introduces a large amount of lattice mis-match and introduces strain and dislocations into the sample increasing SRH recombination and hence the dark current.

5.2 Experimental Aim

The aim of this work was to experimentally confirm whether the defect level within the $InAs_{1-x}Sb_x$ superlattice is located above the conduction band edge [35], and attempt to measure its relative position.

The experiment will be performed by applying high pressures to the superlattice using a sapphire ball cell at low (10K) temperature. The applied pressure will increase the energy of the conduction band and primary energy transition until this energy state begins to overlap with the defect state. It should be noted that there will be a small change in the valence band position, but nearly all of the change due to pressure will occur in the conduction band due to its higher deformation potential. At the point where the energy transition and defect state begin to overlap carriers should recombine via the defect state, resulting in a decline in the observed PL from the sample.

Identifying the position of this level above the conduction band edge will show that SRH recombination *within* the forbidden energy gap will not be a dominant factor in producing dark current, as it the case for InAs/$Ga_{1-x}In_xSb$, thus increasing the suitability of InAs/ $InAs_{1-x}Sb_x$ as a photo-detector material.

Intrinsic surface states within the semiconductor materials used are thought to be the cause of the SRH recombination centres. These surface states have been calculated and measured for bulk materials [35]. Figure 11 shows for each material; the position of the valence band edge (hatched), the position of the

conduction band edge (dashed), the L_1 and X_1 band minima edges, the position of the surface state E_s and its measured energetic width, the position of the fermi level E_f, and also fermi level position of gold contacts E_0 in each case the zero energy is defined as the valence band edge. The data shows that the surface states lie within the forbidden band gap for GaSb, GaAs, and GaP, whereas the surface states for InAs and InSb are found within the conduction band. These calculations give strong evidence that the larger SRH recombination found in Ga containing superlattices is caused by a Ga related defect, and that the $InAs_{1-x}Sb_x$ superlattice should not suffer from the same problem. It should also be noted that the defect level state is calculated to be a broad energetic feature.

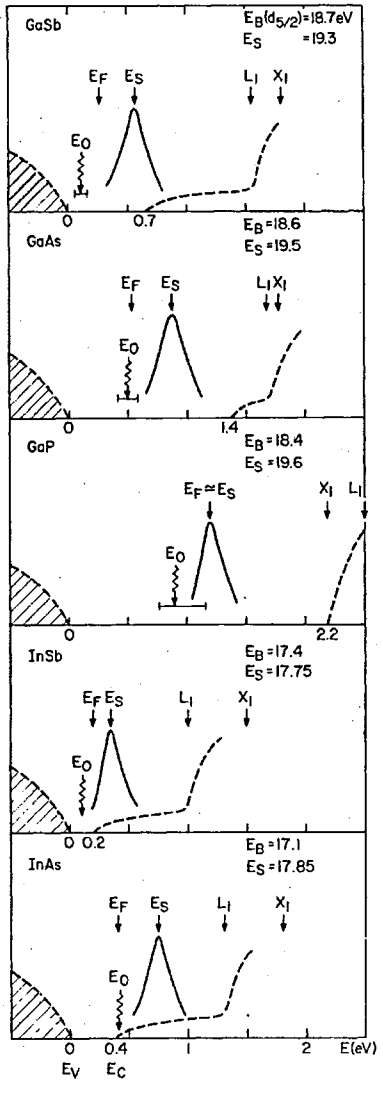

Figure 11: The calculated surface state positions for bulk III-V materials, adapted from reference [35].

When not working with bulk materials these surface states can help understand what is occurring at the interface states. Interface states arise from the point defects caused by lattice mismatch between the two materials. With increasing lattice mismatch in the material the density of interface states is increased, figure 12 shows this effect by the reduction of PL intensity with increasing Sb content within bulk GaSb/$InAs_{1-x}Sb_x$. Within InSb the interface states lie at the conduction band edge, so increasing the number of defects therefore the number of interface states will allow for a greater chance of non-radiative recombination at an interface state, rather than radiative band to band recombination.

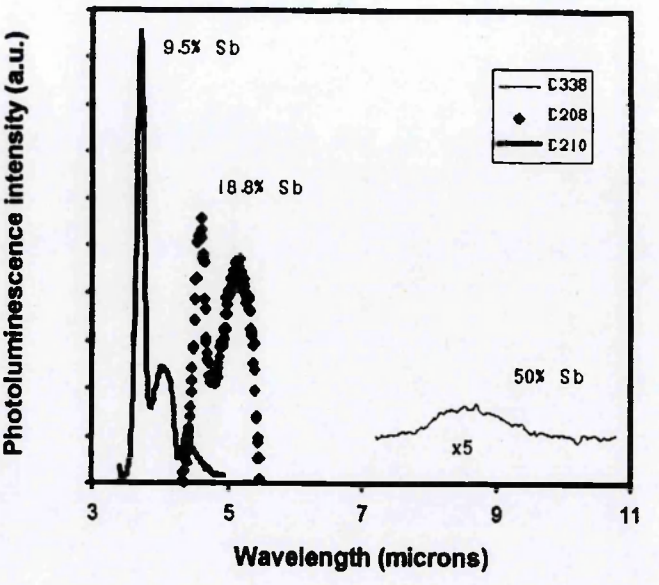

Figure 12: reduced PL with increasing Sb content. Adapted from [36].

While these calculations and measurements have been performed for bulk semiconductor materials, because of the complex de-localisation of the electrons and holes in this type of type-II superlattice forming an electron mini-band, calculation of the defect level and energy band overlap is difficult, simulations are performed later which show the change due to pressure with no observable defect state. This effect should be observable however by performing high pressure measurements. The effect of pressure on a semiconductor band structure has been discussed earlier in chapter 2, and using the sapphire ball technique outlined in chapter 3 high hydrostatic pressure can be applied at low temperature. It has been documented previously that pressure can be used to find electron traps by moving the band edge minimum relative to the defect [37]; and a similar method shall be employed here.

The band curvature in a semiconductor is quantified through the effective mass of the electron or hole. The heavy-hole mass ($0.43m_0$ InAs, $0.41m_0$ InSb)[38, 39] for these materials is also much larger than the conduction band elections mass ($0.014m_0$ InAs, $0.023m_0$ InSb)[38, 39] this gives band deformation values for the conduction band which are larger than that of the valence band. The deformation potential values for InAs are 1.00 eV/cm^3 [40] for the valence band and -5.08

eV/cm^3 [40] for the conduction band (these are relative terms and the negative sign represents an increase in energy), while the values for InSb are 0.36 eV/cm^3 [40] for the valence band and -6.17 eV/cm^3 [40] for the conduction band. This means when hydrostatic pressure is applied 84% of the energy change occurs in the conduction band for InAs, and 94% of the energy change due to pressure occurs in the conduction band of InSb. Due to the localisation of electrons in the InAs layer the pressure is predicted to shift with approximately the same rate as bulk InAs ie 12.5meV/kbar [41]. This means the electron mini-band in the superlattice should move to higher energy at the same rate with increasing pressure.

Since the defect level is above the conduction band edge and the electron mini-band moves to higher energy with pressure the states will increasingly overlap. By measuring at constant pump power, the measured PL intensity should decrease with increasing pressure as recombination increases with the electron trap reducing the radiative efficiency. This overlap with defect states is also expected to have a smooth onset based upon the data in figure 11, where broad edged surface states are evident. The thermal distribution of carriers will also facilitate a smooth onset. Also while the electrons are confined to the InAs layer of the superlattice, InSb features may be seen as the electron mini-band also overlaps with them. However as both InAs and InSb are predicted to have the defect state immediately above the conduction band edge they may not be distinguishable from one another.

5.2.1 Sample Modelling

The sample used for the experiments (selection details of which can be found below) was modelled using Nextnano Mat. Software [42]. This was done to firstly see the band alignment when at zero pressure, and secondly to model the behaviour of this band alignment when subjected to pressure.

Figure 13 shows a section of the simulated superlattice band diagram for a 8.1nm InAs, 2.4nm $InAs_{0.858}Sb_{0.142}$ superlattice which has 40 layers under 0kbar

pressure, and a temperature of 10K. The eigenvalue for the conduction band band and heavy hole wavefunctions are shown and represent the ground state transition for the semiconductor. It should be noted that although there is overlap between the heavy and light hole states, the calculated light hole wavefunction and corresponding eigenvalue are found at a lower energy than the heavy hole eigenvalue. This means they are not the lowest energy transition in the semiconductor. The calculated conduction band to heavy hole energy transition is calculated to be 322meV which is comparable to the measured peak energy of the sample discussed later (314meV).

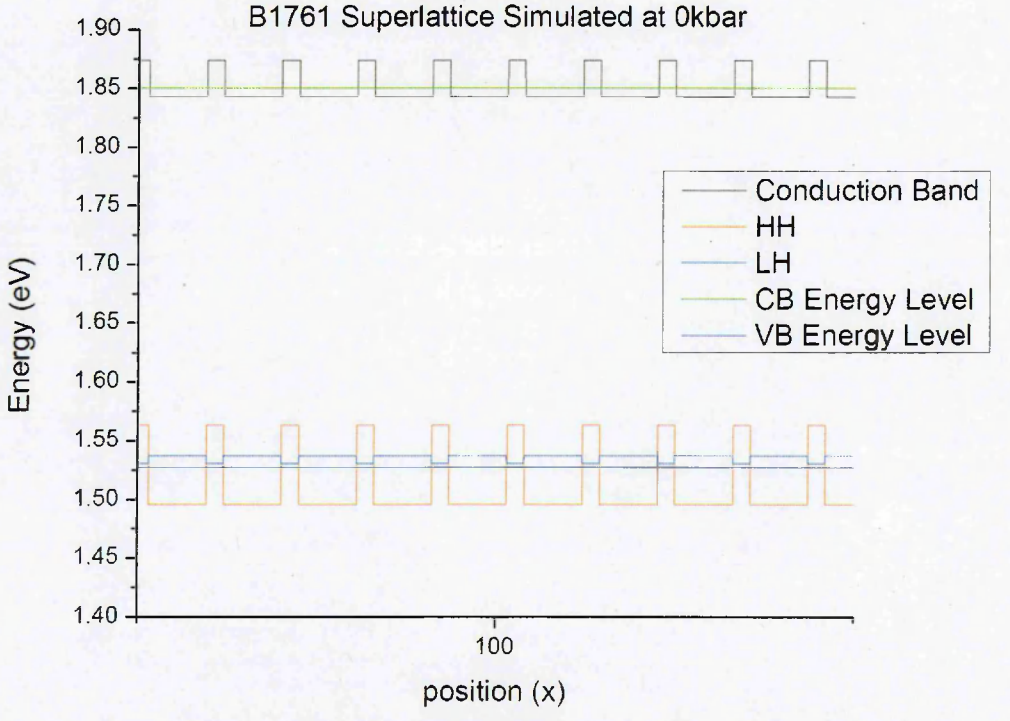

Figure 13: The simulated band alignment of sample B1761, calculated using the Nextnano software.

With an accurate starting position at 0kbar, the simulation was then modified to account for the effect of increasing pressure on the material bandgap. This was achieved by altering the fundamental material parameters for each of the binary materials involved in the semiconductor, in this case InAs and InSb. Two independent simulations were performed, in the first the binary materials bandgap was changed according to the following pressure equations [43, 44]:

InAs $$E_g = E_g(0) + 12.5e^{-3}P\ (eV)$$

InSb $$E_g = E_g(0) + 13.7e^{-3}P - 3.6e^{-5}P^2\ (eV)$$

Secondly the material bandgap and effective mass of the electron was changed with pressure, according to the following relation [45, 46]:

$$\frac{dm^*}{dP} = \frac{m^*}{E_g}\frac{dE_g}{dP}$$

Where m* is the effective mass, E_g is the bandgap of the material and P is the Pressure. The calculated energy gap resulting from these pressure simulations is shown in figure 14. The figure shows that the superlattice has a bandgap change of 12.93±0.04meV/kbar. This is unsurprising as most III-V materials have a change of 10-12meV/kbar, and the sample alloy is predominantly InAs, therefore should follow the pressure coefficient of this material closely.

It can also be seen that the effective mass of the electron makes little difference

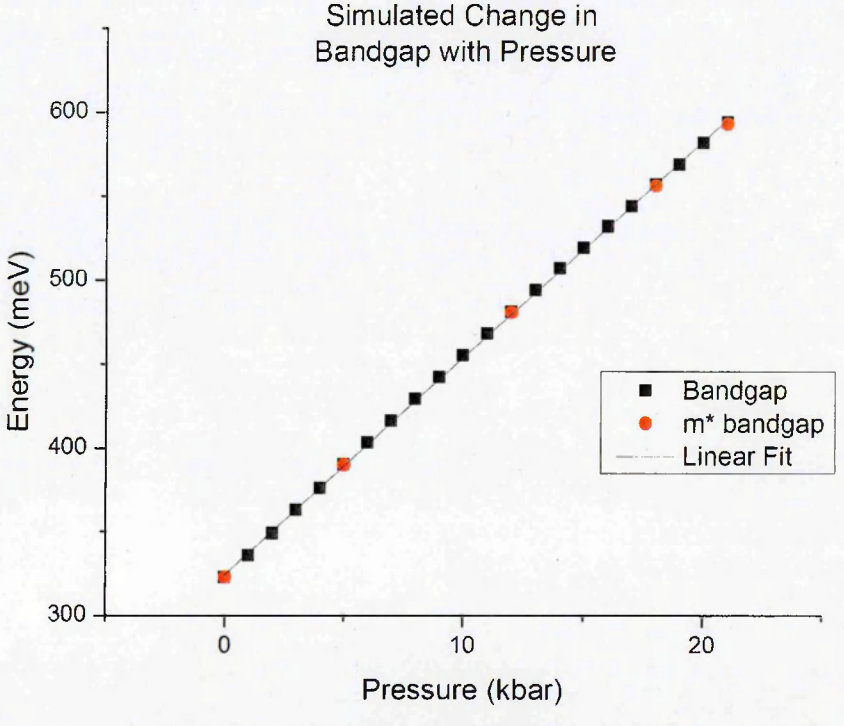

Figure 14: The simulated pressure coefficient of sample B1761.

to the calculated transition energy of the superlattice. Even at the highest pressure of 21kbar the difference is less than 1meV. This effect can be explained when the superlattice layer widths are considered. In this sample the InAs with is 8.1nm and the InAsSb width is 2.4nm, as the effective mass is an approximation of the curvature of the band, it will have less effect on the wider InAs layers. As the electrons in this superlattice are confined to the InAs layers then the reduced effect on the bandgap from the electron effective mass can be expected.

Finally, from these pressure simulations the expected change in band alignment and energy gap has been plotted and can be seen in figure 15. This shows that the expected shift in conduction band energy level is ~271meV when transitioning from 0 to 21kbar. It is expected that the conduction band energy level will begin to cross the predicted defect level leading to a decline in the measured intensity. This simulation does not include any change in the valence band due to pressure. This is because of very small deformation potential of the valence band resulting in a change of ~6% in its energy.

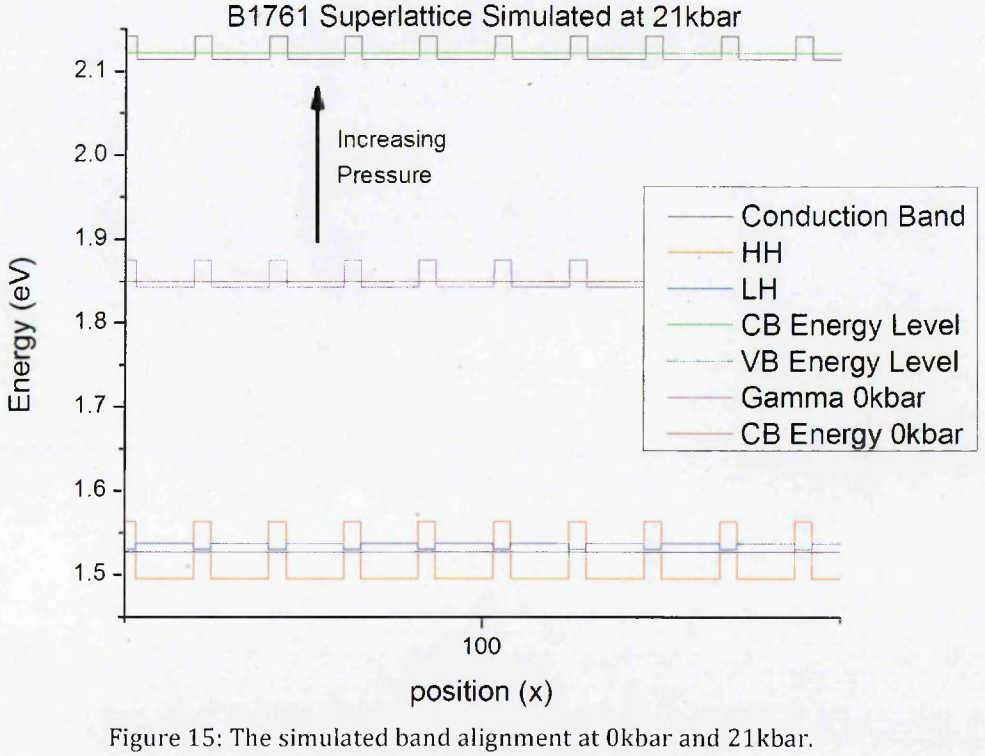

Figure 15: The simulated band alignment at 0kbar and 21kbar.

5.2.1 Experimental Sample Selection and Details

The InAs/$InAs_{1-x}Sb_x$ superlattice samples were provided by collaborators from Arizona State University, who are developing and testing new superlattice structures for use as photo-detectors. The samples provided have a peak emission wavelength of between 4μm and 12.1μm [33], achieving these wavelengths with layer thicknesses and alloy compositions as shown in table 2. The peak emission wavelengths were measured at 12K.

Sample #	InAs thickness (nm)	$InAs_{1-x}Sb_x$ thickness (nm)	x	λ_p (μm)
1 (B1761)	8.1	2.4	0.142	4.0
2 (B1789)	4.7	1.4	0.459	5.5
3 (B1774)	9.3	2.7	0.362	7.4
4 (B1769)	8.3	2.6	0.336	7.5
5 (B1772)	8.5	2.5	0.378	7.8
6 (B1776)	18.8	5.5	0.309	9.5
7 (B1775)	15.4	4.5	0.351	9.8
8 (B1778)	18.9	5.5	0.363	12.1

Table 2: The InAs/InAsSb superlattice structures grown at ASU. Adapted from [33]

To select a sample for the high pressure measurements in the sapphire ball, considerations for the equipment being used were needed. The equipment details were outlined in chapter 3. One of the limitations on sample selection was the cryostat quartz window transmission spectrum. The sharp cut off in transmission at 4.5μm meant that only sample 1 (B1761) was suitable for measurement in the system. Consideration was given to sample 2 (B1789), as this could be shifted into a measureable wavelength by applying ~4kbar of pressure assuming a pressure coefficient of 12.5meV/kbar. However, as the exact position of the defect state was not known, then it potentially could have been missed if starting at a non-zero pressure therefore sample B1761 was chosen for measurement and B1789 left for possible future work.

As the superlattice band gap is shifted to shorter wavelength by using pressure the maximum and minimum measurable wavelengths were calculated. The

maximum wavelength is given by the peak emission wavelength already measured i.e. 4μm. The maximum energy is obtained by taking the sapphire ball cells maximum pressure and multiplying it by the assumed pressure coefficient of 12.5 meV/kbar, assuming a linear relationship. Using the following relation the maximum wavelength can be calculated calculated:

$$\lambda = \frac{hc}{\left(E + \frac{dE}{dP}P\right)}$$

It should be noted that although sapphire ball cells have been documented to reach pressures of ~72kbar [47] the pressure reached on the sapphire ball cell at Surrey University works reliably to 30kbar owing to the larger gasket size. This results in a wavelength range of 4μm to 1.8μm for sample B1761 with increasing pressure up to 30kbar.

5.2.1.1 Pressure Limitation of the Sapphire Ball Cell

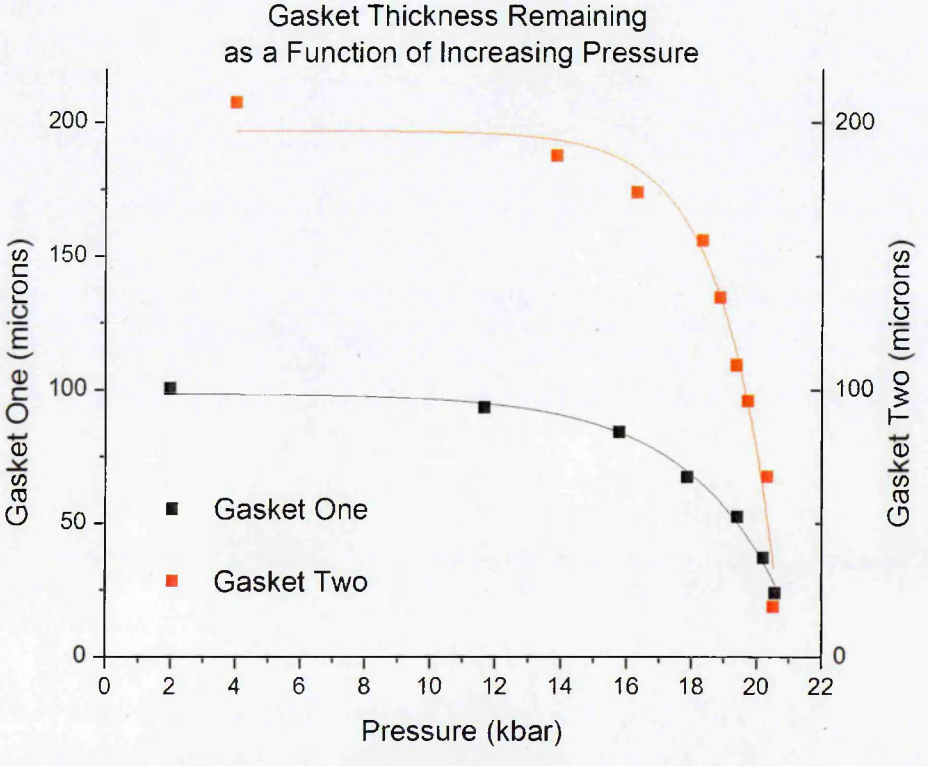

Figure 16: The remaining gasket thickness with increasing pressure.

While it was stated that the sapphire ball cell has reliably reached pressures of up to 30kbar previously, during this experiment the maximum pressure obtained was ~21kbar. The absolute maximum pressure attainable by the sapphire ball is determined by the pressure at which the sapphire lenses will crack relieving the internal pressure, in practice this pressure is never reached due to other mechanical limitations within the cell. The maximum pressure in any given experiment is determined by the point at which the rolled steel gasket is deformed sufficiently so that the samples mounted inside the cell would be crushed between the two sapphire lenses.

Figure 16 shows the remaining gasket thickness as a function of pressure, gasket one was used for three experimental runs, while gasket two was used for a single experiential run. As mentioned in chapter 3 the samples in this experiment were stacked making them ~160μm thick, and the total gasket space was 450μm, this leaves 290μm of height available deformation due to pressure before the samples are crushed by the sapphires. The space remaining in the gasket is observed to decline with pressure tending towards a limiting maximum pressure of ~21kbar for both gaskets.

5.2.1.2 Apparatus Transmission

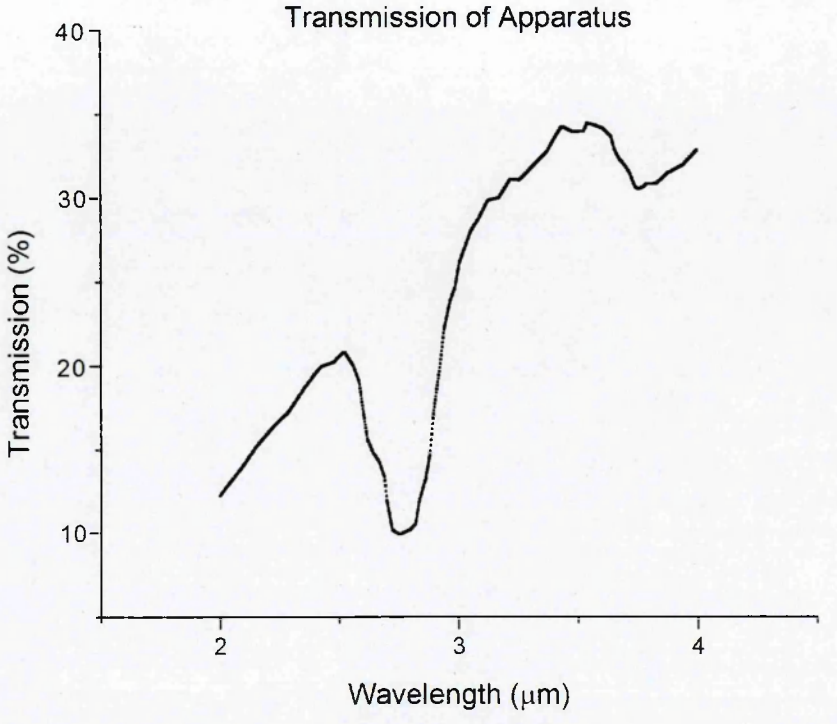

Figure 17: Calculated transmission of apparatus, based upon the transmission spectrum of the Triax grating, blue InSb detector, quartz cryostat window, two CaF_2 lenses and Sapphire discussed in chapter 3.

A comparison between integrated PL intensity as a function of pressure is required to determine if the measured intensity is in fact decreasing with pressure due to defects. The transmission window was determined using the transmission factor of each component of the apparatus used for the experiment. In this case the transmission considered was Triax grating number 2, the "blue" InSb detector, the quartz cryostat window, two calcium fluoride lenses and the sapphire ball. Details of these pieces of equipment are discussed in chapter 3. The results of the calculation are shown in figure 17. This calculation ignores the effect of reflection from the surfaces being passed through and atmospheric absorption, but clearly shows that with increasing the pressure the system response itself will cause a large drop in intensity. This decrease is chiefly due to the Triax 320s grating having a poor response in the 2μm-4μm region. However, these features including the atmospheric absorption should be normalised out of the final spectra as discussed in chapter 3.

5.3 Results

5.3.1 Atmospheric Pressure PL

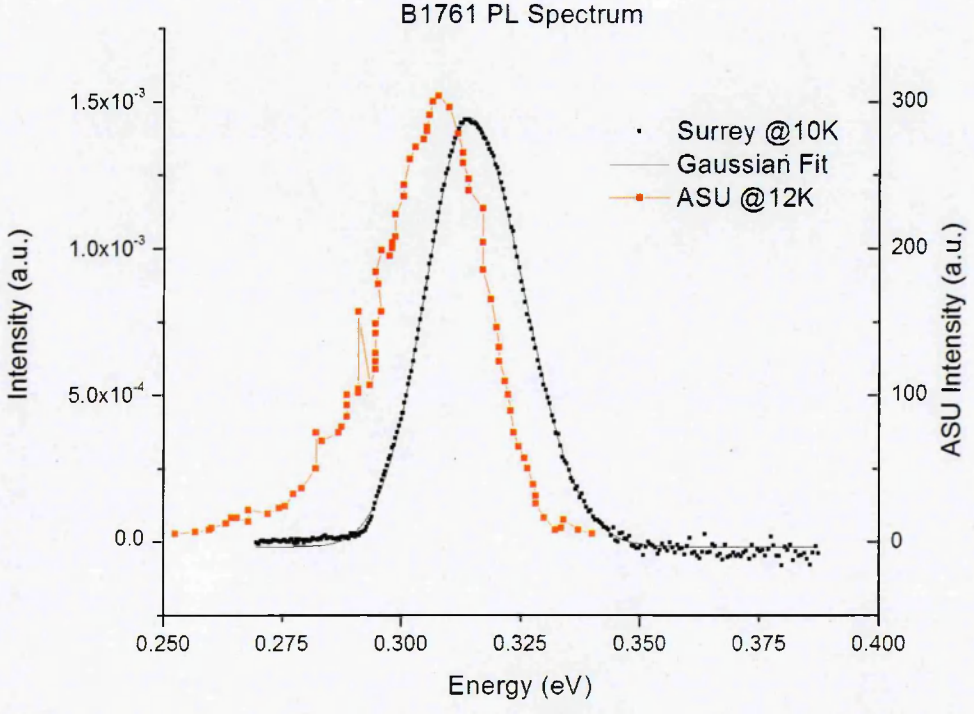

Figure 18: The 10K PL Spectrum of the $InAs/InAs_{0.858}Sb_{0.142}$ superlattice, fitted with a bi-Gaussian curve.

The first measurement performed on the sample were 10K PL measurements performed on a large piece of the sample before placing it inside the sapphire ball cell. Though 12K PL measurements had been previously been performed by colleagues at ASU [33], their measurements were performed using a different experimental setup, including an MCT photo-detector. With this sample having the shortest emission wavelength this was at the edge of the MCT's operational range and therefore produced a noisy spectrum [33] as can be seen in figure 18. The InSb photo-detector used for the measurements in this thesis has a peak responsivity from 4μm to 5μm. This measured a spectrum with little noise using a 100mW 808nm pump laser at 10K as is shown in figure 18 as compared with the ASU spectrum also shown. The shift in emission peak energy is thought to be the result of sample heating due to the high laser power used during the ASU measurements.

The emission peak is fitted with a Originlabs built in bi-gaussian function. This fits each side of the peak position x_c with a half Gaussian distribution. Physically this represents the Urbach tail for the energies below the band gap and radiative transitions for the energies above the band gap this is further discussed in chapter 2. The equation for fitting function is given by [48]:

$$L = L_0 + Aexp\left[-0.5\left(\frac{E - E_c}{\Delta E_1}\right)^2\right] \qquad (E < E_c)$$

$$L = L_0 + Aexp\left[-0.5\left(\frac{E - E_c}{\Delta E_2}\right)^2\right] \qquad (E > E_c)$$

Where L_0 is the background noise level, A is the Gaussian amplitude, E_c is the peak position and ΔE_1 and ΔE_2 are the Gaussian widths. The peak position is measured to be 3.95μm (314meV) at 10K which is comparable to the previous measurements at ASU of 4μm [33]. This data also tells us about the maximum signal that can be expected from the sample. Once cleaved so that is of an appropriate size to fit inside the sapphire ball cell, a less intense PL emission can be expected owing to the limited area available for excitation.

5.3.2 Temperature Dependent PL

As previous generations of InAs/$InAs_{0.858}Sb_{0.142}$ superlattice have a poor maximum operating temperature, and a large temperature dependent response [34] the temperature dependence of this new generation sample was measured. The large piece of sample was excited outside of the sapphire ball cell with a 100mW, 808nm pump laser and the temperature increased in increments of 10K, with a starting temperature of 10K, the experimental results are shown in figure 19 where the maximum temperature a PL signal was detected was 120K.

The temperature dependent measurements firstly show that there is a decrease in the PL intensity with increasing temperature. The effect happens quickly with temperature and is likely an effect of increased tunnelling losses compared to the Ga containing superlattice structures [49]. The $InAs_{1-x}Sb_x$ superlattice structures have decreased conduction and valence band offsets compared to Ga superlattices as can be seen from the simulation earlier, and the increasing temperature increases the carrier energy resulting increased carrier loss through tunnelling or thermal leakage.

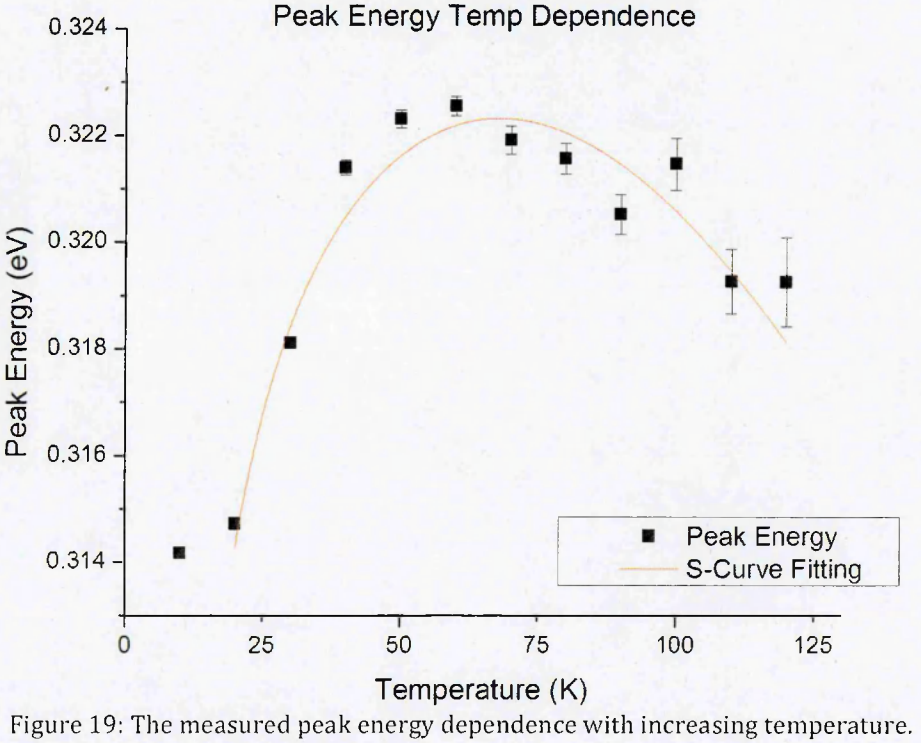

Figure 19: The measured peak energy dependence with increasing temperature.

The peak energy temperature dependence is seen to have a sharp blue-shift with temperature, and then a slow onset red-shift. This "S" curve fitting has been well documented in quantum well materials [50], and has also been observed in $GaN/Al_{0.2}Ga_{0.8}N$ superlattices [51, 52]. This temperature dependent line shape is caused by localised states, caused by disorder at the interface boundary. These localised states can then be described as carriers localised in high energy states. At the semiconductor is heated these carrier gain thermal energy allowing occupy higher energy positions in the density of states until normal band filling occurs and a red-shifting behaviour is resumed. In this case the normal red-

shifting behaviour begins again at 60K. The peak energy data is fitted using [51, 52]:

$$E(T) = E(0) - \frac{2\alpha}{e^{\Theta/T}-1} - \frac{\sigma^2}{k_B T}$$

Where E(0) is the transition energy at zero Kelvin, α is the strength of the electron-phonon interaction, Θ is related to the average phonon energy, and σ is the dispersion of the density of states (its width). The following parameters were gained from this fit; α = 0.047meV, Θ = 328.6K, and σ = 4.6meV. With σ being very small compared to the superlattice emission energy this indicates a high quality of the superlattice interfaces [52]. This S-curve also explains why the initial energy value of the simulation was 322meV, as the simulation would not have accounted for surface states, the limits of the simulation make it follow a strict Varshni behaviour to model temperature change.

It should be noted at this point that the pressure dependent measurements presented in this work were all performed at 10K to gain the maximum PL signal. This means the measurements were performed in the 'S' region, while some carriers were trapped in localised states. It is noted in a future section that the PL intensity appears to increase in intensity with increasing pressure. This could be the result of carriers being liberated from these localised states with increasing pressure, resulting in more carriers available to recombine radiatively. However, these localised states do not explain the sudden drop in measured intensity at high pressure, and therefore do not alter the conclusions drawn about the position of the defect state from this work.

5.3.3 Preliminary Pressure Dependent Spectra

For pressure measurements, the superlattice sample was cleaved and thinned to 80μm and mounted inside the sapphire ball cell, along with the $In_{0.73}Ga_{0.27}As_{0.89}P_{0.11}$ mid-IR pressure gauge described in chapter 3. The bolts were tightened to the smallest possible amount that would allow the two halves of the cell to stay together. The sample spectra was now measured at this lowest

possible pressure for comparison against the original large sample size measurement, the results of which are shown in figure 20.

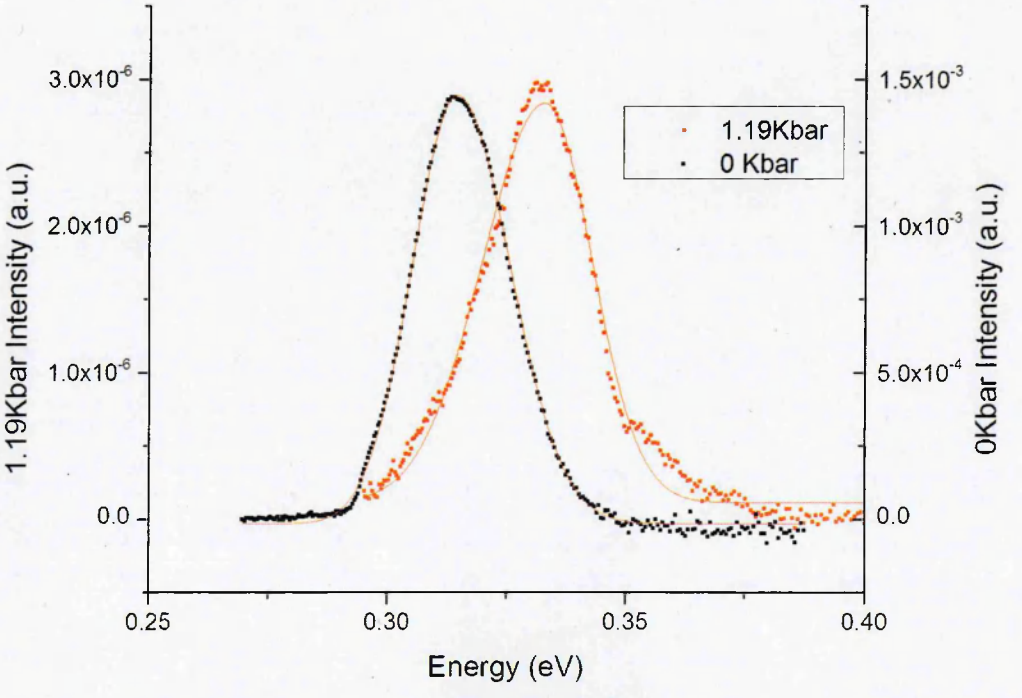

Figure 20: A comparison of the PL spectra obtained from the original large piece measured outside the sapphire ball cell, and the cleaved thinned piece measured at the lowest pressure obtainable by the sapphire ball cell.

The spectra shown in figure 20, has a shifted peak emission due to the increased pressure within the sapphire ball cell. The 0kbar peak is measured to be at 314meV with a FWHM of 10meV, the 1.19kbar peak is measured to be 333meV with a FWHM of 11meV. This implies that the peak shape has not changed with increasing pressure and the pressure dependent shift of the sample is 16meV/kbar. The only large change between the spectra is the measured peak intensity. This has dropped three orders of magnitude. As the peak energies are similar, this cannot be put down to the wavelength dependent transmission of the apparatus, and instead is probably caused by the decreased sample size as well as the flat 10% reduction in transmission that comes from passing through a sapphire ball. Previously on the bulk sample the excitation area was the same as the spot size, inside the sapphire ball the area being excited by the laser is substantially smaller resulting in a less intense total output. Satisfied that

mounting in the sapphire ball cell has not changed the spectrum in any other way than decreased intensity and a peak energy shift due to pressure, additional measurements were performed while increasing the pressure. These pressure dependent results are shown in figure 21.

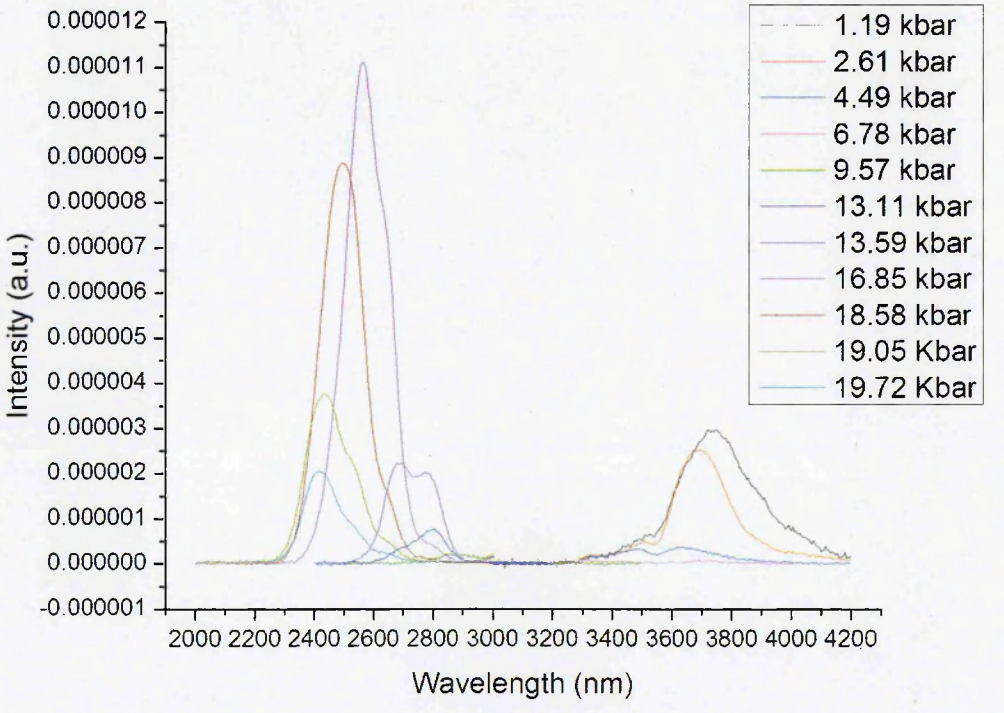

Figure 21: The as measured PL intensity with increasing pressure.

Though not normalised, and as such features of the apparatus and atmosphere will be visible, figure 21 clearly shows the wavelength blue-shift caused by increasing pressure on the superlattice. This is confirmation that the electron min-band is moving up in energy through the structure. There three interesting features of this plot that were investigated further: (1) There is a large wavelength range that has poor PL intensity between 2800nm and 3600nm, (2) There is a sharp drop off in intensity at the highest pressures, and (3) there appears to be variation in measured PL intensity between the lowest pressure, and just before the high pressure drop-off point. While the high pressure drop-off in intensity was an expected feature of finding the InAs defect level above the conduction band, the other two features require explanation to justify that the defect level has in fact been found.

5.3.3.1 Alcohol absorption

While the calculated transmission change with wavelength was calculated in figure 17 it does not reflect the large region of poor PL intensity as shown in figure 21. This drop in PL intensity was found to be caused by the methanol/ethanol pressure medium used in the sapphire ball cell. As liquid is not usually part of a mid-IR optical PL experiment this was overlooked. Upon further investigation, it was found that all of the alcohols have absorption features in the mid-IR due to their O-H bonds [53, 54].

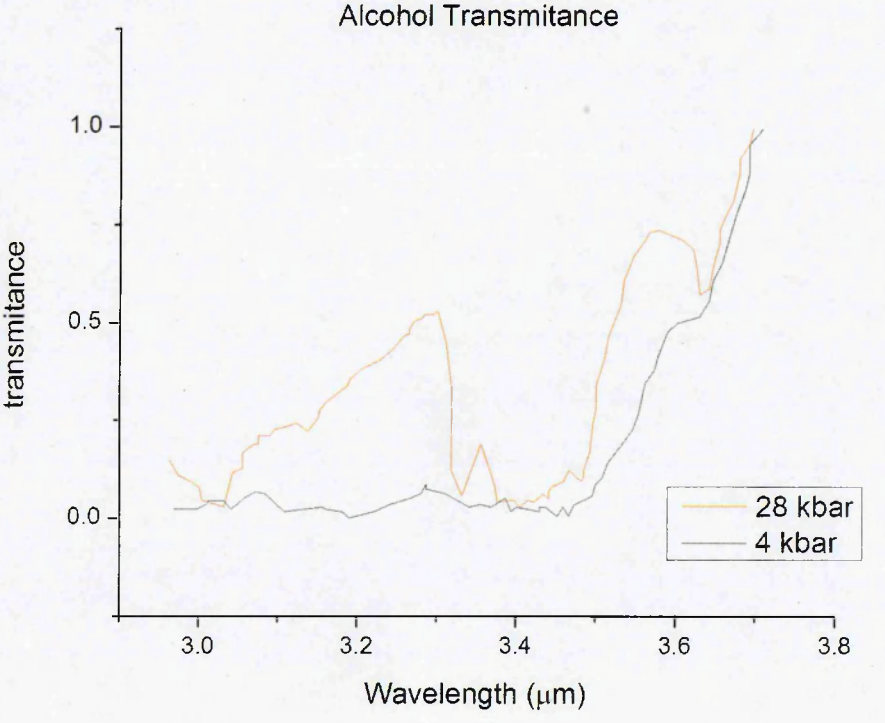

Figure 22: The changing transmittance of ethanol with pressure at 4kbar and 28kbar. Adapted from [55].

While such a feature would normally be removed by normalisation, this is not the case when using alcohols. The transmission spectrum of methanol and ethanol is changed by temperature as the liquid freezes, and also has a pressure dependence [54, 55]. An example of this changing transmission is shown in figure 27. This double dependency on the experimental parameters would now

require the pressure and temperature of each measurement to me matched, and a system response spectrum taken to match each PL measurement. This however is difficult with the sapphire ball cell, due to reaching the exact same pressure. This data could be approximated by an interpolation of figure 22, however, it will be shows that the region affected by alcohol absorption does not impact the final results, and so this interpolation was not performed. Furthermore to measure the system response spectrum while the sample is mounted is not possible as the gasket space is completely filled due to the stacked mounting method outlined in chapter 3.

There are other materials available to use as a pressure medium, such as helium or argon gas that would eliminate this problem [47]. However, they make the sapphire ball cell much more difficult to load and use. This goes against the premise of the device as a mobile easy to use high-pressure device. This alcohol absorption explains the large depression in the PL signal seen in figure 21, and stops us drawing any conclusions about the superlattices behaviour there. Fortunately the alcohol absorption window is spectrally localised, and the defect level energy is located outside of it.

5.3.3.2 Optical Collection Issues

While it has been shown that there is a normalisation issue caused by the changing absorption features of the alcohol pressure medium, it must be justified that the changes in intensity are not caused by optical collection issues. This can be done by performing the same integrated intensity analysis for the $In_{0.73}Ga_{0.27}As_{0.89}P_{0.11}$ pressure gauge. This sample has a known pressure coefficient, and does not change its light output with pressure substantially over the pressure range studied. The emission wavelength range is also not affected by the alcohol absorption features found further into the mid-IR, and is also free of any atmospheric absorption features. This means any change in intensity is caused by problems in the optical collection efficiency. Small problems are to be expected, as the sapphire ball cell must be physically removed form the apparatus when adjusting the pressure. While every care is taken while

performing this process, small changes in the collection efficiency are unavoidable.

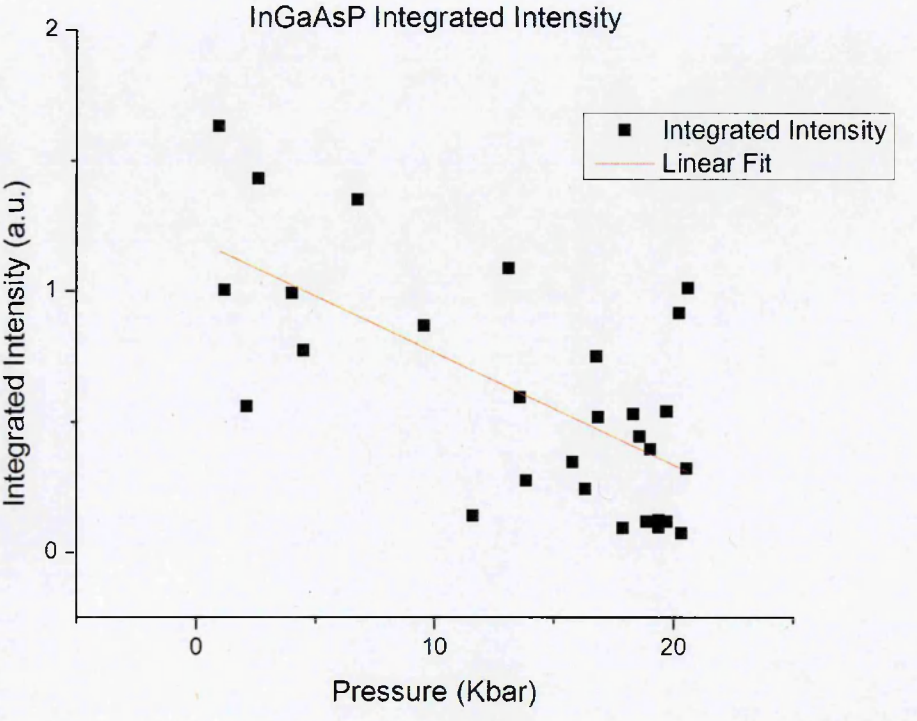

Figure 23: The integrated intensity of the InGaAsP pressure gauge, showing a slight linear dependence with pressure.

The measured integrated intensity of the InGaAsP pressure gauge is shown in figure 23. The figure shows considerable scatter between the data points with increasing pressure. There is also a weak linear dependence to the data with increasing pressure. This weak linear dependence is caused by the changing efficiency of the apparatus which was shown to have a linear decline in response with reducing wavelength (increasing pressure) in figure 17 and approximately the same loss factor as calculated of 66%. The scatter between data sets and data points is caused by a change in the optical collection efficiency changing. It can ba assumed that these changes in collection efficiency will also effect the other sample mounted n the sapphire ball cell, and will later be normalised out. This change in collection efficiency is unavoidable with the large disturbance to the apparatus when removing the sapphire ball cell. It should be noted that there is no resemblance to the shape of the data shown in figure 24 of the increasing

intensity and then sharp decline, this shows that these changes are not features of the optical collection efficiency.

5.3.4 Normalised Pressure Intensities

The pressure measurements were repeated four times. Data set 1 are the original measurements while increasing the pressure, 2 a repeated measurement moving down in pressure on the same gasket, 3 a repeated measurement while moving up in pressure again on the same gasket, and 4 is a repeated measurement moving up in pressure with a completely new gasket. This repeatability was tested on a new gasket to confirm the pressures calculated for each measurement were the same on a fresh gasket. This required a complete reload of the samples into the sapphire ball cell, and so previous gasket measurements would not influence it. The sapphires and gasket were replaced to show that any observed features were not a function any defects in the previous sapphire balls.

The measured spectra were then normalised and the integrated intensity under the curves calculated. Although the normalisation process is not perfect because of the alcohol absorption discussed earlier, this integrated intensity values give a measure of the total light output of the semiconductor, these normalised results are plotted in figure 24.

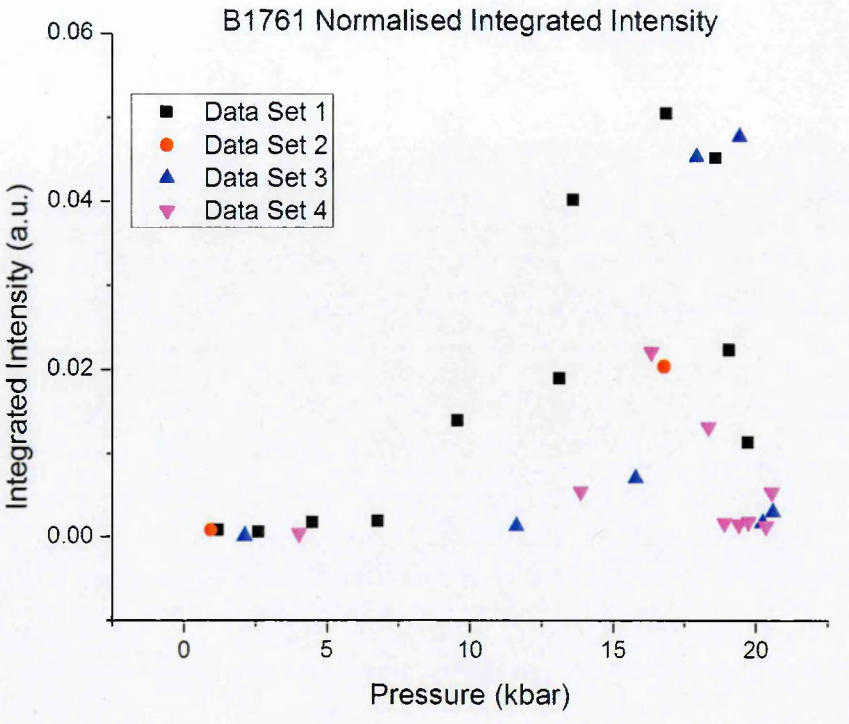

Figure 24: The normalised integrated intensity of the light output as a function of pressure.

Figure 24 shows that in all cases there appears to be an increase in the total light output with pressure, then a sharp decline at a critical pressure of 19.4kbar. It should be noted that the large amount of scatter between experiments is caused by the alcohol absorption not being properly removed through normalisation. This assumption can be justified by observing at the high and low pressure ends of the data where the alcohol absorption effect is least, also has the least amount of data scatter.

The critical pressure of 19.4kbar at which the pressure declines corresponds to a peak energy transition energy of 0.51eV. This value is in good agreement with the position of the high energy tail of the calculated value found in the literature for InAs [35], and this decline is therefore thought to be caused by the defect level state. The same literature also calculates that the defect level state is wide rather than a sharp feature of the material. Based upon this, it is reasonable to say that the carriers are lost from the radiative recombination process to defect level state when even a small pressure is applied. This means the pressure at

which the measured intensity declines to such a point that the SNR is very low, is the point at which the majority of carrier are recombining via the defect state rather than radiatively. This change in dominant recombination process with pressure can be simply checked by measuring the power dependence of the PL intensity at high and low pressure.

5.3.4.1 Normalising to the Pressure Gauge

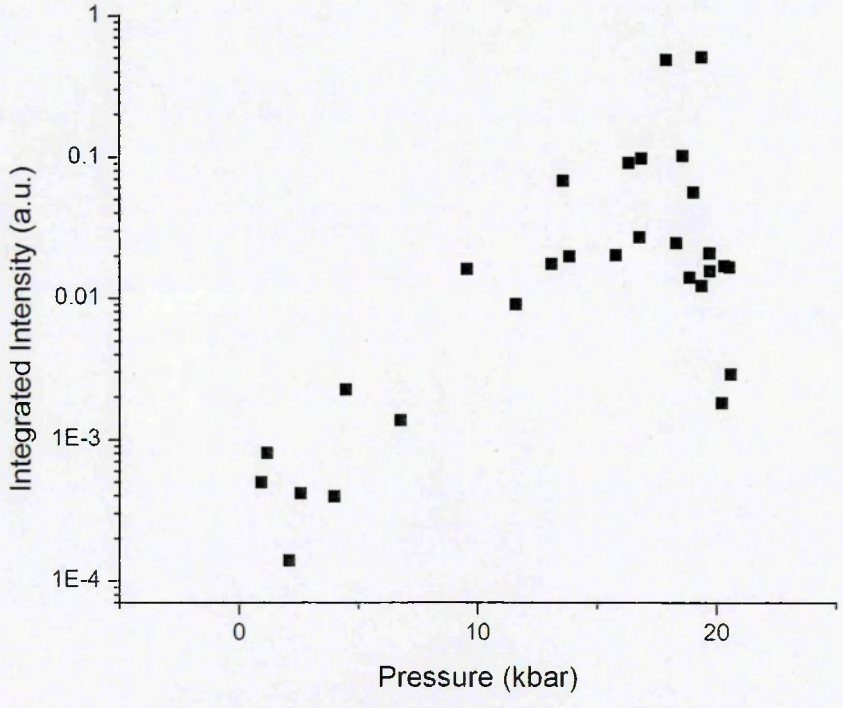

Figure 25: The measured integrated intensity of the superlattice structure, corrected for optical collection efficiency.

Further normalisation is performed to adjust for the optical collection efficiency. With a known change in the optical collection efficiency shown by the pressure gauge, it is possible to correct the measured integrated intensity of the superlattice sample by using the $In_{0.73}Ga_{0.27}As_{0.89}P_{0.11}$ pressure gauge. It can be assumed that the integrated intensity of the pressure gauge is linear with pressure over this pressure range, by multiplying each data point by a normalisation factor that will make it linear, these normalisation factors can then be applied to the corresponding superlattice samples data point to remove the

changes in optical collection. This can be done as each superlattice point always has a corresponding gauge point. These corrections have been applied and the resulting data is plotted in figure 25. This again illustrates the same information as that shown in figure 24, a rise in integrated intensity and then sharp decline.

5.3.5 PL Pump Power Dependencies

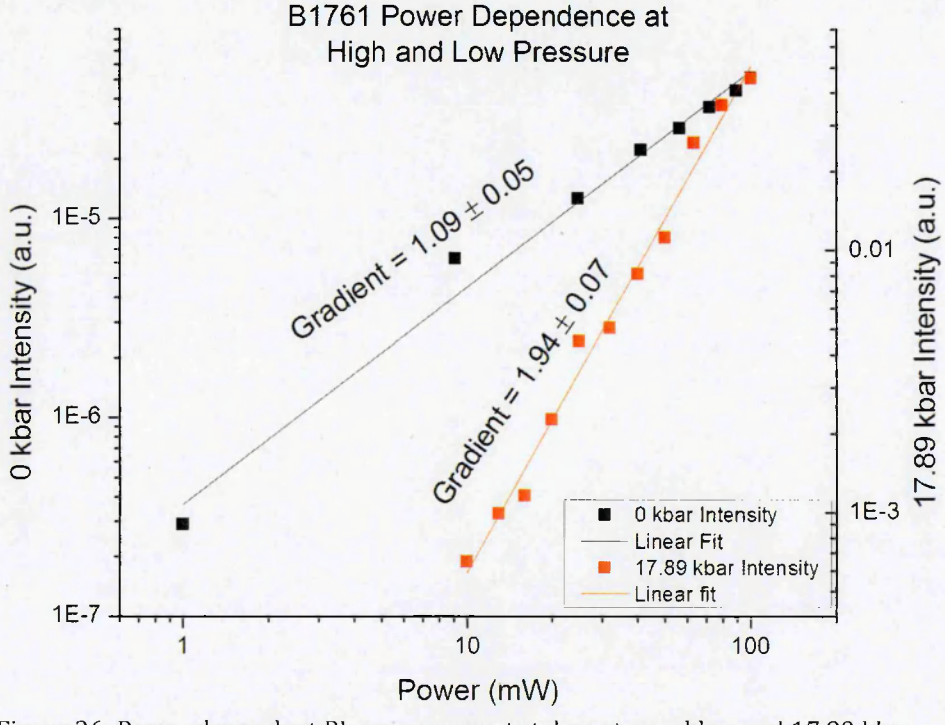

Figure 26: Power dependent PL measurements taken at zero kbar and 17.89 kbar.

Power dependent PL measurements of the sample were taken to identify the dominant recombination process within the sample, details of the theory behind this can be found in chapter two. Power dependent measurements were taken at pressures of 0kbar and 17.89 kbar. These values were selected as if the competing dominance theory stated above is correct then at 0kbar the dominant recombination process should be radiative as there is not yet any influence from the defect state, and at 17.89kbar strongly defect related as this is the point just before the observed PL intensity declines to a non-observable value and the sharp decline in intensity appears. Figure 26 shows that that when the sample is at 0kbar a measured gradient of 1.09 ± 0.05 is found from the Z-analysis in chapter 2 shows, this indicates a dominant radiative recombination process. At a

pressure of 17.89kbar the measured gradient is found to be 1.94 ± 0.07 indicating a dominant defect related recombination process.

This change in dominance matches the predicted behaviour due of a gradual overlap with the defect state positioned above the conduction band edge. This provides the first experimental confirmation that this above conduction defect state exists, and that InAs/InAsSb superlattice structures provide a better alternative to Ga based superlattice photo-detectors due to the limited dark current produced through SRH recombination in the forbidden band gap region.

While this experiment has provided confirmation that the defect level exists and is located ~200meV above the conduction band edge. The width of the level is yet to be ascertained. As the power dependent PL results performed at pressure values between 0kbar and 17.89kbar have interference from the alcohol absorption. This limits the measured output intensity, and therefore measuring a signal at reduced power becomes impossible due to the low SNR This lack of data means that the position at which the dominant recombination process begins to change from radiative to defect cannot be determined, and therefore the width of this defect related feature cannot yet be estimated.

5.3.4.1 Superlattice Pressure Co-efficient

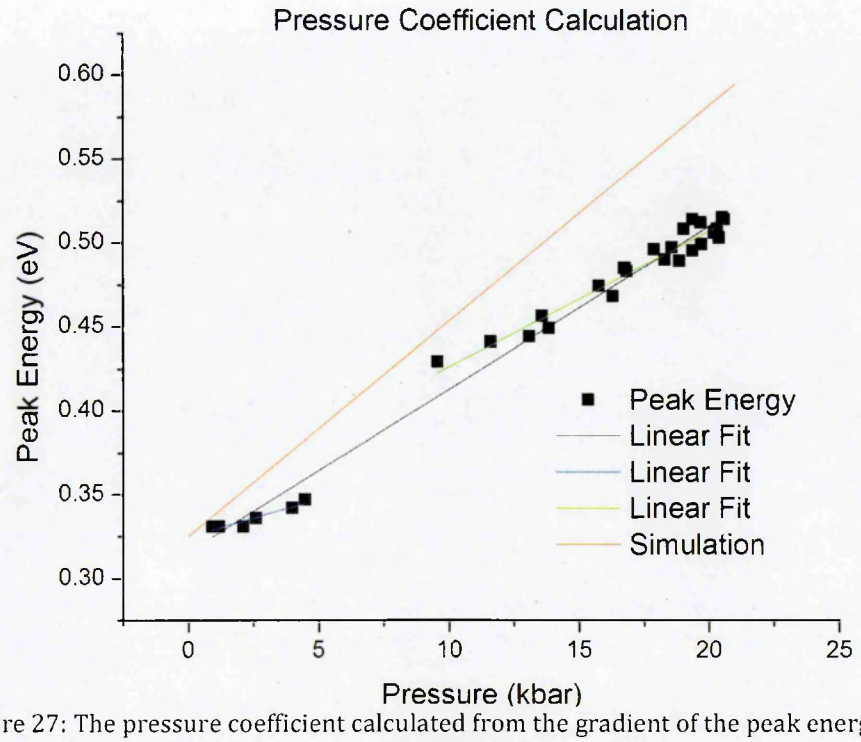

Figure 27: The pressure coefficient calculated from the gradient of the peak energy change with pressure, and simulation using Nextnano.

Though it was not the primary aim, from the data gathered from this experiment the pressure coefficient of the superlattice can be calculated. This is done by plotting the peak emission energy against the pressure at which it was measured with the gradient being the pressure co-effcient. This is shown in figure 27, and a pressure co-efficient of 9.7 ± 0.2meV/kbar is calculated (black).

There also seemed to be a discrepancy in gradient before and after the range over which alcohol normalisation was a problem. To test if alcohol was affecting the data the gradient was fitted over each of these shorter ranges giving values of 4.4 ± 0.7meV/kbar (blue) and 8.1 ± 0.4meV/kbar (green). The higher pressure values are known to not be affected by the alcohol absorption and the lower pressure values are on the edge of the known alcohol absorption. Also the higher pressure data is more numerous, based on this higher reliability is expected from the higher pressure data points.

The simulated data is also shown and has a significantly higher pressure coefficient of 12.9 ± 0.1meV/kbar (red). This can be attributed to the software using the dependence of InAs and InSb with literature values of 12.5 meV/kbar and 12.8 meV/kbar for bulk InAs and InSb respectively [41] as a baseline figure. From this it is not possible for the software to produce a value that will differ wildly from this. Also the way in which pressure has been calculated using the software accounts for any change due to pressure being in the conduction band, with no change in the valence band due to pressure modelled the simulated value will slightly overestimate the pressure coefficient.. Previous studies have shown that the pressure coefficients of InAs/$Ga_{1-x}In_xSb$ superlattices have a pressure dependence which is less than that of the bulk materials, and also have a small ~1-1.5meV/kbar valence band dependency on pressure [56]. From this information it can be expected that the software simulation will therefore over estimate the pressure dependence.

5.5 Conclusions and Further Work

Three key pieces of data were gathered about the superlattice were measured while performing these experiments: (1) the temperature dependence of the superlattice was measured and a low temperature blue-shift and subsequent higher temperature red shift was found. This is comparable to other superlattice structures such as GaN/$Al_{0.2}Ga_{0.8}N$ [51, 52]. This blue shift is caused by localised states at the superlattice layer boundries, and the same fitting was performed for this sample as that found in the literature to gain a value for the superlattice interface quality σ. With this value being very small (0.0046meV) compared to the superlattice emission energy (314meV) then the interfaces are thought to be of good quality.

(2) the pressure coefficient of the superlattice was calculated from the peak energy position change with pressure and was found to be smaller than both simulation or bulk InAs and InSb. This was found to be in line with the literature for this type of localised carrier superlattice.

(3) evidence was presented that the high-pressure decline in measured integrated intensity was caused by a defect level state being moved into the band gap using high pressure. Power dependent measurements showed a change to from radiative dominant recombination to defect related recombination as the pressure is increased. This implies that the radiative and defect processes come into competition as soon as pressure is applied, and at ~19.5kbar the defect related recombination is important.

Given the information obtained from this experiment there is some interesting further work that could be performed. Performing the experiment using a different pressure medium such as argon would eliminate the alcohol absorption features that were present in all of the spectra. This would definitively show that the measured increase in integrated intensity before the 19.4kbar critical point was a normalisation error rather than superlattice feature.

As discussed earlier, this 4μm emission wavelength sample was chosen as it was best suited to the apparatus. As it is expected now that the defect level state does not move with pressure, this could be confirmed by repeating the experiment using the 5.5μm sample but beginning the experiment at a pressure of ~4kbar so that the peak emission would be measureable using the available apparatus. Though this would miss some of the low pressure data points out, it should provide confirmation of the defect level being moved into the band gap with pressure and also its position, assuming it is immobile with pressure. The position could also be confirmed to be identical, showing it is in the InAs layer.

5.6 References

[1] Z. Yin et al., *"A review of energy bandgap engineering in III–V semiconductor alloys for mid-infrared laser applications"*, Solid-State Electron. 51, 1, 6-15 (2007)

[2] P. Norton, *"HgCeTd Infrared Detectors"*, OPTO-ELECTRONICS REVIEW 10(3), 159–174 (2002)

[3] G. E. Jellison et al., *"Optical Absorption of Silicon Between 1.6 and 4.7eV at Elevated Temperatures"*, Applied Physics Letters 41, 180 (1982)

[4] Y.P. Varshni, *"Temperature dependence of the energy gap in semiconductors"*, Physica 34, 1, 149–154, (1967)

[5] S. M. Sze, *"Modern Semiconductor Device Physics"*, Pages 409-466 (1998)

[6] A. R. Adams, "Band-structure engineering for low-threshold high-efficiency semiconductor lasers", Electronics Letters 22, 5, 249-250, (1986)

[7] HgCdTe (MCT) Detectors Technical Data and Information, Accessed Jan 2013, <www.irassociates.com>

[8] R. C. Jones, *"Proposal of the detectivity D* for detectors limited by radiation noise"*, Journal of the Optical Society of America 50, 1058, (1960)

[9] M. W. Scott, "Energy gap in $Hg_{1-x}Cd_xTe$ by optical absorption", Journal of Applied Physics 40, 4077, (1969)

[10] O. Caporaletti et al., *'The low - temperature thermal expansion of $Hg_{1-x}Cd_xTe$ alloys"*, Applied Physics Letters 39, 338 (1981)

[11] U. Rössler, *"New Data and Updates for I-VII, III-V and II-VI Compounds"*, HgTe: Lattice Parameters 1, (2010)

[12] P. Capper, *"Properties of Narrow Gap Cadmium-Based Compounds"*, Page 400, (1994)

[13] Hamamatsu, *"Characteristics and use of infrared detectors"*, < https://www.hamamatsu.com/resources/pdf/ssd/infrared_techinfo_e.pdf>

[14] D. L. Smith et al., *"Proposal for strained type II superlattice infrared detectors"*, Journal of applied Physics 62, 2545, (1987)

[15] G. J. Brown, *"Type-II InAs/GaInSb Superlattices for infrared Detection: An Overview"*, Proc. of SPIE Vol. 5783, (2005)

[16] A. Rogalski et al., *"InAs/GaInSb superlattices as a promising material system for third generation infrared detectors"*, Infrared Physics & Technology 48, 39–52, (2006)

[17] G. J. Brown et al., *"Recent Advances in InAs/GaSb Superlattices for Very Long Wavelength Infrared Detection"*, Proceedings of SPIE Vol. 4999, (2003)

[18] . H. Campbell et al., *"Farinfrared Photoresponsence of the InAs/GaInSb Superlattice"*, Applied Physics Letters 59, 846, (1991)

[19] Y.Wei et al., *"Adavanced InAs/GaSb Superlattice Photovoltaic Detectors for Very Long Wavelength Infrared Applications"*, Applied Physics Letters 80, 3262 (2002)

[20] J. Nguyen et al.," *Low dark current long-wave infrared InAs/GaSb superlattice detectors"*, Applied Physics Letters 97, 051108 (2010)

[21] E. R. Youngdale et al., *"Auger Lifetime Enhancement in InAs/$Ga_{1-x}In_xSb$ Superlattices"*, Applied Physics Letters 64, 3160 (1994)

[22] C. H. Grein et al., *"Reply to "Comment on 'Temperature limits on infrared detectivities of InAs/InxGa1−xSb superlattices and bulk Hg1−xCdxTe'" [J. Appl. Phys. 74, 4774 (1993)]"*, Journal of Applied Physics 77, 4156 (1995)

[23] C. H. Grein et al., *"Long Wavelength InAs/GaInSb Infrared Detectors: Optimisation of Carrier Lifetimes"*, Journal of Applied Physics 78, 7143 (1995)

[24] Optical Society of America, *"Handbook of Optics, Volume 1: Fundamentals, Techniques, and Design. Second Edition"*, 16.8 (1994)

[25] I. Vurgaftman et al., *"Analysis and performance of type-II superlattice infrared detectors"*, Optical Engineering 50(6), 061007 (2011).

[26] S. Bandara *"Doping dependence of minority carrier lifetime in long-wave Sb-based type II superlattice infrared detector materials"*, Optical Engineering 50(6), 061015 (2011)

[27] G. Belenky et al. *"Effects of carrier concentration and phonon energy on carrier lifetime in type-2 SLS and properties of InAs1-XSbX alloys"*, Proc. SPIE 8012, 80120W, (2011)

[28] D. Donetsky et al., *"Carrier lifetime measurements in short-period InAs/GaSb strained-layer superlattice structures"*, Applied Physics Letters 95, 212104 (2009)

[29] G. C. Osbourn, *"InAsSb strained layer superlattices for long wavelength detector applications"*, Journal of Vacuum Science & Technology B 2, 176 (1984)

[30] S.P. Svenssona et al., *"Growth of type II strained layer superlattice, bulk InAs and GaSb materials for minority lifetime characterization"*, Journal of Crystal Growth Volume 334, Issue 1, 1, Pages 103–107, (2011)

[31] E. H. Steenbergen et al., *"Significantly improved minority carrier lifetime observed in a long- wavelength infrared III-V type-II superlattice comprised of InAs/InAsSb"*,Applied Physics Letters 99, 251110 (2011)

[32] D. Lackner, et al., *"Strain balanced InAs/InAsSb superlattice structures with optical emission to 10μm"*, Applied Physics Letters 95, 081906 (2009)

[33] O. O. Cellek et al., *"InAs/InAsSb Type-II Superlattice: A Promising Material for Mid- Wavelength and Long-Wavelength Infrared Applications"*, Proc. of SPIE Vol. 8353, 83533F , (2012)

[34] E. H. Steenbergen et al., *"Structural and optical characterization of type-II InAs/InAs1−xSbx superlattices grown by metalorganic chemical vapor deposition"*, Applied Physics Letters 99, 071111 (2011)

[35] D. E. Eastman et al., *"Relation of Schotttky Barriers to Empty Surface States on III-V Semiconductors"*, physical review letters 34, 26 (1975)

[36] P. J. P. Tang et al., *"Photo and electro-luminescence studies of uncooled Arsenic rich In(As.Sb) strained layer superlattice light emitting diodes for the 4-12μm band"*, Proc. of SPIE Vol 2397 / 389-298 (1995)

[37] M. Mizuta et al., *"Direct Evidence for the DX Center Being a Subsitutional Donor in AlGaAs Alloy System"*, Japanese Journal of Applied Physics 24, 2 (1985)

[38] InAs – Indium Arsenide, Accessed Jan 2013,
< http://www.ioffe.ru/SVA/NSM/Semicond/InAs>

[39] InSb – Indium Antimonide, Accessed Jan 2013,
< http://www.ioffe.ru/SVA/NSM/Semicond/InSb>

[40] C. G. Van de Walle, *"Band line-ups and deformation potentials in model solid theory"*, Physical Review B 39, 3, (1989)

[41] S. R. Kurtz et al., *"Photoluminescence and the band structure of InAsSb strainedlayer superlattices"*, Appl. Phys. Lett. 53, 216 (1988)

[42] Nextnano Semiconductor Software Solutions, Accessed March 2013, http://www.nextnano.de

[43] A. L. Edwards et al., *"Effect of Pressure on the Absorption Edges of Some III—V; II—VI, and I—VII Compounds", Physical Review 122, 4 (1961)*

[44] P. E. Vann Camp et al., *"Pressure dependence of the electronic properties of cubic III-V In compounds"*, Physical Review B 41, 3 (1990)

[45] P. Y. Yu, M. Cardona, *"Fundamentals of semiconductors"*, (1996)

[46] R. J. Warburton et al., *"The pressure dependence of the effective mass in a GaAs/AlGaAs heterojunction"*, Semiconductor science and Technology 7, (1992)

[47] M. Eremets, *"High Pressure Experimental Methods"*, Oxford University Press (1996)

[48] Originlab Bigaussian Fitting, Accessed Jan 2013,
< http://www.originlab.com/www/helponline/origin/en/UserGuide >

[49] T. Schuler-Sandy et al., *"Gallium Free Type II InAs/InAs$_{1-x}$Sb$_x$ Superlattice Photodetectors"*, Applied Physics Letters 101, 071111 (2012)

[50] P. G. Eliseev et al., *""Blue" temperature-induced shift and band-tail emission in InGaN-based light sources"*, Applied Physics Letters 71, 569 (1997)

[51] Leah Bergman et al., *"Photoluminescence and recombination mechanisms in GaN/Al0.2Ga0.8N superlattice"*, Applied Physics Letters 76, 1969 (2000)

[52] C. H. Chen et al., *"Mechanism of photoluminescence in GaN/Al0.2Ga0.8N superlattices"*, Applied Physics Letters 79, 3806 (2001)

[53] E. K. Plyer, *"Infrared Spectra of Methanol, Ethanil and n-Propanol"*, Journal of Research of the International Bureau of Standards 48, 4 (1952)

[54] J. Osugi et al., *"The Optical Studies of Pressure Effects 1. The measurement of O-H Stretching Vibration Band of Ethanol"*, The Review of Physical Chemistry of Japan 35, 1 (1965)

[55] A. Anderson, et al., *"Infrared Spectra of Liquid and Crystalline Ethanol at High Pressures"*, Spectroscopy Letters: An International Journal for Rapid Communication, 31:2, 369-378 (1998)

[56] H. M. Cheong et al., *"Pressure dependence of band offsets in InAs/Ga$_{1-x}$In$_x$Sb superlattices,* Physical Review B 55, 7 (1997)

Chapter 6 - Conclusions and Further Work

6.1 Thesis Review and Conclusions

The central aim of this thesis was to spectroscopically characterise semiconductor nanomaterials for use in the mid-IR wavelength region. This characterisation was primary achieved using a combination of simulation via the Nextnano software package and through detailed fitting of the experimental data. The primary method of obtaining experimental data in this thesis was through the use of photoluminescence performed using different variations of temperature, power and pressure. These techniques have been used to successfully characterise a temperature dependent blue shift in InAsSb quantum dots and identify the physics behind the shift. They have also provided the first experimental evidence for a predicted defect level above the conduction band edge in an InAs/InAsSb superlattice structure.

In the first chapter a review of why mid-IR devices are important and a selection of the applications to which they can be applied. More specific information is then given on the development and benefits of quantum dots, as well as benefits type II superlattice structures could bring to photo-detector applications.

In the second chapter the fundamental physics which is built upon is subsequent chapters is outlined. This ranges from the change in density of states of a system restricted in its dimensionality, to the theory behind z-analysis that is used to identify the dominant recombination process in all of the samples studied during this work. The most used technique in this work, the physics behind photoluminescence is provided in detail.

The third chapter focuses on the experimental apparatus and configurations used to perform the experiments in this work. Working in the mid-IR wavelength region requires careful attention to the optical properties of the apparatus being selected for work. An example of this is glass optics being replaced with calcium fluoride, this is a requirement of mid-IR work due to the poor transmission spectrum of glass in the region. All of the apparatus used during this work is examined and where available the transmission spectrum of the material is presented. The relevant atmospheric absorption features are also presented for

the region in which this work takes place. The result of this is that no anomalous features of the apparatus being used have interfered with the data presented in this work.

The fourth chapter focuses on mid-IR quantum dots. It begins with a review of how strain is the underlying factor behind most dot morphology, and dot morphology in turn is the dominant factor in emission wavelength along with alloy composition. InAs quantum dots are simulated to correspond to the experimentally measured peak energy. From these simulations it is found that a single group of quantum dots and their excited states cannot account for the two oscillator peak required to achieve a high R^2 value to the experimental data. Instead a bimodal dots are required, something that would have been overlooked if not for the characterisation performed in this work. Analysis of the power dependent PL for these dots also shows a dominant radiative recombination process at high and low temperatures. This implies that if manufactured into devices these dots would have a high efficiency value.

The work in chapter four continues to examine InAsSb quantum dots. The inclusion of antimony into the dot alloy is designed to extend the emission wavelength further into the mid-IR when compared with the previous InAs dots studied. However, due to the larger lattice mis-match the dot width is reduced also reduces the emission wavelength. As a result the InAsSb dots are found to have a similar emission wavelength to the previous InAs dots. As the antimony fraction in InAsSb quantum dots can never accurately be known, only the antimonidation time, simulations were performed to gain an estimate for both the dot width and antimony content. Based on the increased lattice mis-match the InAsSb dots were calculated to be ~13% smaller than the pure InAs dots. To simulate the same emission wavelength as was measured during experiment this required an antimony fraction of 10%. The dot samples were split into two groups once measured, one had an observed temperature dependent blue shift and was fitted using one oscillator to obtain a high R^2 value. The other red shifted with temperature and required a two oscillator fit. Using the simulations this two oscillator fit was found to be the result of bimodal dots, this bimodal dot theory

also explained the temperature dependent blue shift through a change in dominance of the oscillators. Power dependent measurements confirmed this change in dominance as the dots moved from radiative to defect dominated recombination. This also indicated that one group of dots contained no antimony as its dominant recombination process was radiative as seen in the InAs dots. The antimony containing dots were dominated by defect related recombination which is explained trough defects being introduced because of the larger lattice mismatch.

The fifth chapter involved experimentally confirming the existence of a defect level positioned above the conduction band edge in an InAs/InAsSb superlattice. The justification on why new superlattice photo-detectors would provide an advantage over the existing MCT detectors is presented. The dominance of dark currents caused by SRH recombination in the bandgap region is presented for gallium containing superlattices, something that InAs/InAsSb would not be affected by if the defect level is above the conduction band edge. A sapphire ball cell is used to create the high pressures required, these high pressures move the conduction band up in energy until primary energy transition begins to over lap with the defect state. At this point a decline in the measure signal intensity should be observed as carriers recombine via the defect state. This decline in measured intensity was observed at ~19.4kbar. To confirm that this change was caused by a defect level, power dependent PL measurements were performed at high and low pressure. At low pressure the dominant recombination method was found to be radiative, and at high pressure defect related. This gives the first experimental evidence for this defect state being found above the conduction band edge.

6.2 Further Work

The InAs quantum dots were found to have a strongly radiative recombination process rather then the defect related process found in the InAsSb dots. As a result of this it would be interesting to process the wafer into simple P-I-N diodes and characterise the sample electrically. This would allow for a

comparison between spectroscopic characterisation of a wafer sample and electrical characterisation of a device. This would then result in evidence of if a well performing wafer would result in a similarly well performing device.

The InAs/InAsSb superlattice also has interesting further work that could be performed:

(1) The methanol/ethanol pressure medium of the sapphire ball used to maintain hydrostatic pressure cell could be replaced with argon. While this introduces complexity to loading the sapphire ball cell with samples, the problem of alcohol absorption in the 2.8 - 3.6μm region would be overcome allowing additional experiments to be performed.

(2) Additional power dependent measurements at pressures between 0kbar and 17.89kbar could be taken if there were no alcohol absorption features. While currently the position of the defect state is known, its width is not. By observing the point at which the sample migrates from a radiative only recombination process to a combination of radiative and defects would allow this width to be quantified.

(3) The experiments performed in this work could be repeated using other samples shown in chapter 5 table 2 available from the growers in ASU. These additional samples have longer emission wavelengths, meaning that they should interact with the defect state at lower pressures. This would provide confirmation of the results presented in this work. This further work would also have the possibility of differentiating between an InAs and InSb defect state, by experimenting on different InAsSb alloy compositions. If the InAs defect state is being studied then the position would be independent of the antimony content of the sample.

(4) The work on this sample could be repeated at a higher temperature, one that is not in the 'S' temperature dependent region. This would then show if the

increase in intensity with pressure is the result of carriers being liberated from the localised states with pressure.

Appendices

Appendix A: InAs Quantum Dot Structure

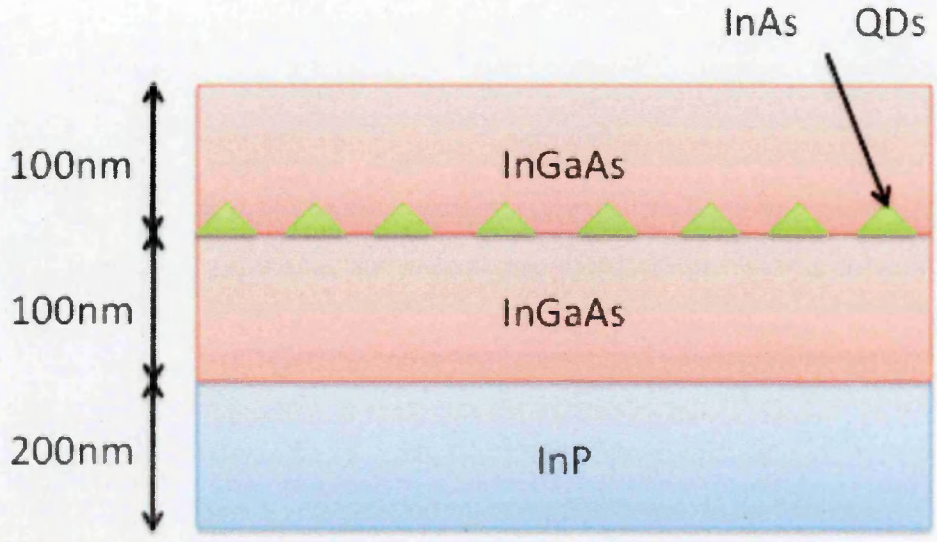

Appendix B: InAs Quantum Dot Wavefunctions

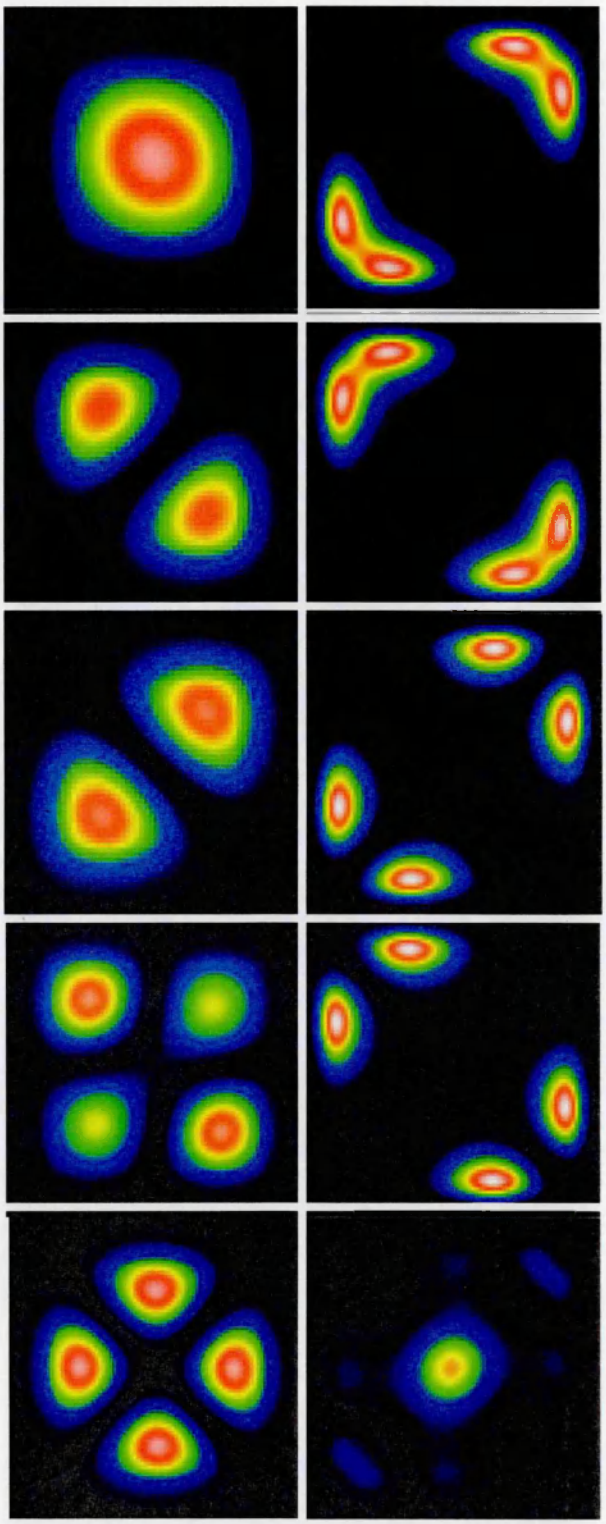

The first five calculated InAs wavefunctions shown from top to bottom. The x and y axis are in plane, while the growth direction z is out of the page. Conduction band functions are shown on the left, HH on the right.

Appendix C: InAsSb Quantum Dot Structure

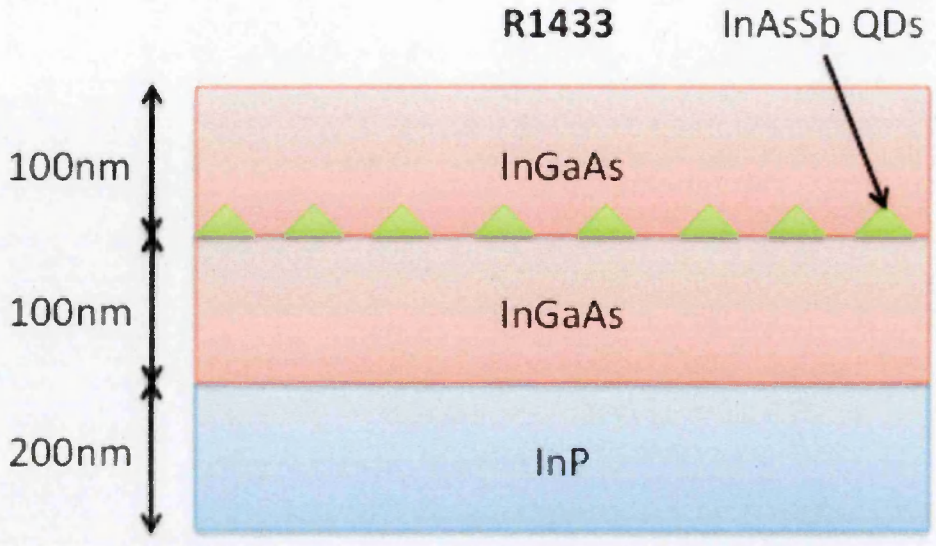

Appendix D: InAsSb Quantum Dot Wavefunctions

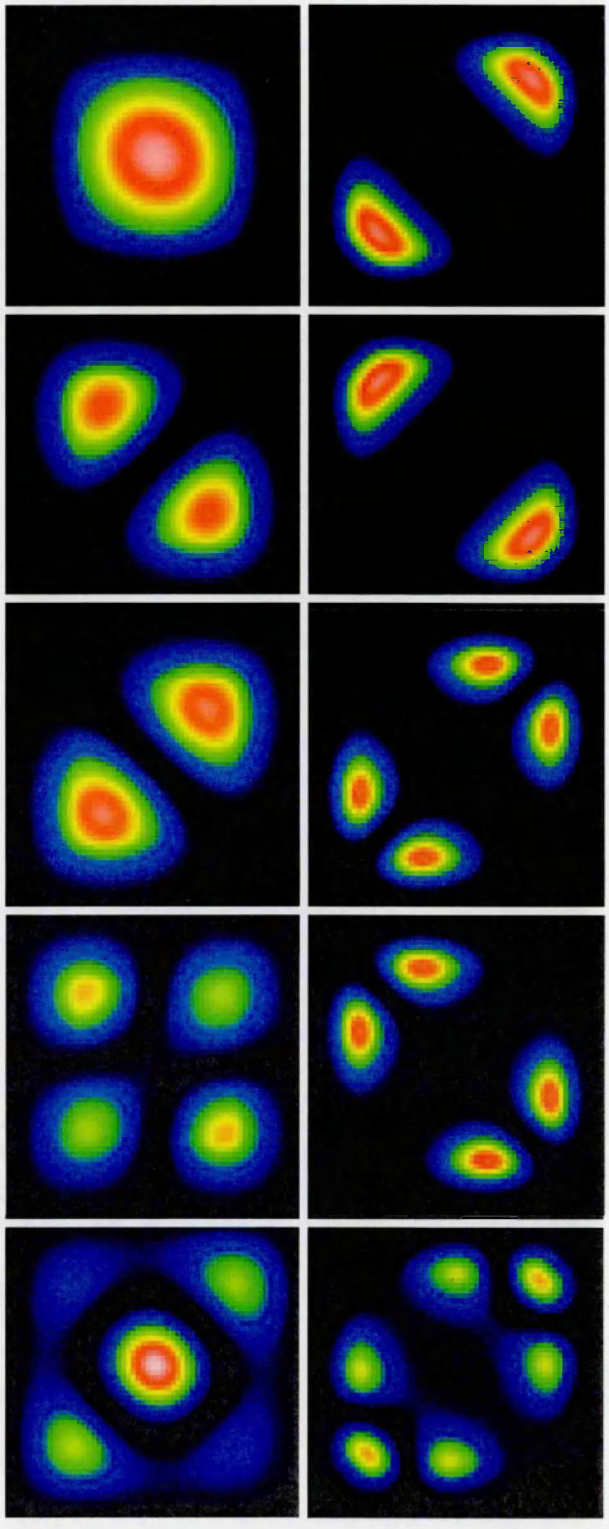

The first five calculated InAsSb wavefunctions shown from top to bottom. The x and y axis are in plane, while the growth direction z is out of the page. Conduction band functions are shown on the left, HH on the right.

Appendix E: Nextnano

The Nextnano software package has been used throughout this work to simulate different nano scale structures. This appendix will cover the basic process and equations used by the software to create these simulations. Further reading can be found at the Nextnano website [1].

The material parameters are taken from an existing database, most of the values are taken from I. Vurgaftan et al.'s paper [2]. The software uses the input file specified by the user to interpolate the values of any ternary alloys e.g. InAsSb. A grid, the dimensions of which the user specifies, is then populated with these materials.

At this point a strain minimisation calculation occurs. When materials of two different lattice constants are joined an elastic strain is created between them. This strain is known to change the conduction band and valence band edges, as well as the **K•p** Hamiltonian of Schrödinger's equation. The strain tensor equation used by Nextnano is given by [3]:

$$\epsilon_{ij} = \frac{1}{2}(\tilde{u}_{ji} + \tilde{u}_{ij})$$

Where ϵ_{ij} is the strain where i and j = 1, 2, 3... and $\tilde{u}_{ji}$ is a vector describing the displacement due to lattice deformation. Following this the electrostatics within the simulated material are solved by the use of the Poisson equation [4]:

$$\nabla \cdot [\varepsilon_0 \varepsilon_r(x) \nabla \phi(x)] = -\rho(x)$$

Where ε_0 is the vacuum permittivity, ε_r is the material dielectric constant at position x, $\phi$is the electrostatic potential at position x, and ρ is the charge density distribution at position x.

The final step is to solve the 8 x 8 **K•p** Schrödinger equation [3] to gain values for the wave functions and corresponding Eigen states.

References:

[1] Nextnano website, Accessed 2013, <http://www.nextnano.de/nextnano3/>

[2] I. Vurgaftman et al., *"Band parameters for III–V compound semiconductors and their alloys"*, Journal of Applied Physics 89, 11, (2001)

[3] S. Birner, Selected Topics of Semiconductor Physics and Technology (G. Abstreiter, M.-C. Amann, M. Stutzmann, and P. Vogl, eds.), Vol. 135,
Verein zur Förderung des Walter Schottky Instituts der Technischen Universität München e.V., München, 239 pp. (2011)

[4] T. Zibold, Selected Topics of Semiconductor Physics and Technology (G. Abstreiter, M.-C. Amann, M. Stutzmann, and P. Vogl, eds.), Vol. 87
Verein zur Förderung des Walter Schottky Instituts der Technischen Universität München e.V., München (2007)